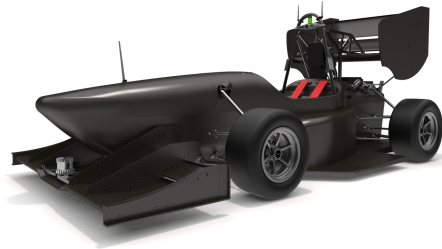




**TÉCNICO**  
LISBOA



## **Traction control of a Formula Student prototype**

**André Filipe Alves Grancho Barroso**

Thesis to obtain the Master of Science Degree in

### **Mechanical Engineering**

Supervisors: Prof. Alexandra Bento Moutinho  
Prof. José Raul Carreira Azinheira

#### **Examination Committee**

Chairperson: Prof. Carlos Baptista Carneira  
Supervisor: Prof. Alexandra Bento Moutinho  
Member of the Committee: Prof. Miguel Afonso Dias de Ayala Botto

**September 2021**



## Acknowledgments

A sincere thank you is due to my family, my rock, without whom this achievement would be meaningless. To my parents, for the unconditional love and for granting me the opportunity to pursue my passions, thank you. To my brother Henrique, for the journey we have shared together, and the one we will go through, thank you. To my dear friends Marta, Rodrigo, Mariana and Sofia, thank you for being yourselves.

A word of appreciation goes out to my Formula Student teammates - including alumni and more recent team members -, particularly Migdon, Rodrigo, Gonçalo and Stefan, with whom I built an incredible race car, making great friendships along the way.

Finally, I would like to thank professor Miguel Ayala Botto and my supervisors, professors Alexandra Moutinho and José Azinheira, for the invaluable guidance and help, particularly during a year of remote work. Additionally, I would like to thank the help given by Alexandre Athayde and Solange Santos, from a technical but also motivational point of view.





## Resumo

O controlo do escorregamento dos pneus é essencial em protótipos de competição automóvel, tal como num veículo Formula Student. Possuindo uma elevada relação potência-peso, estando sujeito a acelerações longitudinais e laterais consideráveis, e tendo relativamente curtas dimensões entre eixos e de largura de vias, um protótipo de Formula Student sofre transferências de massa dinâmicas significativas. Com um motor elétrico por cada cubo de roda, o futuro protótipo da FST Lisboa - que terá configurações autónoma e pilotada - apresenta uma oportunidade para controlar diretamente o estado dos quatro pneus e melhorar o desempenho dinâmico do veículo.

Um sistema de controlo de tração deve tolerar não linearidades e ser robusto a mudanças ou incertezas paramétricas de forma a melhorar o desempenho dinâmico do veículo. Para cumprir esses requisitos propõe-se uma arquitetura de controlo em cascata, baseada em controlo proporcional e na dinâmica de pneus, capaz de satisfazer simultaneamente requisitos de desempenho em termos longitudinais (acelerar e desacelerar) e laterais (em curva). Uma componente de realimentação é utilizada para seguir referências de velocidade longitudinal, enquanto que uma componente antecipativa melhora o desempenho em curva, seguindo referências de razão de guinada. Ambas as componentes melhoram a capacidade do veículo de acelerar, desacelerar e guinar, evitando a tendência natural de perder a tração em pneus com menor carga vertical devido a transferências de massa. Um módulo de distribuição de potência corrige os comandos de binário dos motores, de modo a cumprir os limites de potência elétrica em aceleração e desaceleração.

Sugere-se uma heurística para sintonizar os parâmetros resultantes dos controladores de tração. Posteriormente, a sensibilidade dos controladores a variações e incertezas paramétricas é estudada, avaliando a sua robustez. Finalmente, os controladores de tração são validados em pistas genéricas, com um grau de complexidade superior às usadas para sintonizar os controladores.

**Palavras-chave:** Formula Student, controlo de tração, dinâmica de veículo, controlo em cascata



## Abstract

Controlling tire slip is crucial for race cars performance, such as Formula Student prototypes. The high power-to-weight ratio, longitudinal and lateral accelerations, coupled with relatively short wheelbase and track width, results in significant dynamic mass transfers. With four independent wheel-hub electric motors, the future prototype from FST Lisboa - with both driverless and person-driven configurations - provides an opportunity to directly control the state of the four tires and improve dynamic performance.

A traction control system must handle nonlinearities and be robust to parametric changes or uncertainties to improve dynamic vehicle behaviour. To fulfil these requirements, a cascade control architecture based on proportional control and tire dynamics is proposed, being able to simultaneously fulfil longitudinal (accelerating and decelerating) and lateral (turning) dynamics requirements. A feedback component is employed to track the longitudinal speed and fulfil tire and electric motor constraints, while a feedforward term is used to track the yaw rate and achieve torque vectoring in turns. Both components improve the vehicle ability to accelerate, decelerate and turn, mitigating the natural tendency to break traction in vertically unloaded tires due to mass transfers. A power distribution module corrects the individual torque commands to enforce electrical power limits in acceleration and deceleration.

A heuristic method is suggested to tune the traction control parameters. The sensitivity of the resulting traction controllers is studied for varying traction conditions and vehicle parameters, assessing the proposed solution's robustness. Finally, the traction controllers are validated on generic race tracks, with a higher degree of complexity from the benchmarks used for tuning.

**Keywords:** Formula Student, traction control, vehicle dynamics, cascade control



# Contents

- Acknowledgments . . . . . iii
- Resumo . . . . . v
- Abstract . . . . . vii
- List of tables . . . . . xi
- List of figures . . . . . xiii
- Nomenclature . . . . . xv
- Glossary . . . . . xix
  
- 1 Introduction . . . . . 1**
- 1.1 Motivation . . . . . 1
- 1.2 Traction control systems . . . . . 2
- 1.3 Objectives . . . . . 4
- 1.4 Thesis outline . . . . . 5
  
- 2 Vehicle modelling . . . . . 6**
- 2.1 Realistic vehicle model . . . . . 6
  - 2.1.1 Kinematics and dynamics . . . . . 8
  - 2.1.2 Tire modelling . . . . . 9
    - Magic Formula for pure slip conditions . . . . . 11
    - Magic Formula for combined slip conditions . . . . . 14
  - 2.1.3 Powertrain modelling . . . . . 15
  - 2.1.4 Steering modelling . . . . . 17
- 2.2 Simplified vehicle models . . . . . 19
  - 2.2.1 Bicycle model . . . . . 19
  - 2.2.2 Unicycle model . . . . . 22
  - 2.2.3 Model used for control design . . . . . 23
  - 2.2.4 Dynamic mass transfers . . . . . 25
  
- 3 Traction control of a Formula Student prototype . . . . . 28**
- 3.1 Autonomous driving simulator overview . . . . . 28
- 3.2 Simplified vehicle model implementation . . . . . 29
  - 3.2.1 Longitudinal controller . . . . . 30

3.2.2	Lateral controller . . . . .	30
3.3	Realistic vehicle model implementation . . . . .	31
3.3.1	Longitudinal controller . . . . .	32
3.3.2	Lateral controller . . . . .	33
3.3.3	Power distribution . . . . .	34
<b>4</b>	<b>Controllers tuning and validation</b>	<b>37</b>
4.1	Formula Student Driverless regulations . . . . .	37
4.2	Longitudinal performance . . . . .	39
4.3	Lateral performance . . . . .	41
4.4	Combined performance . . . . .	43
4.5	Simulation specifics . . . . .	44
<b>5</b>	<b>Results and discussion</b>	<b>46</b>
5.1	Solution without traction control . . . . .	46
5.1.1	Longitudinal dynamics . . . . .	46
5.1.2	Lateral dynamics . . . . .	49
5.2	Longitudinal performance . . . . .	51
5.3	Lateral performance . . . . .	59
5.4	Combined performance . . . . .	64
<b>6</b>	<b>Conclusions</b>	<b>72</b>
6.1	Achievements . . . . .	72
6.2	Future work . . . . .	73
	<b>Bibliography</b>	<b>74</b>

# List of tables

2.1	Boundaries of the parameters used in the tire model. . . . .	11
2.2	Magic formula coefficients for pure-slip tire curves. . . . .	13
2.3	Electric motor characterisation from a mechanical standpoint. . . . .	16
2.4	Motor efficiency for the range of speeds and torques. . . . .	17
2.5	List of lever arms for $M_z$ computation for tire $i$ . . . . .	19
4.1	Performance requirements for $u_{ref} = 10$ m/s. . . . .	39
4.2	Performance requirements for $r_{ref} = 1$ rad/s. . . . .	42
4.3	Stand still initial conditions in the simulation environment. . . . .	45
4.4	Constants and coefficients that model the FST 10d. . . . .	45
5.1	$T_{r_{max}}$ sweep for an Acceleration event. . . . .	53
5.2	$T_{f_{max}}$ sweep for an Acceleration event. . . . .	54
5.3	$T_{f_{min}}$ and $T_{r_{min}}$ sweep for an Acceleration event. . . . .	55
5.4	$\mu$ sensitivity for an Acceleration event. . . . .	57
5.5	$m$ sensitivity for an Acceleration event. . . . .	58
5.6	$R$ sensitivity for an Acceleration event. . . . .	58
5.7	$K_r$ sweep. . . . .	60
5.8	$\mu$ sensitivity for a chicane. . . . .	63
5.9	Parameters considered for trajectory generation. . . . .	64
5.10	$\mu$ sensitivity for the FSG race track. . . . .	65
5.11	$\mu$ sensitivity for the FSI race track. . . . .	65





# List of figures

1.1	FST 08e team in the Formula Student Italy competition (2018).	2
2.1	Schematic of the realistic vehicle model.	7
2.2	Schematic of a tire and generated forces/moment.	10
2.3	Typical pure slip curves for the Magic Formula tire model.	12
2.4	Tire curve produced by the Magic Formula, with the respective curve parameters.	13
2.5	Longitudinal and lateral force surfaces as function of tire slip ratio and angle.	15
2.6	Example of a measured G-G diagram of a Formula Student prototype.	15
2.7	Torque and power curves of the electric motor.	16
2.8	Ackermann steering geometry.	18
2.9	Free-body diagram for planar motion.	20
2.10	Schematic of the bicycle model.	21
2.11	Schematic and free-body diagram of the unicycle model.	22
2.12	Longitudinal weight transfer in acceleration.	25
2.13	Lateral weight transfer in a right-hand turn.	26
2.14	Weight transfer due to aerodynamic forces.	27
3.1	Diagram of the autonomous driving simulator for FST Lisboa.	29
3.2	Block diagram of the simplified traction control scheme.	29
3.3	Controller implemented for the longitudinal subsystem.	30
3.4	Controller implemented for the lateral subsystem.	31
3.5	Block diagram of the full complexity traction control scheme.	32
3.6	Block diagram of the longitudinal controller.	33
3.7	Block diagram of the lateral controller.	34
4.1	Layout of the Acceleration event.	38
4.2	Layout of the Skid Pad event.	38
4.3	Layout of the Trackdrive event.	38
4.4	Types of cones used to define the race tracks.	39
4.5	Longitudinal speed reference for the Acceleration event.	40
4.6	Yaw rate reference for a chicane.	42
4.7	Race tracks used for simulation.	43

5.1	Results for the Acceleration event, without traction control. . . . .	48
5.2	Results for the chicane, without traction control. . . . .	50
5.3	Results for a step in longitudinal speed. . . . .	52
5.4	Results for the Acceleration event, with traction control. . . . .	56
5.5	Yaw rate response for a step input and resulting vehicle path. . . . .	60
5.6	Yaw rate response for a chicane and resulting vehicle path. . . . .	61
5.7	Results for the chicane, with lateral control. . . . .	62
5.8	Results associated to the poor traction trajectory for the FSG race track. . . . .	68
5.9	Results associated to the excellent traction trajectory for the FSG race track. . . . .	69
5.10	Results associated to the poor traction trajectory for the FSI race track. . . . .	70
5.11	Results associated to the excellent traction trajectory for the FSI race track. . . . .	71

# Nomenclature

## Greek symbols

$\alpha$	Tire side slip angle.
$\beta$	Vehicle side slip angle.
$\Delta$	Linear suspension deformation; variation.
$\delta$	Steering wheel angle.
$\eta$	Efficiency.
$\gamma$	Tire camber angle.
$\kappa$	Tire slip ratio.
$\lambda$	Eigenvalue.
$\mu$	Tire-road friction coefficient.
$\Omega$	Angular CG velocity.
$\omega$	Wheel angular speed.
$\Phi$	Euler angles.
$\rho$	Air density; normalised combined slip magnitude.

## Roman symbols

$(\vec{x}, \vec{y}, \vec{z})$	Reference frame versors.
$A$	State matrix; projected area.
$B$	Input matrix.
$C$	Output matrix; coefficient.
$c$	Damping coefficient.
$D$	Direct transmission matrix.
$e$	Error.

$F$	Force.
$F_x$	Longitudinal tire force.
$F_y$	Lateral tire force.
$F_z$	Vertical tire force.
$g$	Acceleration of gravity.
$GR$	Drivetrain gear ratio.
$I$	Electrical current.
$J$	Inertia tensor; wheel rotational inertia.
$J_P$	Performance index.
$K$	Proportional gain.
$k$	Elastic constant.
$L$	Distance.
$M$	Moment.
$m$	Vehicle mass.
$M_z$	Self-aligning tire moment.
$MR$	Motion ratio.
$N$	Angular speed.
$P$	CG position; power.
$R$	Tire radius.
$r$	Yaw rate.
$SR$	Steering ratio.
$T$	Torque.
$t$	Time constant; time.
$TF$	Torque fraction.
$u$	Longitudinal speed; input vector.
$V$	Linear CG velocity; voltage.
$v$	Lateral speed.
$W$	Weight.

$w$  Vertical speed.  
 $x$  State vector.  
 $y$  Output vector.

### **Subscripts**

$0$  Initial.  
 $\kappa$  Relative to the tire slip ratio.  
 $a$  Acceleration; aerodynamic.  
 $acc$  Acceleration.  
 $B$  Moving/body reference frame.  
 $cmd$  Command.  
*critical* Critical value in terms of stability.  
 $D$  Drag.  
 $dec$  Deceleration.  
*diff* Difference or asymmetry.  
*eff* Effective.  
 $f$  Front; final.  
 $G$  Fixed/ground reference frame.  
 $h$  Height.  
 $i$  Wheel/suspension quarter index.  
 $L$  Lift.  
*lap* Relative to a single lap.  
*lim* Limit.  
 $m$  Motor.  
*max* Maximum.  
*mean* Mean value.  
*min* Minimum.  
*nom* Nominal.  
 $PT$  Powertrain.

*r* Rear; rotation; relative to the yaw rate.  
*ref* Reference.  
*run* Relative to a single run.  
*STA* Steering actuation.  
*sus* Suspension.  
*t* Width; translation.  
*TV* Torque vectoring.  
*u* Relative to the longitudinal speed.  
*w* Wheel.

### **Superscripts**

<sup>-1</sup> Inverse.  
<sup>·</sup> Derivative with respect to time.  
*dyn* Dynamic.  
*st* Static.  
*T* Transpose.

# Glossary

<b>4WD</b>	Four-wheel driven.
<b>ABS</b>	Anti-lock braking system.
<b>CG</b>	Centre of gravity.
<b>CP</b>	Centre of pressure.
<b>DNF</b>	Did not finish.
<b>DOF</b>	Degree of freedom.
<b>DV</b>	Driverless vehicle.
<b>EV</b>	Electric vehicle.
<b>FSD</b>	Formula Student Driverless.
<b>FSG</b>	Formula Student Germany.
<b>FSI</b>	Formula Student Italy.
<b>FST Lisboa</b>	Formula Student team from Instituto Superior Técnico.
<b>FWD</b>	Front-wheel driven.
<b>GPS</b>	Global Positioning System.
<b>ICEV</b>	Internal combustion engine vehicle.
<b>LIDAR</b>	Laser imaging, detection and ranging.
<b>PMSM</b>	Permanent magnet synchronous motor.
<b>RMS</b>	Root-mean-square.
<b>RWD</b>	Rear-wheel driven.
<b>TCS</b>	Traction control system.
<b>TC</b>	Traction control.





# Chapter 1

## Introduction

### 1.1 Motivation

The term "traction" is often used to describe how well a ground vehicle interacts with the driving surface. The abundance of driving surfaces (tarmac, concrete, gravel, snow, cobblestones or even a mixture), tire conditions (compound type, wear, pressure and temperature) and environmental conditions (dry, wet, damp or icy) dictate that the concept of traction is a complex one.

From a high-level point of view, traction control systems (TCS) regulate wheel rotation, avoiding extreme situations, such as wheel lock and wheel spin. Wheel lock occurs frequently during hard braking manoeuvres, if the applied braking force exceeds a critical value, stopping the wheel and causing tire skid. Conversely, wheel spin can occur at any point when there is excess driving power or poor traction conditions. Both extreme cases must be avoided since they may create unstable driving situations and decrease the effective driving/braking forces, thus resulting in vehicle performance degradation or even loss of control. Traction control (TC) started with the implementation of the anti-lock braking system (ABS) in aircraft and then in automobiles [1]. Other TC mechanisms include anti-spin control, electronic stability program, electronic differential, active suspension and four-wheel steering [2].

FST Lisboa [3] is a team of students from Instituto Superior Técnico, shown in figure 1.1, who are passionate about motorsports and engineering. The team was created in 2001 and initially designed race cars with internal combustion engines (ICEV). A shift was made to prototypes with electric powertrains (EV) in 2011, when the team introduced the first electric racing prototype made in Portugal. 2021 was the first year when two prototypes were simultaneously developed: a driverless (DV) and a person-driven one. The prototypes are designed, manufactured and then used to race in Formula Student competitions. These are international design events where students build a single-seat, formula-type race car and compete against teams from many countries. The competitions do not simply reward the fastest car, but also consider time and project management, manufacturing processes and the economical aspects of automotive engineering.

Aiming to bridge the industry needs and technical universities, Formula Student Germany [4] (FSG) organized the first driverless competition in 2017 at the Hockenheimring - Formula Student Driverless

(FSD). In this competition, that has since spread to other countries and race tracks, the teams are challenged to build a prototype that can autonomously navigate through tracks whose layout and environment is regulated. The race track limits are defined by plastic cones of several shapes and colours. To push the development of autonomous driving in the Formula Student competitions even further, FSG decided that the teams competing with person-driven prototypes should run half of the dynamic events in a driverless configuration from 2022 on [5]. Given these constraints, FST Lisboa decided to focus all their efforts into designing one prototype for the 2022 season - a hybrid race car in the sense of having person-driven and driverless configurations that can be mounted according to the type of dynamic event the team wishes to participate in.

To extract more dynamic performance from the future hybrid vehicle, this work proposes an approach for TC that can be applied to both vehicle configurations. In the scope of this thesis, the FSD category is considered in greater detail, since it possesses a higher degree of complexity and richness in terms of vehicle control than the person-driven one.



Figure 1.1: FST 08e team in the Formula Student Italy competition (2018).

## 1.2 Traction control systems

A racing driver, or a computer emulating the driver, is able to produce two major sorts of inputs to drive a car: accelerator/brake pedal input and steering wheel input. Following this logic, a TCS encompasses two categories: longitudinal and lateral control. The longitudinal controller monitors tire adhesion to prevent wheel lock and spin, while the lateral one deals with vehicle behaviour in turns, also referred to as the yaw motion [6].

The main function of a TCS is to guarantee adequate driving torques, while providing information about the varying tire-road conditions. To implement traction control, one is typically interested in regulating tire slip, defined by the slip ratio  $\kappa$ . Even though there are several definitions for the slip ratio [7], which will be formally defined in chapter 2, it can be generally thought of as the relative linear speed between the tires and vehicle centre of gravity (CG). If the former is higher, the vehicle should be accelerating, otherwise deceleration occurs. The slip ratio directly affects the effective driving force and

is not easily measured, so it should be estimated online, fusing information from the available sensors. Tire and vehicle dynamics are nonlinear and have time-varying parameters, reasons why TC algorithms must be robust with respect to nonlinearities and parametric uncertainties [2] [8].

TCS are implemented differently according to the types of powertrain. For vehicles with internal combustion powertrains, TC can be achieved by engine control (air and fuel flow regulation, spark-timing shift), brake control (independent brake actuation) or torque transfer (a fraction of the available torque can be transferred to a wheel with better traction via differentials or clutches) [6]. Vehicles with electric powertrains, especially those with independent motors, present a good opportunity for the application of more sophisticated TC algorithms. Comparing with ICEV, EV have a much faster and precise torque response (in the region of hundredths of seconds [6]), the torque is easily measured knowing the motor current, and the possibility of having independent in-wheel motors enables decoupled wheel torque control [9] [10] [11]. For the EV case, since electric machines can also work as generators, acceleration and deceleration can both be performed without an additional braking system, implying that TC can be realised using only software [6], with the added benefit of battery recharge while braking. In both ICEV and EV, traction control also aims to improve energetic efficiency by limiting wheel slip [2] [12].

Driving forces produced by tires in a typical race track surface vary nonlinearly with  $\kappa$ , presenting a strictly ascending part in which they are directly proportional to  $\kappa$ , followed by an inflection point in which the forces reach a maximum -  $\kappa_{critical}$  - and a strictly descending part, in which they are inversely proportional to  $\kappa$ , rendering the traction system unstable for slip ratios higher than the optimal value  $\kappa_{critical}$  [8]. The naïve approach would be to try to realise optimal slip ratio controls according to a tire model such as the Magic Formula [13], however this strategy is not sufficiently sensitive to changing tire-road conditions and results in poor control performance [2]. Commercial TCS are typically designed for the worst-case scenarios that the vehicle might encounter - such as icy road conditions with old tires - which generally results in a suboptimal solution [2] [11] [12], certainly not suitable for a racing application. An approach that incorporates robustness to nonlinearities and parameter variability in its formulation is sliding-mode control, in which the control action may change structure under varying operating conditions, being robust to parameter variations and bounded disturbances [8] [14]. Another approach for TC is an online estimation of the maximum transmissible torque, as demonstrated in [12] and [15]. According to [16], the presence of nonlinearities, parameter variations and state constraints discourages the use of optimal control strategies. The employment of neuro-fuzzy control schemes is also a possibility, as shown in [14], where the unknown nonlinear slip dynamics are approximated by a neural network, robust to modelling inaccuracies; and in [11], where a fuzzy-logic controller is able to compensate for the complex nonlinear tire-road behaviour and adapt to varying road surfaces. Regarding pure longitudinal control, two subcategories in terms of implementation arise: those that require the vehicle/chassis velocity and those that do not. If the vehicle is front (FWD) or rear-wheel driven (RWD), chassis velocity can be estimated using odometry data from the non-driven wheels. For these wheels, tire slip is negligible, only enough to overcome the driving resistances. If, however, the vehicle is four-wheel driven (4WD), more complex algorithms must be employed to estimate it. In any case, due to the practical difficulty in estimating vehicle velocity - even with access to GPS data -, control

schemes that do not require it may be preferable in terms of robustness [12]. Additionally, the integration of chassis acceleration in time, as measured by accelerometers, to obtain the velocity is not a viable option since error is propagated due to the long-term integration, causing drift [10].

TCS for Formula Student prototypes are not implemented as in most commercially available vehicles, since the typical single-wheel/independent modelling does not accurately capture the coupling and interaction between wheels, due to the high accelerations and mass transfers that the Formula Student vehicles experience [17]. Regarding the advancements proposed by former members of FST Lisboa, several vehicle control strategies were explored in the last decade. Lateral control strategies for FSD were studied in [18], which consisted in a decoupled approach between lateral and longitudinal dynamics that did not consider tire slip for the latter. An ABS for a Formula Student prototype used a cascade control architecture with a proportional-integrative-derivative-fuzzy controller for slip ratio on the outer loop and a brake pressure proportional-derivative controller for the inner loop [19]. From a data-driven perspective, a dynamic vehicle model generated using data from physical vehicle testing with a neural network was used as the prediction model for a nonlinear model predictive controller [20]. A torque vectoring control scheme proposed for a rear-wheel driven (RWD) prototype emulates a mechanical differential to improve handling, using optimal control strategies for yaw rate and lateral velocity tracking [21]. Other Formula Student teams have proposed a linear-quadratic-regulator-integrative approach to regulate traction of a 4WD vehicle [17] and a method to control a RWD prototype that includes both open and closed-loop components to control the relative slip between front and rear wheels [22].

This thesis aims to implement a traction control scheme for an electric Formula Student prototype where longitudinal and lateral dynamics are coupled, aiming to improve vehicle performance in the dynamic events of the Formula Student competitions.

### 1.3 Objectives

The traction control system, also termed a low-level controller, will work downstream from a high-level controller (if the vehicle is in driverless mode) or a driver (if the vehicle is piloted), which effectively navigate the vehicle on the race track. The low-level controller must regulate the actuation effort in order to ensure vehicle stability and avoid wheel lock and spin. To design and implement the traction control system, the following logic steps and intermediate objectives are defined:

- Research about traction control strategies and understand the mechanisms that govern tire-road interaction;
- Implement a realistic vehicle model that simulates the behaviour of a Formula Student vehicle, including a sufficiently complex tire model, that adequately captures the nonlinear tire behaviour;
- Design traction controllers based on simplified vehicle models and test their validity against the realistic vehicle model;
- Develop a control architecture capable of influencing both longitudinal and lateral vehicle dynamics, while fulfilling tire and powertrain constraints;

- Tune the proposed traction controllers for simple driving benchmarks using a heuristic method;
- Validate the resulting solution for two generic FSD race tracks.

## 1.4 Thesis outline

The thesis is divided into six chapters, whose contents are now briefly described. In the present chapter, the motivation, requirements and constraints for TCS design are introduced, including a literature review which contemplates TC mainly from a commercial vehicle point of view. Vehicle modelling is detailed in chapter 2, containing the basis for the simulator used for validation. Several simplified models are derived to better understand the traction control problem. Chapter 3 is dedicated to introducing the traction controllers, consisting of three modules: longitudinal controller, lateral controller and power distribution. From the three modules result several design parameters which must be tuned. In chapter 4, a heuristic tuning procedure is suggested, using representative instances for longitudinal and lateral dynamics, separately. In chapter 5, the results of the tuning procedure to improve longitudinal and lateral performance from a baseline solution is documented, as well as some preliminary conclusions. Finally, the proposed traction controllers are validated for two generic, complex, FSD race tracks. In chapter 6, the achievements and shortcomings of this work are summarised, including suggestions about future research on this topic.

## Chapter 2

# Vehicle modelling

Several degrees of complexity and detail can be adopted to simulate the dynamic driving behaviour of a vehicle. To achieve an accurate representation of reality, complex and computationally expensive programs are used in motorsports, since on-track testing opportunities are scarce. Formula Student is no exception, since the teams often have a relatively short amount of time before the summer competitions to validate and tune their prototypes. For these reasons, it is important to validate controllers in a simulation environment before proceeding to the physical implementation on the vehicle. In this work, a nonlinear, tridimensional, rigid-body dynamics car model is used as a validation tool. However, the design of controllers for any vehicle module is impractical using such a complex vehicle model. Simpler and often linear models are derived for control design, which provide an intuitive platform to employ linear or nonlinear control techniques.

In this chapter, a description of the vehicle model used for simulation is made - with emphasis on tire and powertrain modelling - as well as simplified models, useful to understand how to approach the traction control problem of a Formula Student prototype.

### 2.1 Realistic vehicle model

The simulator used in this thesis is based on a simulator developed by Prof. José Azinheira, thoroughly documented in [23]. The possibility of having access to the source code and adaptation to the Formula Student environment was the decisive factor to using it instead of a commercially available software.

The simulator models the vehicle as a rigid body with six degrees of freedom (DOF) and a vertical suspension system for each wheel. The car is four-wheel driven by independent electric motors and front-wheel steered. To mathematically describe the vehicle motion, six reference frames of the north-east-down type are used. The fixed/ground reference frame  $(\vec{x}_G, \vec{y}_G, \vec{z}_G)$  allows the description of vehicle positions and the moving/body reference frame  $(\vec{x}_B, \vec{y}_B, \vec{z}_B)$  coincides with the car's CG, aligned forwards/left/down, respectively. Four additional reference frames  $(\vec{x}_i, \vec{y}_i, \vec{z}_i)$ ,  $i = 1, 2, 3, 4$  are attached to the tire contact patches. Subscripts  $i$  represent the different suspension quarters, according to: front-

left ( $i = 1$ ), front-right ( $i = 2$ ), rear-left ( $i = 3$ ) and rear-right ( $i = 4$ ). As a simplification, the tires are considered rigid and the contact patches as points where each tire interacts with the road. Figure 2.1 shows a schematic of the resulting realistic vehicle model, including the reference frames, suspension systems and inputs (in green).

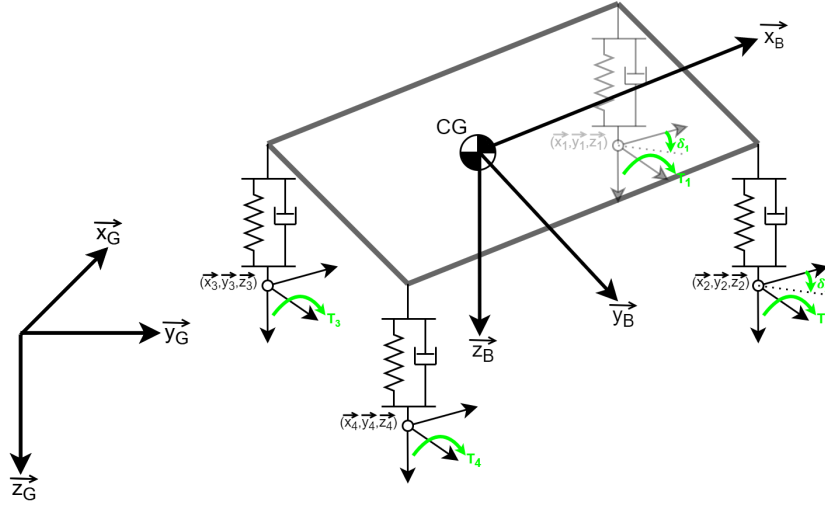


Figure 2.1: Schematic of the realistic vehicle model.

The vehicle model is formulated in a state-space representation [24], expressed by:

$$\dot{x}(t) = f(x(t), u(t)); \quad (2.1)$$

$$y(t) = h(x(t), u(t)); \quad (2.2)$$

in which  $x$  is the state vector,  $u$  the input vector and  $y$  the output vector, as defined in equations (2.3)-(2.5). The system output vector  $y$  includes both the state vector  $x$  and some additional outputs related to the employed tire model that are useful in simulation. The nonlinear vector functions  $f$  and  $h$  describe the system state and output, respectively.

$$x(t) = (V \ \Omega \ P_G \ \Phi \ \omega)^T; \quad (2.3)$$

$$u(t) = (T \ \delta)^T; \quad (2.4)$$

$$y(t) = (V \ \Omega \ P_G \ \Phi \ \omega \ \Delta \ \kappa \ \alpha \ F_x \ F_y \ F_z \ M_z \ T_z)^T. \quad (2.5)$$

The definitions of the states, inputs, outputs and respective units are the following:

- $V = (u \ v \ w)$  [m/s]: linear CG velocity, expressed in the body frame;
- $\Omega = (p \ q \ r)$  [rad/s]: angular CG velocity, expressed in the body frame;
- $P_G = (x_G \ y_G \ z_G)$  [m]: CG position, expressed in the ground frame;
- $\Phi = (\phi \ \theta \ \psi)$  [rad]: Euler angles (rotations from the ground to the body frame);
- $\omega = (\omega_1 \ \omega_2 \ \omega_3 \ \omega_4)$  [rad/s]: angular speeds of wheels 1 to 4;
- $T = (T_1 \ T_2 \ T_3 \ T_4)$  [N.m]: driving or braking torque delivered by tires 1 to 4;

- $\delta$  [rad]: steering wheel angle;
- $\Delta = (\Delta_1 \Delta_2 \Delta_3 \Delta_4)$  [m]: linear suspension deformation of quarters 1 to 4;
- $\kappa = (\kappa_1 \kappa_2 \kappa_3 \kappa_4)$  [-]: slip ratio of tires 1 to 4;
- $\alpha = (\alpha_1 \alpha_2 \alpha_3 \alpha_4)$  [rad]: slip angle of tires 1 to 4;
- $F_x = (F_{x_1} F_{x_2} F_{x_3} F_{x_4})$  [N]: longitudinal force produced by tires 1 to 4;
- $F_y = (F_{y_1} F_{y_2} F_{y_3} F_{y_4})$  [N]: lateral force produced by tires 1 to 4;
- $F_z = (F_{z_1} F_{z_2} F_{z_3} F_{z_4})$  [N]: vertical force produced by tires 1 to 4;
- $M_z = (M_{z_1} M_{z_2} M_{z_3} M_{z_4})$  [N.m]: self-aligning moment produced by tires 1 to 4;
- $T_z$  [N.m]: yawing torque around the  $\vec{z}_B$  axis.

All the states, inputs and outputs are time-variant but the notation  $(t)$  was dropped to simplify the reading.

### 2.1.1 Kinematics and dynamics

From a kinematics perspective, the linear (2.6) and angular (2.7) velocities of the body frame can be expressed in the fixed/ground frame as:

$$\dot{P}_G(t) = S(t)^T V(t) \text{ [m/s];} \quad (2.6)$$

$$\dot{\Phi}(t) = R(t)^{-1} \Omega(t) \text{ [rad/s];} \quad (2.7)$$

where  $S$  (2.8) is the rotation matrix that converts a vector expressed in fixed frame coordinates to one expressed in body frame coordinates and  $R$  (2.9) is a transformation matrix from the Euler angles rate of change to the CG angular velocities:

$$S(t) = \begin{pmatrix} 1 & 0 & 0 \\ 0 & \cos(\phi(t)) & -\sin(\phi(t)) \\ 0 & \sin(\phi(t)) & \cos(\phi(t)) \end{pmatrix} \begin{pmatrix} \cos(\theta(t)) & 0 & \sin(\theta(t)) \\ 0 & 1 & 0 \\ -\sin(\theta(t)) & 0 & \cos(\theta(t)) \end{pmatrix} \begin{pmatrix} \cos(\psi(t)) & -\sin(\psi(t)) & 0 \\ \sin(\psi(t)) & \cos(\psi(t)) & 0 \\ 0 & 0 & 1 \end{pmatrix}; \quad (2.8)$$

$$R(t) = \begin{pmatrix} 1 & 0 & -\sin(\theta(t)) \\ 0 & \cos(\phi(t)) & \cos(\theta(t)) \sin(\phi(t)) \\ 0 & -\sin(\phi(t)) & \cos(\theta(t)) \cos(\phi(t)) \end{pmatrix}. \quad (2.9)$$

The dynamics equations can be derived according to the Newton-Euler formulation, applied on the CG translation (2.10), CG rotation (2.11) and wheels rotation (2.12):

$$m \dot{\vec{V}}(t) = -m (\vec{\omega}(t) \times \vec{V}(t)) + m S(t) \vec{g} + \sum \vec{F}_{CG}(t); \quad (2.10)$$

$$J_{CG} \dot{\vec{\Omega}}(t) = -(\vec{\Omega}(t) \times J_{CG} \vec{\Omega}(t)) + \sum \vec{T}_{CG}(t); \quad (2.11)$$

$$J_w \dot{\omega}(t) = T(t) - F_x(t) R + \sum T_w(t). \quad (2.12)$$



Considering equation (2.10),  $m$  is the vehicle mass,  $\vec{g}$  is the gravity vector and  $\vec{F}_{CG}$  is the vector of resultant forces acting on the CG, which includes tire, dissipation and aerodynamics forces. Both dissipation and aerodynamics forces are proportional to  $\|\vec{v}\|^2$ . Regarding equation (2.11),  $J_{CG}$  is the CG inertia tensor and  $\vec{T}_{CG}$  is the vector of resultant torques acting on the CG, introducing energy dissipation proportional to  $\|\vec{\Omega}\|^2$ . Finally, in equation (2.12),  $J_w$  is the wheel rotational inertia and  $T_w$  is the wheel dissipation torque, proportional to  $\|\omega\|^2$ .

The planar tire forces and moments generation is detailed in the following section, which is influenced by the vertical force acting on each tire. A simplified suspension model is used in this work, aligned with the rigid-body assumption: each suspension quarter has an equivalent linear spring-damper system that is directly actuated and normal to the ground plane. For this suspension model, the vertical force is given by

$$F_z(t) = \frac{k}{MR^2} \Delta(t) + \frac{c}{MR^2} \dot{\Delta}(t) \text{ [N];} \quad (2.13)$$

in which  $k$  and  $c$  are the elastic and damping coefficients of the linear spring-damper systems, respectively. To correct the fact that the real suspension mechanism is not directly actuated but through a series of mechanisms (via pushrods and bellcranks), the concept of motion ratio  $MR$  is introduced, which is the ratio between wheel displacement and equivalent spring/damper system displacement [19].

## 2.1.2 Tire modelling

Tires are the only element interacting simultaneously with the driving surface and the vehicle body via the suspension. The friction these create when interacting with the road is the predominant force and moment generation mechanism, producing accelerations. Given the difficulty of computing the loads analytically, several tire models exist with a similar goal: the prediction of the magnitude and direction of the friction forces and moments originated at the tire/road interface in several driving scenarios [25]. Two distinct approaches can be used to derive a tire model: using a mathematical/physical formulation or using empiric test data. Some models employ a blend of both approaches.

FST Lisboa's tire supplier is Continental AG, who provides the C19 racing tires (Competition Tire 2019), including documentation to simulate tire behaviour. Continental AG makes available the treated data from private testing, using the Magic Formula tire model, a semi-empirical model that calculates steady-state tire loads [26] [13]. The semi-empirical classification is given since the model is based on test data, but is also described by physical properties.

To be able to employ the provided tire model and compute the friction loads it produces in the tire/road interface, several concepts must be defined. For a free-rolling wheel, as shown in figure 2.2, with linear velocity  $V_w = (V_x \ V_y \ V_z)^T$  measured at the wheel centre, rotating at angular speed  $\omega_0$ , the tire effective radius  $R$  is given by

$$R = \frac{V_x}{\omega_0} \text{ [m].} \quad (2.14)$$

If a driving torque  $T$  is applied, a longitudinal tire slip  $\kappa$  occurs,

$$\kappa(t) = -\frac{V_x(t) - R \omega(t)}{V_x(t)} \quad [-], \quad (2.15)$$

known as the slip ratio, arising from the deformations of the rubber as it contacts the road. This particular formulation implies that  $\kappa \rightarrow \infty$  if the wheel is spinning (in a tire burnout, for instance) and  $\kappa = -1$  if it is locked (under hard braking). Tire slip can also occur laterally if  $V_y \neq 0$  and is defined in terms of the side slip angle  $\alpha$ ,

$$\alpha(t) = \arctan\left(\frac{V_y(t)}{V_x(t)}\right) \quad [\text{rad}]. \quad (2.16)$$

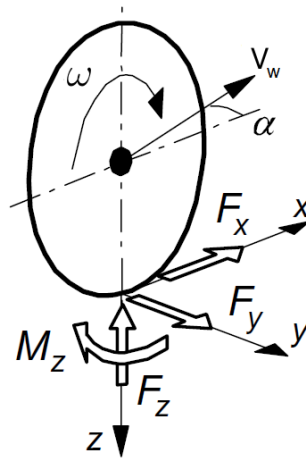


Figure 2.2: Schematic of a tire and generated forces/moment [13].

The camber angle  $\gamma$  is the angle of inward or outward tilt of the tire when looking from the rear of the vehicle. If the tire tilts inwards, which is typical in racing tires on a static configuration,  $\gamma < 0$ . The tilt provides extra cornering force when compared to a fully vertical tire caused by a more uniform tire footprint and reduces tire drag in longitudinal acceleration due to a smaller tire footprint.

The friction coefficient  $\mu$  is defined as the ratio between longitudinal/lateral force and vertical load:

$$\mu_x = \frac{F_x}{F_z} \quad [-]; \quad (2.17)$$

$$\mu_y = \frac{F_y}{F_z} \quad [-]; \quad (2.18)$$

and depends on tire-road traction conditions. One can consider, for simplicity,

$$\mu = \mu_x = \mu_y \quad [-]; \quad (2.19)$$

corresponding to isotropic levels of traction in terms of  $F_x$  and  $F_y$ .

The tire model provided by Continental AG is valid within the boundaries defined in table 2.1, which covers a wide range of possible operating conditions.

Table 2.1: Boundaries of the parameters used in the tire model.

Parameter	Minimum value	Maximum value
Vertical load ( $F_z$ )	230 [N]	1600 [N]
Slip ratio ( $\kappa$ )	-0.25 [-]	0.25 [-]
Slip angle ( $\alpha$ )	-0.20 [rad]	0.20 [rad]
Camber angle ( $\gamma$ )	-0.10 [rad]	0.10 [rad]

### Magic Formula for pure slip conditions

Pure longitudinal slip ( $\alpha = 0$  [rad]) and pure lateral slip ( $\kappa = 0$  [-]) represent the driving scenarios where only one of the slip quantities varies. Having defined the concepts associated with tire mechanics, it is now possible to state the formula that baptises the model. Indeed, for provided values of vertical load  $F_z$ , friction coefficient  $\mu$  and camber angle  $\gamma$ , the Magic Formula can be expressed as [13]

$$y(x(t)) = D \sin(C \arctan(B x(t) - E(B x(t) - \arctan(B x(t))))), \quad (2.20)$$

with

$$Y(X(t)) = y(x(t)) + S_V, \quad (2.21)$$

$$x(t) = X(t) + S_H. \quad (2.22)$$

The input variable is  $X$ , which can be  $\kappa$  or  $\alpha$ , and the output variable is  $Y$ , which can be  $F_x$ ,  $F_y$  or  $M_z$ . To compute  $F_x$ , the input variable is  $\kappa$ ; to compute  $F_y$  and  $M_z$  the input variable is  $\alpha$ .  $B$ ,  $C$ ,  $D$  and  $E$  are fixed coefficients for provided  $(F_z, \mu, \gamma)$  conditions: stiffness factor, shape factor, peak value and curvature factor, respectively. To have a better fit of the curves to tire test data, components  $S_V$  and  $S_H$  allow vertical and horizontal curve shifts, respectively. The shifts present in the data might be caused by ply-steer, conicity or rolling resistance effects [13].

Throughout this thesis, the design values for the friction coefficient and camber angle are considered  $\mu = 1$  [-] and  $\gamma = 0$  [rad], respectively. In that case, the  $F_x(\kappa)$ ,  $F_y(\alpha)$  and  $M_z(\alpha)$  tire curves depend solely on  $F_z$ , and have the typical shapes shown in figure 2.3, for several instances of  $F_z$ .

Considering driving surfaces made of tarmac or concrete - as the ones the Formula Student prototype will likely encounter -  $Y(X)$  increases up to a certain  $\kappa_{critical}$  or  $\alpha_{critical}$ , where it reaches a maximum, and decreases afterwards in a tire-specific rate. The opposite is true for negative  $\kappa$  and  $\alpha$  values, in which a minimum for  $Y(X)$  is reached. Tire operating conditions in which  $|\kappa| > \kappa_{critical}$  and  $|\alpha| > \alpha_{critical}$  occur frequently in motorsports if no traction control is employed, due to the high power-to-weight ratios, accelerations and mass transfers. Tire states in which  $|\kappa| > \kappa_{critical}$  and/or  $|\alpha| > \alpha_{critical}$  should generally be avoided since they represent an unstable setting, with a danger of quick force/moment drop-off, causing the vehicle to slide or skid unpredictably across the race track. Generally, racing tires are "less forgiving" for the driver after  $\kappa_{critical}$  and/or  $\alpha_{critical}$  are exceeded (in terms of force/moment drop-off), comparing with standard tires. However, a good racing driver/computer emulating the driver should be able to consistently drive the car in operating conditions that are close to  $\kappa_{critical}$  and  $\alpha_{critical}$  to achieve highest possible accelerations and thus the minimum lap time.

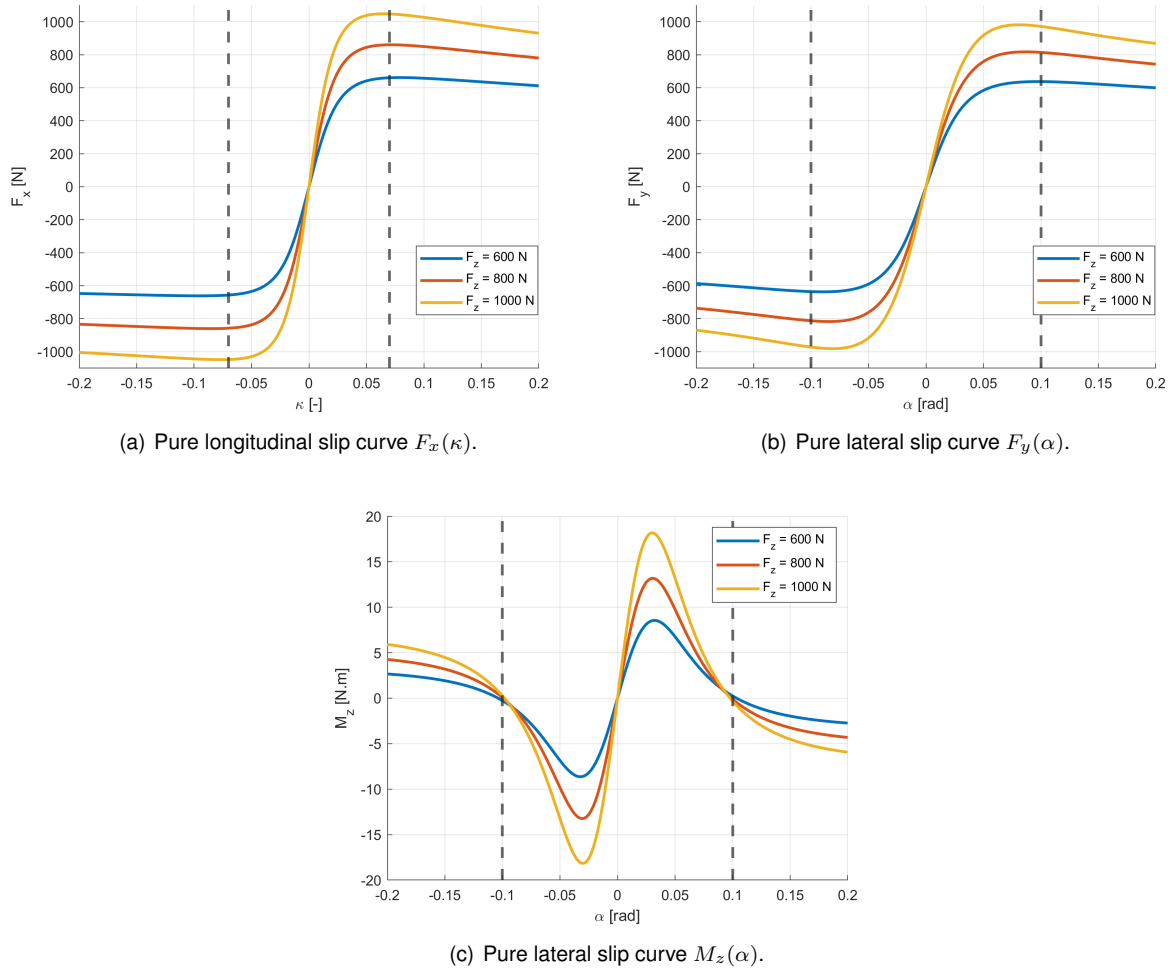


Figure 2.3: Typical pure slip curves for the Magic Formula tire model.

From the tire curves from figure 2.3, it can be seen that  $\kappa_{critical} \approx 0.07$  [-] (for peak longitudinal performance) and  $\alpha_{critical} \approx 0.1$  [rad] (for peak lateral performance). In practice, it is not feasible to have all four tires working in the peak performance regions at all times.

The slopes of the pure slip curves from figure 2.3 near the origin represent the regions where tires show a linear slip versus force/moment relationship. These regions occur approximately, irrespective of vertical load, for  $\kappa \in [-0.025, 0.025]$  [-] and  $\alpha \in [-0.04, 0.04]$  [rad]. The slopes are termed longitudinal slip stiffness ( $C_\kappa$ ), cornering stiffness ( $C_\alpha$ ) and self-aligning stiffness ( $C_{\alpha M}$ ), respectively. For these regions, admitting  $\gamma = 0$  [rad], one obtains:

$$F_x(t) = C_\kappa \kappa(t) \text{ [N];} \quad (2.23)$$

$$F_y(t) = C_\alpha \alpha(t) \text{ [N];} \quad (2.24)$$

$$M_z(t) = C_{\alpha M} \alpha(t) \text{ [N.m].} \quad (2.25)$$

Referring to figure 2.4, the coefficients of the Magic Formula (2.20) are computed as follows. Coeffi-

cient  $D$  represents the peak value with respect to the  $x$  axis, simply:

$$D = y_{max}. \quad (2.26)$$

The shape factor  $C$ , which controls the range of the sine function and its shape, is given by:

$$C = 1 \pm \left( 1 - \frac{2}{\pi} \arcsin \left( \frac{y_a}{D} \right) \right). \quad (2.27)$$

The product  $BCD$  corresponds to the slope at the origin ( $x = y = 0$ ). Finally, it is possible to determine  $E$ , which simultaneously controls the curvature at the peak and its horizontal position:

$$E = \frac{B x_m - \tan \left( \frac{\pi}{2C} \right)}{B x_m - \arctan(B x_m)} \quad (2.28)$$

Shifts  $S_V$  and  $S_H$  are considered null, as an approximation for ideal tire curves.

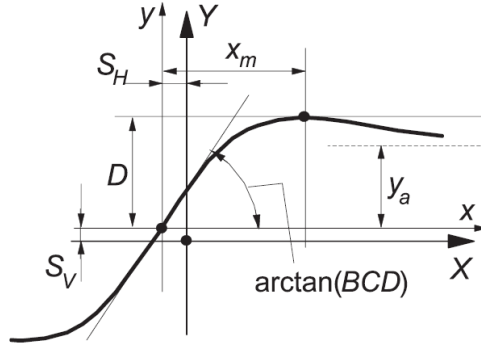


Figure 2.4: Tire curve produced by the Magic Formula, with the respective curve parameters. [13].

To experimentally identify the Magic Formula parameters only once, and still capture the effect of expansion proportional to  $F_z$ , depicted in figure 2.3, parameter  $D$  is defined as:

$$D(t) = \mu F_z(t); \quad (2.29)$$

and the remaining parameters are determined for the normalized curves in terms of vertical load ( $F_z = 1$  [N]), shown in table 2.2. Parameter  $D$  is computed online and, according to the particular tire vertical load  $F_z(t)$ , expands the tire curves defined by (2.20) accordingly.

Table 2.2: Magic formula coefficients for pure-slip tire curves.

Pure-slip curve	$B$	$C$	$E$	$D(t)$
$F_x(\kappa)$	20	1.9	0.6	$\mu F_z(t)$
$F_y(\alpha)$	10	2.2	0.5	$\mu F_z(t)$
$M_z(\alpha)$	10	0.05	5	$\mu F_z(t)$

## Magic Formula for combined slip conditions

A drop in tire force occurs if, for a tire with a given  $\kappa$ , a component  $\alpha$  is added or vice-versa. This phenomenon is known as combined tire slip [13]. Even though it is useful to consider longitudinal and lateral forces associated to slip ratios and slip angles, in reality, the tire rubber simply produces a resultant force and a resultant slip velocity [7]. Still, driving instances where there are combined slip conditions are common in motorsports, for instance when braking and turning before a curve apex and when accelerating and turning after it.

Since slip ratio (fraction of relative speeds) and slip angle (measured in radians) aren't commensurable, they cannot be used directly to compute an equivalent slip vector [27]. Recovering the critical values for the pure longitudinal and lateral tire curves,  $\kappa_{critical}$  (slip ratio for which  $F_x(\kappa, F_z)$  reaches the maximum) and  $\alpha_{critical}$  (slip angle for which  $F_y(\alpha, F_z, \gamma)$  reaches the maximum), it is possible to define the non-dimensional slip quantities  $s$  and  $a$ ,

$$s(t) = \frac{\kappa(t)}{\kappa_{critical}} \quad [-]; \quad (2.30)$$

$$a(t) = \frac{\alpha(t)}{\alpha_{critical}} \quad [-]. \quad (2.31)$$

Since  $s$  and  $a$  are unitless, a normalised combined slip magnitude  $\rho$  is defined as

$$\rho(t) = \sqrt{s(t)^2 + a(t)^2} \quad [-]. \quad (2.32)$$

Finally, the Magic Formula for pure slip conditions (2.20) can be updated to include combined slip:

$$F_x(t) = \frac{s(t)}{\rho(t)} D_\kappa \sin(C_\kappa \arctan(B_\kappa \rho(t) \kappa_{critical} - E_\kappa(B_\kappa \rho(t) \kappa_{critical} - \arctan(B_\kappa \rho(t) \kappa_{critical})))) \quad [\text{N}]; \quad (2.33)$$

$$F_y(t) = \frac{a(t)}{\rho(t)} D_\alpha \sin(C_\alpha \arctan(B_\alpha \rho(t) \alpha_{critical} - E_\alpha(B_\alpha \rho(t) \alpha_{critical} - \arctan(B_\alpha \rho(t) \alpha_{critical})))) \quad [\text{N}]. \quad (2.34)$$

Figure 2.5 shows the surfaces corresponding to the evolutions of the normalised forces  $F_x(\kappa, \alpha)$  and  $F_y(\kappa, \alpha)$ , clearly showing the tire force drop-off when a component of  $\alpha$  is added to the pure longitudinal slip curve (figure 2.5(a)) and when a component of  $\kappa$  is added to the pure lateral slip one (figure 2.5(b)).

Tire forces and moments generate longitudinal and lateral accelerations in the chassis,  $a_x$  and  $a_y$ . As stated in [7], the goal in racing is to maintain the highest possible acceleration level in the appropriate direction. The G-G diagram, as exemplified in figure 2.6, helps understand the dynamic vehicle behaviour in terms of accelerations  $a_x$  and  $a_y$ , plotted at a given frequency (two hundred samples per second, in this particular case). The accelerations are typically expressed in [g], in which  $1 \text{ [g]} = 9.81 \text{ [m/s}^2\text{]}$ , approximately the acceleration of gravity. Pure longitudinal dynamics, such as accelerating (positive  $a_x$  values) and decelerating (negative  $a_x$  values), will only show points along the vertical axis; while pure lateral dynamics will mainly show points along the horizontal one. For a generic racing instance, the points will be scattered along the four quadrants of the diagram. Vehicle performance can be assessed based on the maximum/average acceleration values that the vehicle experiences while driving around a

race track, being useful to rank the evolution of setup changes or, in the scope of this thesis, the traction controllers effectiveness.

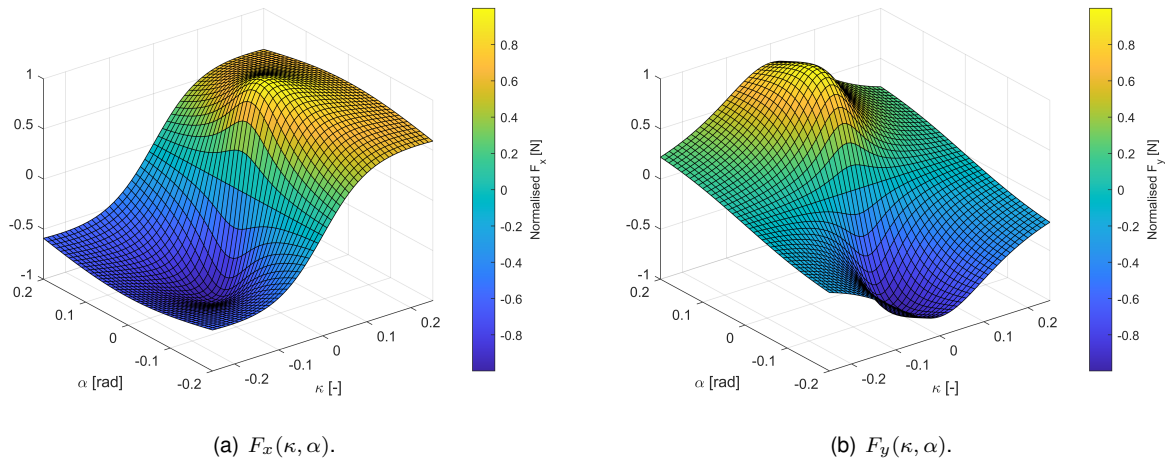


Figure 2.5: Longitudinal and lateral force surfaces as function of tire slip ratio and angle.

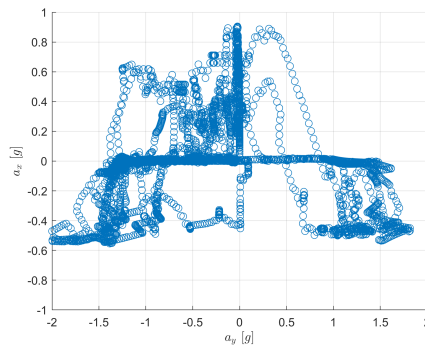


Figure 2.6: Example of a measured G-G diagram of a Formula Student prototype.

### 2.1.3 Powertrain modelling

FST Lisboa employ electric powertrains with in-wheel motors, which may run as four-wheel-driven (4WD) or rear-wheel driven (RWD). For both configurations, the motors are permanent-magnet, synchronous machines (PMSM) built by AMK GmbH, characterized in table 2.3. Each motor is independently controlled in speed-control operating mode, which allows a dynamic limitation of both speed and torque references [28].

The rules of the Formula Student competitions [5] state that the cumulative power must not exceed 80 [kW] or, more formally,

$$\sum_i |V_{m_i}(t) I_{m_i}(t)| \leq 80000 \text{ [W]}; \quad (2.35)$$

$i = 1, 2, 3, 4$  for 4WD and  $i = 3, 4$  for RWD;  $V_m$  and  $I_m$  are the motor voltage and current. Since the peak power for each motor is  $P_{max} = 35$  [kW], the requirement stated in (2.35) is always satisfied for RWD, where only two motors are employed. However, if the car runs as 4WD, a power distribution control loop

Table 2.3: Electric motor characterisation from a mechanical standpoint.

Parameter	Symbol	Value, [units]
Nominal speed	$N_{nom}$	12000 [rpm]
Nominal torque	$T_{nom}$	10 [N.m]
Nominal power	$P_{nom}$	12.3 [kW]
Maximum speed	$N_{max}$	20000 [rpm]
Maximum torque	$T_{max}$	21 [N.m]
Maximum power	$P_{max}$	35 [kW]

must be implemented to power the four motors adequately.

The motor torque and power curves are sketched in figure 2.7 for the range of motor speeds, as per the manufacturer documentation [28]. The orange curve stands for nominal operating conditions, under which the motor can operate with "infinite" life, and the blue curve represents peak performance conditions, in which the motor can briefly operate.

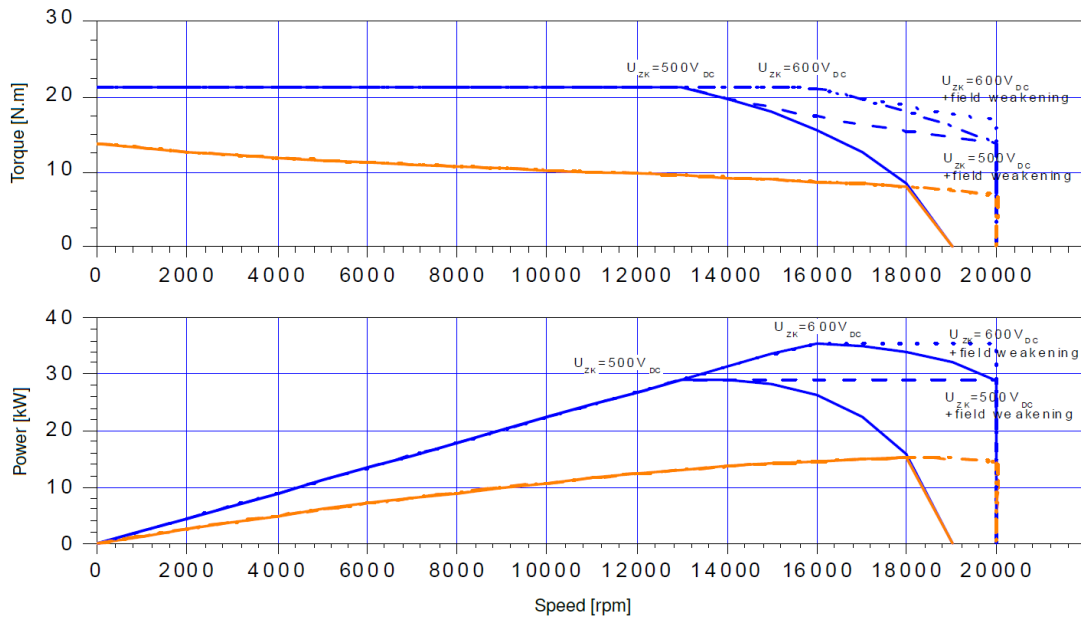


Figure 2.7: Torque and power curves of the electric motor. [28].

Motor efficiency is considered as per table 2.4. The region of high motor efficiency  $\eta_{motor} > 80$  [%] is highlighted. The efficiency in generator-operating mode is given by the inverse values of table 2.4, for negative motor torques. Knowing the motor speed and requested torque command, a look-up table is used to determine the motor efficiency for the operating conditions, using a cubic interpolation between entries.

The electric motors spin at extremely high speeds with relatively low torques, so a gear reduction is necessary. FST Lisboa use a planetary gear train with a fixed gear ratio,  $GR = 16.25$  [-], such that the torque at wheel  $i$  is given by

$$T_{w_i}(t) = T_{m_i}(t) GR \text{ [N.m].} \quad (2.36)$$



Table 2.4: Motor efficiency for the range of speeds and torques.

		Motor speed [rpm]									
		500	1000	2000	3000	4000	6000	10000	12000	15000	19000
Motor torque [N.m]	1.3	64.37	71.33	73.64	74.7	75.43	76.57	77	77.08	77.56	78.14
	2.7	58.42	70.48	77.57	80.4	82.01	83.92	85.16	85.44	85.97	86.5
	5.4	44.94	60.81	73.35	78.82	81.94	85.43	88.2	88.88	89.71	90.44
	7.9	35.59	51.9	67.02	74.26	78.54	83.42	87.58	88.65	89.84	90.86
	10.4	29.14	44.78	61.01	69.41	74.57	80.62	85.93	87.34	88.86	90.16
	12.5	24.17	38.71	55.22	64.39	70.24	77.3	83.73	85.48	87.37	88.98
	14.4	20.41	33.76	50.04	59.65	65.99	73.88	81.33	83.42	85.66	87.59
	16	17.31	29.4	45.1	54.87	61.55	70.1	78.56	80.97	83.56	85.81
	17.4	14.82	25.75	40.67	50.41	57.28	66.34	75.7	78.4	81.34	82.71
	18.5	12.81	22.67	36.72	46.3	53.25	62.67	72.77	75.75	79.02	76.96
	19.6	11.17	20.05	33.21	42.51	49.44	59.09	69.82	73.06	67.66	69.28

Conversely, the angular speed of wheel  $i$  is given by

$$\omega_i(t) = \frac{\omega_{m_i}(t)}{GR} \text{ [rad/s]}. \quad (2.37)$$

Since the numerical modelling of the PMSM is outside the scope of this thesis, the torque response dynamics are approximated by a first-order system:

$$G_{PT}(s) = \frac{\eta_{PT}}{t_{PT}s + 1}, \quad (2.38)$$

where  $\eta_{PT} = 0.90$  [-] is the equivalent powertrain efficiency that considers the accumulator, inverters, electrical connections and drivetrain (considered constant);  $t_{PT} = 0.02$  [s] is the time constant of the torque dynamics.

## 2.1.4 Steering modelling

The rotation of a steering wheel or an actuator - in the driverless case - induces a steering angle in the tires. FST Lisboa's vehicles are only front-wheel steered, as shown by the tire steering angles  $\delta_1$  and  $\delta_2$  in figure 2.8.

From a kinematics perspective, if both front tires are steered by the same angular amount, the outer tire would start skidding, since the radius of curvature that each wheel must describe is different. To allow for  $\delta_1 \neq \delta_2$  and consequently avoid tire skid, the Ackermann steering geometry may be employed, as shown in figure 2.8. This principle is applicable to low-speed/low curvature curves [7], such as the ones found in typical Formula Student race tracks.

The steering of a Formula Student prototype is not direct, which means that the steering wheel has a higher rotation than that of the tires  $i = 1, 2$ . Formally,  $SR > 1$  [-], with the steering ratio being defined as

$$SR = \frac{\delta(t)}{\delta_i(t)} \text{ [-]}. \quad (2.39)$$

According to the Ackermann steering geometry, the steering angles  $\delta_1$  and  $\delta_2$  can be computed as:

$$\delta_1(t) = \arctan \left( \frac{(L_f + L_r) \tan(\delta(t)/SR)}{L_f + L_r - \frac{L_t}{2} \tan(\delta(t)/SR)} \right) \text{ [rad];} \quad (2.40)$$

$$\delta_2(t) = \arctan \left( \frac{(L_f + L_r) \tan(\delta(t)/SR)}{L_f + L_r + \frac{L_t}{2} \tan(\delta(t)/SR)} \right) \text{ [rad];} \quad (2.41)$$

in which  $L_f$ ,  $L_r$  and  $L_t$  are the distance from the CG to the front axle, from the CG to the rear axle, and the track width, respectively.

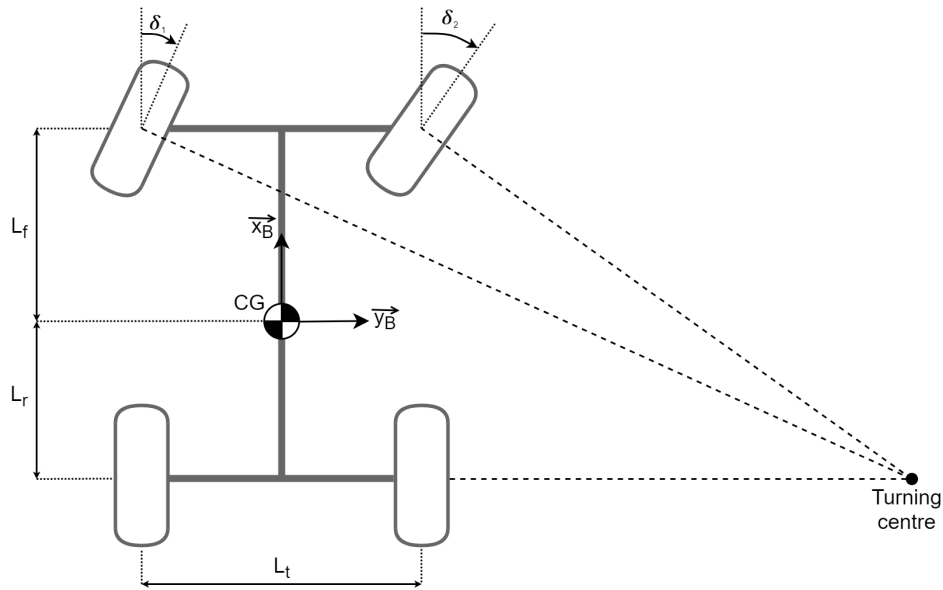


Figure 2.8: Ackermann steering geometry.

Similarly to the powertrain modelling, the steering angle actuation is also modelled as a first-order system as

$$G_{STA}(s) = \frac{1}{SR(t_{STA}s + 1)}, \quad (2.42)$$

where  $t_{STA} = 0.1$  [s] is the steering actuation time constant.

## 2.2 Simplified vehicle models

Two common categories of simplified vehicle models are kinematic and dynamic ones. Kinematic models ignore inertial effects and tire-road interactions, being suitable for low-speed path planning and control. The no-slip assumption between the tires and road is valid for instance in parking manoeuvres or most urban driving situations. On the other hand, if the vehicle experiences high enough accelerations, that assumption may lead to erroneous results, as in a racing scenario. For these instances, dynamic models may be more accurate [29]. It is preferable to use dynamic models to study a Formula Student prototype since they fall into to the category of vehicles subject to high accelerations.

In this section, several simplified dynamic models are introduced: a planar (bicycle) model, a uni-dimensional (unicycle) model and a combined model that is used for control design. Lastly, a brief explanation of dynamic mass transfers is given, since they influence vehicle traction.

### 2.2.1 Bicycle model

The planar dynamics describes the motion in an horizontal plane, which has three DOF: translation in the  $\vec{x}_G$  and  $\vec{y}_G$  directions and rotation about the  $\vec{z}_G$  axis. According to the Newton-Euler equations for a rigid body planar motion [30], one wishes to determine the equivalent loading that acts on the vehicle CG: forces  $F_{xCG}$  and  $F_{yCG}$  and moment  $M_{zCG}$  such that

$$F_{xCG}(t) = m(\dot{u}(t) - v(t) r(t)) \Leftrightarrow \dot{u}(t) = \frac{F_{xCG}(t)}{m} + v(t) r(t) \quad [\text{m/s}^2]; \quad (2.43)$$

$$F_{yCG}(t) = m(\dot{v}(t) + u(t) r(t)) \Leftrightarrow \dot{v}(t) = \frac{F_{yCG}(t)}{m} - u(t) r(t) \quad [\text{m/s}^2]; \quad (2.44)$$

$$M_{zCG}(t) = I_{zz} \dot{r}(t) \Leftrightarrow \dot{r}(t) = \frac{M_{zCG}(t)}{I_{zz}} \quad [\text{rad/s}^2]; \quad (2.45)$$

where  $I_{zz}$  is entry (3,3) of the inertia tensor  $J_{CG}$ , also known as rotational inertia.

Considering the free-body diagram in figure 2.9, the equivalent loading on the CG is given by

$$F_{xCG}(t) = \sum_i F_{x_i}(t) \cos(\delta_i(t)) - F_{y_i}(t) \sin(\delta_i(t)) \quad [\text{N}]; \quad (2.46)$$

$$F_{yCG}(t) = \sum_i F_{x_i}(t) \sin(\delta_i(t)) + F_{y_i}(t) \cos(\delta_i(t)) \quad [\text{N}]; \quad (2.47)$$

$$M_{zCG}(t) = \sum_i M_{z_i}(t) + y_i(F_{x_i}(t) \cos(\delta_i(t)) - F_{y_i}(t) \sin(\delta_i(t))) + x_i(F_{y_i}(t) \cos(\delta_i(t)) + F_{x_i}(t) \sin(\delta_i(t))) \quad [\text{N.m}]. \quad (2.48)$$

Since the vehicle is only front-wheel steered,  $\delta_3 = \delta_4 = 0$  [rad];  $x_i$  and  $y_i$  are the lever arms defined in table 2.5.

Table 2.5: List of lever arms for  $M_z$  computation for tire  $i$ .

$i$	1	2	3	4
$x_i$	$L_f$	$L_f$	$-L_r$	$-L_r$
$y_i$	$\frac{L_t}{2}$	$-\frac{L_t}{2}$	$\frac{L_t}{2}$	$-\frac{L_t}{2}$

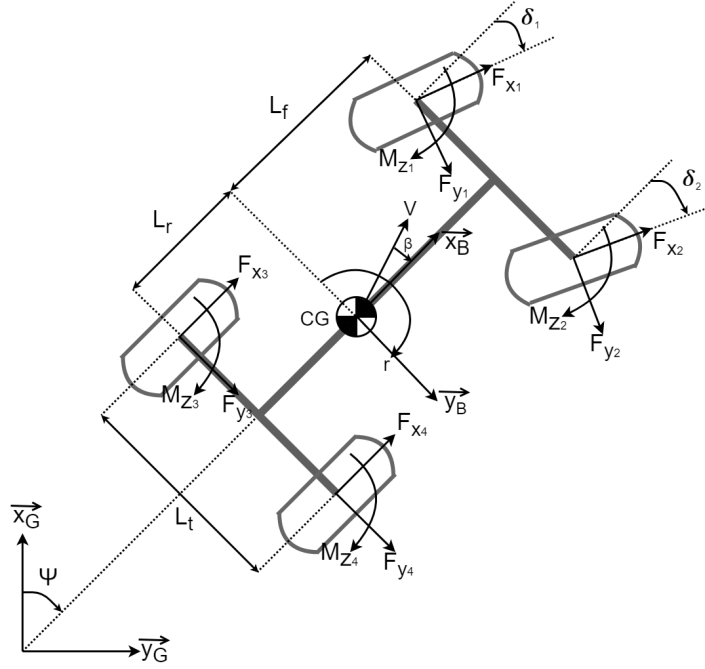


Figure 2.9: Free-body diagram for planar motion.

The planar velocity  $\dot{P}_G$  can be expressed in the global reference frame as

$$\begin{pmatrix} \dot{x}_G(t) \\ \dot{y}_G(t) \\ \dot{\psi}(t) \end{pmatrix} = \begin{pmatrix} \cos(\psi(t)) & -\sin(\psi(t)) & 0 \\ \sin(\psi(t)) & \cos(\psi(t)) & 0 \\ 0 & 0 & 1 \end{pmatrix} \begin{pmatrix} u(t) \\ v(t) \\ r(t) \end{pmatrix}. \quad (2.49)$$

Finally, the planar pose (position and orientation) can be obtained by integrating  $\dot{P}_G$  in time as

$$x_G(t) = x_{G_0} + \int_{t_0}^t \dot{x}_G(t) dt \quad [\text{m}]; \quad (2.50)$$

$$y_G(t) = y_{G_0} + \int_{t_0}^t \dot{y}_G(t) dt \quad [\text{m}]; \quad (2.51)$$

$$\psi(t) = \psi_0 + \int_{t_0}^t \dot{\psi}(t) dt \quad [\text{rad}]; \quad (2.52)$$

where  $x_{G_0}$ ,  $y_{G_0}$  and  $\psi_0$  represent the respective initial conditions,  $t_0$  and  $t$  the temporal limits of integration.

To further simplify the planar vehicle model, it can be thought of as a single-track entity, resembling a bicycle, as depicted in figure 2.10. The front and rear axles are now condensed into a single wheel for each. There is now a single steering angle  $\delta_f$ , the front axle has no longitudinal force component, and the self-aligning moments are considered null. A simplified Magic Formula tire model is employed. This model aims to represent a rear-wheel driven car with front-wheel steering.

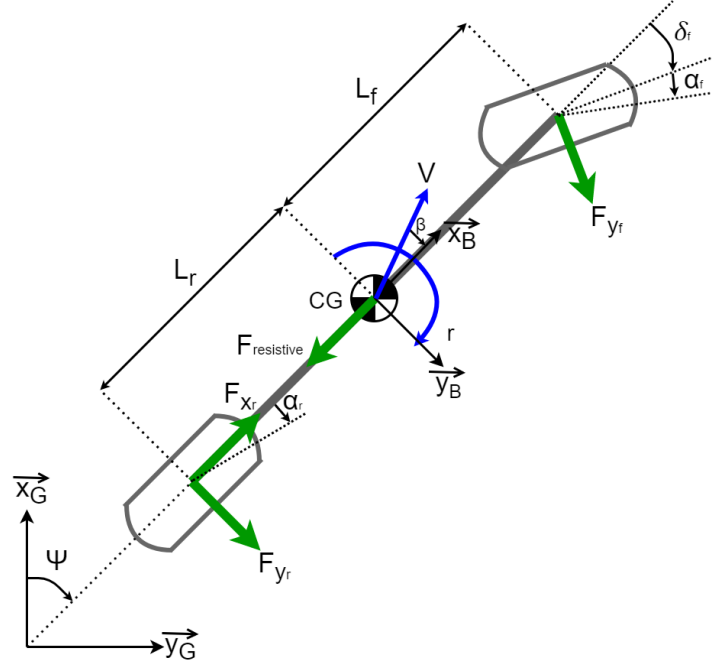


Figure 2.10: Schematic of the bicycle model.

Applying equations 2.46-2.48 (planar motion) to the bicycle model, one concludes:

$$\dot{u}(t) = \frac{1}{m}(-F_{y_f}(t) \sin(\delta_f(t)) + F_{x_r}(t)) + v(t) r(t) \quad [\text{m/s}^2]; \quad (2.53)$$

$$\dot{v}(t) = \frac{1}{m}(F_{y_f}(t) \cos(\delta_f(t)) + F_{y_r}(t)) - u(t) r(t) \quad [\text{m/s}^2]; \quad (2.54)$$

$$\dot{r}(t) = \frac{1}{I_{zz}}(F_{y_f}(t) \cos(\delta_f(t)))L_f - F_{y_r}(t) L_r \quad [\text{rad/s}^2]. \quad (2.55)$$

The side slip of a car  $\beta$  is defined as the angle between the vehicle's heading and its velocity vector [31],

$$\beta(t) = \arctan\left(\frac{v(t)}{u(t)}\right) \quad [\text{rad}]. \quad (2.56)$$

Since all tires deform laterally to compensate for the body sideslip, this notion can be applied to tire  $i$  as

$$\beta_i(t) = \alpha_i(t) + \delta_i(t) \quad [\text{rad}], \quad (2.57)$$

where  $\alpha_i$  [rad] is the slip angle present in tire  $i$ . Since, in the bicycle mode, the vehicle is viewed as a two-wheel entity with front-wheel steering, the slip angles of the front and rear tires are given by:

$$\alpha_f(t) = \arctan\left(\frac{v(t) + r(t) L_f}{u(t)}\right) - \delta_f(t) \quad [\text{rad}]; \quad (2.58)$$

$$\alpha_r(t) = \arctan\left(\frac{v(t) - r(t) L_r}{u(t)}\right) \quad [\text{rad}]. \quad (2.59)$$

Considering a simplified version of the Magic Formula (2.20), tire forces can be computed as:

$$F_{x_r}(t) = 2 D_{R_{\kappa}} \sin(C_{R_{\kappa}} \arctan(B_{R_{\kappa}} \kappa(t))) \quad [\text{N}]; \quad (2.60)$$

$$F_{y_f}(t) = -2 D_{F_\alpha} \sin(C_{F_\alpha} \arctan(B_{F_\alpha} \alpha(t))) \text{ [N]}; \quad (2.61)$$

$$F_{y_r}(t) = -2 D_{R_\alpha} \sin(C_{R_\alpha} \arctan(B_{R_\alpha} \alpha(t))) \text{ [N]}. \quad (2.62)$$

The factor of 2 represents the effects of both wheels of the front and rear axles;  $B$ ,  $C$  and  $D$  are the Magic Formula Parameters according to table 2.2.

## 2.2.2 Unicycle model

The highest degree of simplification for a vehicle model admits only one dimension, in which it can only accelerate and decelerate, without turning. The unicycle model depicted in figure 2.11 considers a single wheel bearing the vehicle mass.

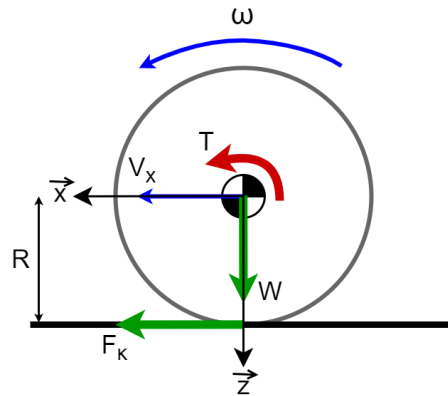


Figure 2.11: Schematic and free-body diagram of the unicycle model.

In this unidimensional model, a wheel with effective radius  $R$  receives an input torque  $T$  and rotates with an angular speed  $\omega$ . The tire-road interaction creates a traction force that propels the vehicle longitudinally  $F_\kappa$ , proportional to the slip ratio  $\kappa$ , as shown in figure 2.3(a). The wheel has a rotational inertia  $J_w$  and carries a weight  $W$ . One is interested in obtaining the equations that govern the dynamics of the unidimensional vehicle model. A force balance along the  $\vec{x}$  axis reveals that

$$\sum F_x(t) = m \dot{V}_x(t) = F_\kappa(t) \text{ [N]}. \quad (2.63)$$

A moment balance around the  $\vec{y}$  axis shows that

$$\sum M_y(t) = J \dot{\omega}(t) = -F_\kappa(t) R + T(t) \text{ [N.m]}. \quad (2.64)$$

A linear tire model is desirable, to have a simple and intuitive representation of the system. Choosing the operating tire conditions within the linear range of the pure longitudinal slip curve from figure 2.3(a), where equation (2.23) holds, then equations (2.63) and (2.64) become

$$\dot{V}_x(t) = \frac{C_\kappa \kappa(t)}{m} \text{ [m/s}^2\text{]}; \quad (2.65)$$

$$\dot{\omega}(t) = \frac{-C_{\kappa} \kappa(t) R + T(t)}{J} \text{ [rad/s}^2\text{]}. \quad (2.66)$$

To control  $\kappa$  explicitly, and not as a consequence of  $V_x$  and  $\omega$ , it is useful to define it as a state variable. Considering, from equation (2.15), that

$$\omega(t) = \frac{V_x(t)(1 + \kappa(t))}{R} \text{ [rad/s]}, \quad (2.67)$$

equation (2.66) becomes

$$\frac{\dot{V}_x(t)(1 + \kappa(t)) + V_x(t) \dot{\kappa}(t)}{R} = \frac{-C_{\kappa} \kappa(t) R + T(t)}{J} \quad (2.68)$$

$$\Leftrightarrow \dot{\kappa}(t) = \frac{R}{J V_x(t)} (-C_{\kappa} \kappa(t) R + T(t)) - \frac{\dot{V}_x(t)}{V_x(t)} (1 + \kappa(t)) \text{ [s}^{-1}\text{]}. \quad (2.69)$$

### 2.2.3 Model used for control design

The vehicle model used for control design is an extension of the dynamic bicycle one, derived in section 2.2.1. To capture the tire-road interaction, an additional state - tire slip ratio  $\kappa$  - is introduced, analogous to the unicycle model presented in section 2.2.2, which is directly influenced by the input motor torque  $T_m$ . Additionally, a yawing moment due to torque vectoring  $T_{TV}$  is also considered as an input and included in the yaw rate equilibrium equation. The model, summarised in equations (2.70)-(2.73) represents a RWD car with longitudinal and lateral tire slip dynamics, front-wheel steering and torque vectoring possibility.

$$\dot{u}(t) = \frac{1}{m} (-F_{y_f}(t) \sin(\delta_f(t)) + F_{x_r}(t) - C_t u^2(t)) + v(t) r(t) \text{ [m/s}^2\text{]}; \quad (2.70)$$

$$\dot{\kappa}(t) = \frac{R}{J_w u(t)} \left( -\frac{F_{x_r}(t)}{2} R + T_m(t) GR \right) - \frac{\dot{u}(t)}{u(t)} (1 + \kappa(t)) \text{ [s}^{-1}\text{]}; \quad (2.71)$$

$$\dot{v}(t) = \frac{1}{m} (F_{y_f}(t) \cos(\delta_f(t)) + F_{y_r}(t)) - u(t) r(t) \text{ [m/s}^2\text{]}; \quad (2.72)$$

$$\dot{r}(t) = \frac{1}{I_{zz}} (F_{y_f}(t) \cos(\delta_f(t)) L_f - F_{y_r}(t) L_r + T_{TV}(t)) \text{ [rad/s}^2\text{]}. \quad (2.73)$$

The tire forces are given by:

$$F_{x_r}(t) = \frac{2 m g}{4} \sin(1.9 \arctan(20 \kappa(t))) \text{ [N]}; \quad (2.74)$$

$$F_{y_f}(t) = -\frac{2 m g}{4} \sin(2.2 \arctan(10 \alpha_f(t))) \text{ [N]}; \quad (2.75)$$

$$F_{y_r}(t) = -\frac{2 m g}{4} \sin(2.2 \arctan(10 \alpha_r(t))) \text{ [N]}; \quad (2.76)$$

in which the front and rear tire slip angles are given by equations (2.58) and (2.59), respectively. The simplified tire model includes the assumption that the vertical force acting in each tire is a quarter of the total vehicle weight. Since the front and rear axles are condensed into one tire each, the longitudinal and lateral forces are multiplied by a factor of 2. The tire-road friction coefficient is set as constant,  $\mu = 1$

[-].

If the state (2.1) and output (2.2) equations are linearised about the operating state, the linearised state-space representation is obtained [24]:

$$\dot{x}(t) = A(t) x(t) + B(t) u(t); \quad (2.77)$$

$$y(t) = C(t) x(t) + D(t) u(t); \quad (2.78)$$

where  $A$  is the state matrix,  $B$  the input matrix,  $C$  the output matrix and  $D$  the direct transmission matrix.

As shown in equations (2.70)-(2.73), the model has  $x(t) = (u \ \kappa \ v \ r)^T$  as state vector and  $u(t) = (T_m \ T_{TV} \ \delta)^T$  as input vector. To define the control strategy, the model was linearised around several trim points found while driving forward, with null steering input or tire side slip, for a range of  $u$  and  $\kappa$ . The corresponding linear, time-invariant state-space representation is:

$$\begin{pmatrix} \dot{u}(t) \\ \dot{\kappa}(t) \\ \dot{v}(t) \\ \dot{r}(t) \end{pmatrix} = \begin{pmatrix} A_{11} & A_{12} & 0 & 0 \\ A_{21} & A_{22} & 0 & 0 \\ 0 & 0 & A_{33} & A_{34} \\ 0 & 0 & A_{43} & A_{44} \end{pmatrix} \begin{pmatrix} u(t) \\ \kappa(t) \\ v(t) \\ r(t) \end{pmatrix} + \begin{pmatrix} 0 & 0 & 0 \\ B_{21} & 0 & 0 \\ 0 & 0 & B_{33} \\ 0 & B_{42} & B_{43} \end{pmatrix} \begin{pmatrix} T_m(t) \\ T_{TV}(t) \\ \delta(t) \end{pmatrix}; \quad (2.79)$$

$$y(t) = x(t). \quad (2.80)$$

The linearisation results show that the vehicle model can be divided into two decoupled subsystems:

- Longitudinal subsystem (analogous to the unicycle model): the motor torque  $T_m$  directly influences the wheel slip ratio  $\kappa$  which, in turn, influences the longitudinal speed  $u$  - a chained system. The dominant (slower) closed-loop pole is associated to the longitudinal vehicle speed, whereas the one associated to the tire slip ratio is four to five orders of magnitude faster.
- Lateral subsystem (analogous to a pure lateral model): the steering angle  $\delta$  directly affects the lateral speed  $v$  and yaw rate  $r$ , with a smaller contribution from the yawing moment due to torque vectoring  $T_{TV}$  for the latter. The eigenvalues of the subsystem's  $A$  matrix shows the same order of magnitude in terms of closed-loop pole locations. The dominant (slower) pole is associated to the yaw rate dynamics.

Both subsystems are stable in closed-loop, as well as the resulting system, since all eigenvalues have negative real components.



## 2.2.4 Dynamic mass transfers

Considering now vertical dynamics, the vehicle is subjected to two types of vertical loads: static and dynamic ones [19]. Static loads can be determined with the stationary vehicle, using weight scales, or from inspection of figure 2.9:

$$F_{z_1}^{st} = F_{z_2}^{st} = \frac{m g L_r}{2(L_f + L_r)} \text{ [N]}; \quad (2.81)$$

$$F_{z_3}^{st} = F_{z_4}^{st} = \frac{m g L_f}{2(L_f + L_r)} \text{ [N]}. \quad (2.82)$$

Dynamic loads are time-variant and occur when the vehicle is moving, because of load transfer and aerodynamics. Load transfer is a consequence of inertial reaction forces and the CG location, being classified as longitudinal and lateral load transfer [7]. The interaction between the moving vehicle and the air originates two types of forces, drag and lift/downforce. These phenomena are important since a tire force/moment generation capacity is influenced by the vertical load acting on it, as made evident in figure 2.3.

In the following formulas, the vehicle weight  $W = m g$  [N] is divided into the respective components: for front and rear axle considerations,  $W = W_{front} + W_{rear}$  [N]; for right and left side considerations,  $W = W_{left} + W_{right}$  [N], considering  $W_{left} = W_{right}$  [N] due to symmetry.

If a car performs a positive longitudinal acceleration  $a_x$ , the front axle is unloaded and some vertical load is transferred to the rear axle, as shown in figure 2.12; the opposite is for a deceleration. The equilibrium of moments around point  $O$  shows

$$\frac{W a_x(t) L_h}{g} = \Delta W_{rear}^{weight}(t)(L_f + L_r) \Leftrightarrow \Delta W_{rear}^{weight}(t) = \frac{W a_x(t) L_h}{g(L_f + L_r)} \text{ [N]}. \quad (2.83)$$

Regarding the front axle, the variation is necessarily symmetrical,

$$\Delta W_{front}^{weight}(t) = -\Delta W_{rear}^{weight}(t) \text{ [N]}. \quad (2.84)$$

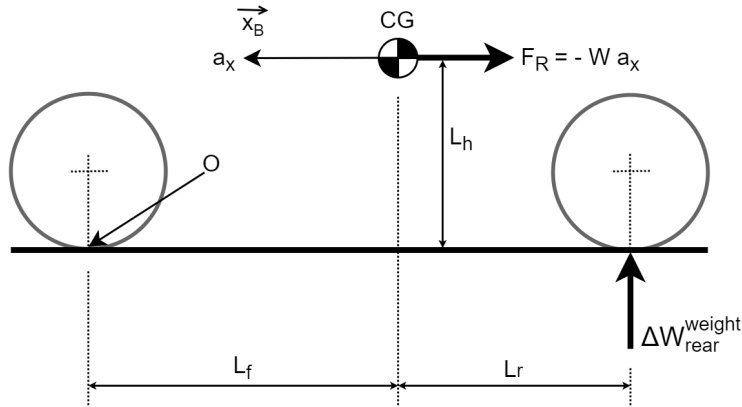


Figure 2.12: Longitudinal weight transfer in acceleration [7].

In a steady-state turn, the inside wheels (right wheels for a right-hand turn/left wheels for a left-

hand turn) become unloaded and some vertical load is transferred to the outside ones due to a lateral acceleration  $a_y$ . Regarding the lateral load transfer depicted in figure 2.13, the equilibrium of moments around point  $O$  shows

$$\frac{W a_y(t) L_h}{g} = \Delta W_{rear}^{weight}(t)(L_f + L_r) \Leftrightarrow \Delta W_{rear}^{weight}(t) = \frac{W a_y(t) L_h}{g L_t} \quad [\text{N}]. \quad (2.85)$$

Similarly, regarding the right side of the vehicle, the variation is symmetrical,

$$\Delta W_{right}^{weight}(t) = -\Delta W_{left}^{weight}(t) \quad [\text{N}]. \quad (2.86)$$

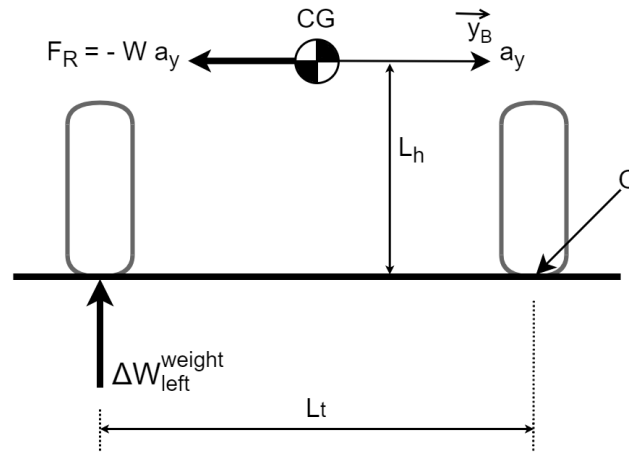


Figure 2.13: Lateral weight transfer in a right-hand turn [7].

The other source of dynamic loading is the aerodynamics loads - drag and lift - which act on the vehicle centre of pressure (CP). Unlike tire forces, which are considered independent of velocity in this thesis, aerodynamic forces increase rapidly with velocity [7]. Aerodynamic drag is a driving resistance that is parallel and opposite to the velocity vector (approximately horizontal), given by (2.87). It has a significant effect on longitudinal acceleration, namely the maximum speed.

$$F_{drag}(t) = \frac{1}{2} \rho A_p C_D \|V(t)\|^2 \quad [\text{N}]. \quad (2.87)$$

Aerodynamic lift, on the other hand, is a force perpendicular to the velocity vector (approximately vertical), further "pushing" the vehicle against the road. It may also be referred to as downforce and is given by (2.88).

$$F_{lift}(t) = \frac{1}{2} \rho A_p C_L \|V(t)\|^2 \quad [\text{N}]. \quad (2.88)$$

Regarding equations (2.87) and (2.88),  $\rho$  is the air density,  $A_p$  is the vehicle projected/section area,  $C_D$  is the drag coefficient and  $C_L$  is the lift coefficient.

The prototypes built by FST Lisboa are typically designed to have the CP marginally ahead of the CG, along the longitudinal direction. If they do not coincide, the translation of forces  $F_{drag}$  and  $F_{lift}$  to the CG must also include moments. As a simplification, one assumes that they are coincident and no

moments due to aerodynamics are created.

After these considerations, it is possible to determine the vertical load transfer due to aerodynamics, as depicted in figure 2.14. Performing a balance of moments in point  $O$ , one concludes:

$$F_{drag}(t) L_h + F_{lift}(t) L_f = \Delta W_{rear}^{aero}(t)(L_f + L_r) \Leftrightarrow \Delta W_{rear}^{aero}(t) = \frac{F_{drag}(t) L_h + F_{lift}(t) L_f}{L_f + L_r} \text{ [N]}. \quad (2.89)$$

Once again, the mass transfer from the front axle is symmetrical,

$$\Delta W_{front}^{aero}(t) = -\Delta W_{rear}^{aero}(t) \text{ [N]}. \quad (2.90)$$

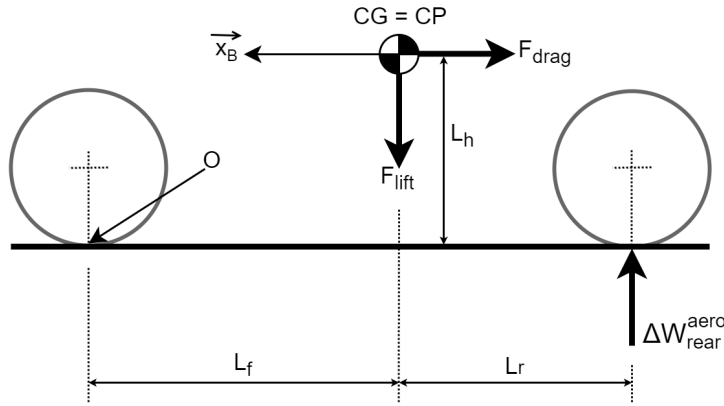


Figure 2.14: Weight transfer due to aerodynamic forces.

If one does not consider the effects of suspension systems, the total vertical load  $F_z(t) = F_z^{st} + F_z^{dyn}(t)$  can be approximated by:

$$F_{z_1}(t) = F_{z_1}^{st} + \frac{1}{2} \Delta W_{front}^{weight}(t) + \frac{1}{2} \Delta W_{left}^{weight}(t) + \frac{1}{2} \Delta W_{front}^{aero}(t) \text{ [N]}; \quad (2.91)$$

$$F_{z_2}(t) = F_{z_2}^{st} + \frac{1}{2} \Delta W_{front}^{weight}(t) + \frac{1}{2} \Delta W_{right}^{weight}(t) + \frac{1}{2} \Delta W_{front}^{aero}(t) \text{ [N]}; \quad (2.92)$$

$$F_{z_3}(t) = F_{z_3}^{st} + \frac{1}{2} \Delta W_{rear}^{weight}(t) + \frac{1}{2} \Delta W_{left}^{weight}(t) + \frac{1}{2} \Delta W_{rear}^{aero}(t) \text{ [N]}; \quad (2.93)$$

$$F_{z_4}(t) = F_{z_4}^{st} + \frac{1}{2} \Delta W_{rear}^{weight}(t) + \frac{1}{2} \Delta W_{right}^{weight}(t) + \frac{1}{2} \Delta W_{rear}^{aero}(t) \text{ [N]}. \quad (2.94)$$

The CG location in this modelling is considered fixed but, in practice, the CG height changes with longitudinal acceleration. To mitigate the consequences of these variations, anti-dive, anti-lift or anti-squat strategies can be employed when designing the suspension geometry [7].

## Chapter 3

# Traction control of a Formula Student prototype

In this chapter, the design of traction controllers is detailed, corresponding to the last layer of the planning and control pipeline. The low-level controllers are responsible for controlling the actuation of the physical system, in this case, the motor torques and the steering wheel angle.

Since the Formula Student prototype has four wheel-hub motors which can be individually controlled, the car has effectively five DOF for low-level actuation: four motor torques and the steering wheel angle. This allows for a significant design freedom but requires more complex low-level control algorithms [32], comparing with cars with fewer motors.

### 3.1 Autonomous driving simulator overview

Before focusing on the design of traction controllers, the perception, planning and control architecture of the driverless prototype from FST Lisboa must be explained, which is implemented in simulation according to the diagram from figure 3.1.

The first logical task of an autonomous vehicle is to interpret the surroundings, detecting the race track limits in this particular case, which is associated to the "Perception" module. A LIDAR and camera are employed, which feed neural networks and point-cloud processing algorithms. After obtaining the position of the plastic cones that define the track limits, the "High-level planning" module computes a trajectory that minimises the lap time, creating a desired path with an associated velocity profile that feeds the following module. To ensure that the desired trajectory is correctly tracked, the "Mid-level controllers" generate the references of longitudinal velocity, yaw rate and steering angle. Finally, the "Low-level controllers" must ensure that the mid-level references are followed, regulating the actuation effort - motor torques and steering wheel angle -, strongly influenced by the existing traction conditions, or the tire-road interaction. Ideally, all three layers should be co-designed to extract the maximum performance of the connected system, as suggested in [32]. However, to limit the scope of this work, only the low-level layer is considered. To validate the low-level controllers, the outputs of the high-level planning and mid-level

control modules are considered external. Vehicle perception is not yet implemented in the simulator - the simulator inputs are the race track limits. The "Simulation" and "Visualisation" blocks implement the realistic vehicle model described in section 2.1.

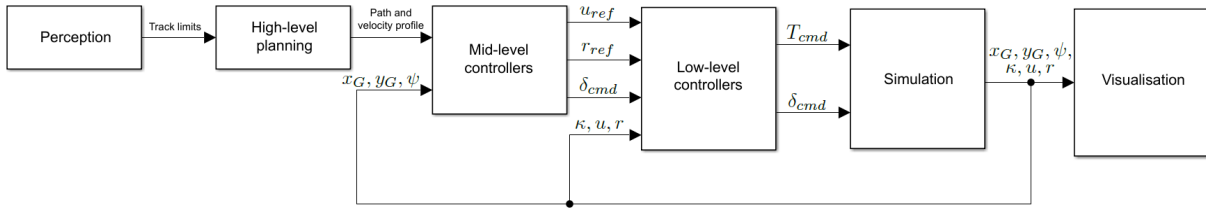


Figure 3.1: Diagram of the autonomous driving simulator for FST Lisboa.

### 3.2 Simplified vehicle model implementation

To develop a traction control architecture that is able to simultaneously influence longitudinal (accelerating and decelerating) and lateral (turning) dynamics, it is useful to analyse the vehicle model derived in section 2.2.3, particularly the consequences of the linearised model around an operating point:

- The longitudinal and lateral subsystems are decoupled, suggesting the employment of two independent controllers.
- The longitudinal dynamics is chained: the motor torque influences the tire slip ratio, which in turn influences the vehicle longitudinal speed. The slip ratio dynamics is several orders of magnitude faster than that of the longitudinal vehicle speed.
- The lateral vehicle speed and the yaw rate dynamics are coupled, with the latter being slower. The yawing torque due to torque vectoring directly affects the yaw rate dynamics.

These learnings justify the implementation of the longitudinal and lateral controllers, documented in sections 3.2.1 and 3.2.2, which can be summarised by the diagram from figure 3.2.

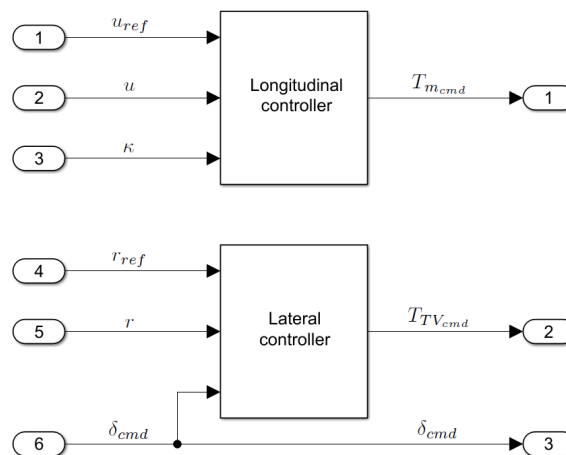


Figure 3.2: Block diagram of the simplified traction control scheme.

### 3.2.1 Longitudinal controller

A cascade control architecture for the longitudinal subsystem is suggested, allowing the control of both the slip ratio  $\kappa$  (inner loop) and the longitudinal speed  $u$  (outer loop), as shown in figure 3.3. This structure is appropriate for the longitudinal traction control problem due to the existing coupling of the slip ratio and the longitudinal speed dynamics and since the former is faster - they can be controlled in chain. This architecture also allows the controller to directly saturate the physical quantities that must be limited: the slip ratio  $\kappa$  must be limited due to tire performance constraints (3.1) and the motor torque command  $T_{m_{cmd}}$  is bounded by hardware limits (3.2):

$$\kappa(t) \in [\kappa_{min}, \kappa_{max}] \quad [-]; \quad (3.1)$$

$$T_{m_{cmd}}(t) \in [T_{m_{min}}, T_{m_{max}}] \quad [\text{N.m}]. \quad (3.2)$$

The controllers employed are proportional gains,  $K_u$  and  $K_\kappa$ , such that:

$$\kappa_{ref}(t) = K_u(u_{ref}(t) - u(t)) \quad [-]; \quad (3.3)$$

$$T_{m_{cmd}}(t) = K_\kappa(\kappa_{ref}(t) - \kappa(t)) \quad [\text{N.m}]. \quad (3.4)$$

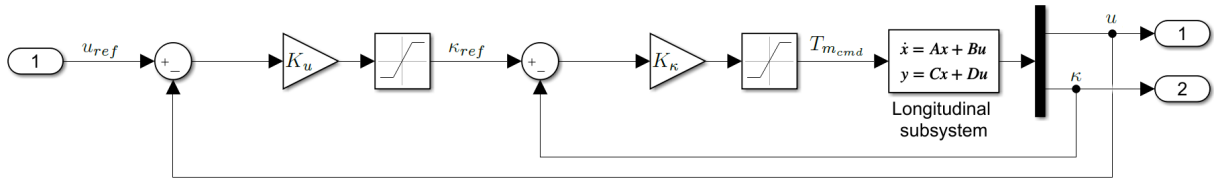


Figure 3.3: Controller implemented for the longitudinal subsystem.

### 3.2.2 Lateral controller

The use of independent wheel-hub motors allows for asymmetric torque distributions. A left/right motor torque asymmetry assists in controlling the slip ratios created in each tire while describing a turn. Additionally, if a left/right torque asymmetry exists, a yawing moment due to torque vectoring  $T_{TV_{cmd}}$  will be created, inducing a rotation of the car about the  $\vec{z}_B$  axis. In fact, the regulation of the yawing moment is crucial in a typical Formula Student race track with sharp and consecutive turns, in addition to the steering wheel input, allowing the car to rotate on its vertical axis and perform a turn with the highest possible yaw acceleration.

Since the yaw rate and lateral vehicle speed are coupled, and given that the regulation of the yawing torque  $T_z$  is important, the lateral controller is defined as a yaw rate tracker, as shown in figure 3.4. The controller creates an additional yawing moment command due to torque vectoring  $T_{TV_{cmd}}$ , given by

$$T_{TV_{cmd}}(t) = K_r(r_{ref}(t) - r(t)) \quad [\text{N.m}], \quad (3.5)$$

where  $K_r$  is a proportional gain. To observe physical and stability limits, the additional yawing moment

is bounded by

$$T_{TV_{cmd}}(t) \in [T_{TV_{min}}, T_{TV_{max}}] \text{ [N.m]}. \quad (3.6)$$

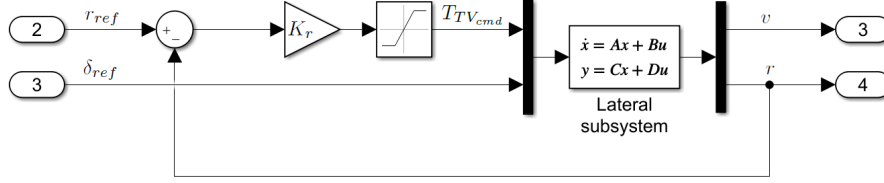


Figure 3.4: Controller implemented for the lateral subsystem.

### 3.3 Realistic vehicle model implementation

The bicycle model with slip dynamics is useful to better understand the requirements and controller architecture. However, being a single-track vehicle model, it is not sensitive to vertical load transfers, which strongly influence the tire deformations - slip ratio and slip angle. Additionally, the RWD simplification with one equivalent motor torque command  $T_{m_{cmd}}$  does not physically describe the evolution of  $T_z$  - which has contributions from the four existing motors. However, the merits of the proposed control architecture can be extended to the realistic tridimensional vehicle model presented in section 2.1.

Instead of tuning the controllers exclusively resorting to a simplified vehicle model, to fully capture the relevant tire slip dynamics, the controller fine tuning process is made using the realistic tridimensional simulator. Even though the tuning effort increases due to the higher levels of detail, the results are expected to be more reliable and directly applicable to the physical prototype. In terms of inputs, the simulator receives the motor torque commands  $T_{cmd_1}$ ,  $T_{cmd_2}$ ,  $T_{cmd_3}$  and  $T_{cmd_4}$  and the steering angle command  $\delta_{cmd}$ .

Figure 3.5 shows the proposed full complexity traction controllers, consisting of three modules: longitudinal controller, lateral controller and power distribution. Based on the yaw rate tracking error  $e_r = r_{ref} - r$ , the lateral controller provides a slip ratio asymmetry  $\kappa_{diff}$  to the longitudinal controller. This controller regulates both the individual tire slip ratios  $\kappa$  and the vehicle longitudinal speed  $u$  according to the longitudinal speed tracking error  $e_u = u_{ref} - u$ . After computing the appropriate torque commands for each motor  $T$ , that simultaneously tracks  $u_{ref}$  and  $r_{ref}$ , the power distribution module checks whether the commands satisfy the Formula Student regulations and powertrain constraints and appropriately allocates the available electrical power to the four motors, outputting the final commands  $T_{cmd}$ , consisting of  $T_{cmd_1}$ ,  $T_{cmd_2}$ ,  $T_{cmd_3}$  and  $T_{cmd_4}$  and  $\delta_{cmd}$  - which remains unchanged from the input value - that will enter the simulator.

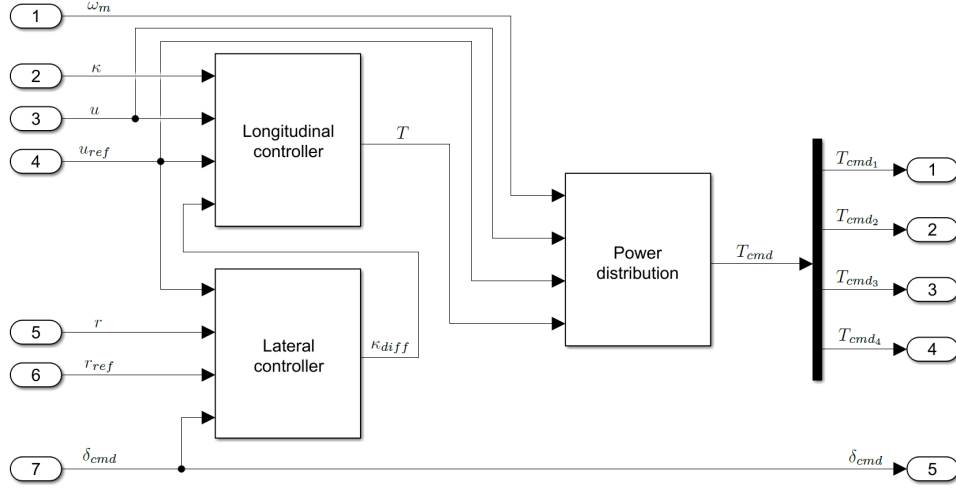


Figure 3.5: Block diagram of the full complexity traction control scheme.

### 3.3.1 Longitudinal controller

The use of the cascade control architecture with proportional gains is extended to control the vehicle longitudinal speed, the slip ratio of the four tires and receive information from the lateral controller, as shown in figure 3.6. The advantage of regulating the torque of each wheel is the possibility to limit the minimum and maximum values of both torque and slip ratio that are admissible for each tire.

Once again, the slip ratio reference  $\kappa_{ref}$  is determined as

$$\kappa_{ref}(t) = K_u(u_{ref}(t) - u(t)) \quad [-]. \quad (3.7)$$

Introducing the novel  $\kappa_{diff}$  component, the vector of motor torques  $T$  is now given by:

$$T_1(t) = K_{\kappa_f}(\kappa_{ref}(t) - \kappa_1(t) + \kappa_{diff}(t)) \quad [\text{N.m}]; \quad (3.8)$$

$$T_2(t) = K_{\kappa_f}(\kappa_{ref}(t) - \kappa_2(t) - \kappa_{diff}(t)) \quad [\text{N.m}]; \quad (3.9)$$

$$T_3(t) = K_{\kappa_r}(\kappa_{ref}(t) - \kappa_3(t) + \kappa_{diff}(t)) \quad [\text{N.m}]; \quad (3.10)$$

$$T_4(t) = K_{\kappa_r}(\kappa_{ref}(t) - \kappa_4(t) - \kappa_{diff}(t)) \quad [\text{N.m}]; \quad (3.11)$$

where  $K_{\kappa_f}$  and  $K_{\kappa_r}$  are the gains for the front and rear axles, respectively. The procedure to determine gains  $K_u$ ,  $K_{\kappa_f}$  and  $K_{\kappa_r}$  is explained in the next chapter.

The physical quantities that must be limited are, in this case:

$$\kappa_i(t) \in [\kappa_{min}, \kappa_{max}], i = 1, \dots, 4 \quad [-]; \quad (3.12)$$

$$T_1(t), T_2(t) \in [T_{fmin}, T_{fmax}] \quad [\text{N.m}]; \quad (3.13)$$

$$T_3(t), T_4(t) \in [T_{rmin}, T_{rmax}] \quad [\text{N.m}]; \quad (3.14)$$

allowing different motor torque saturations from front to rear axles.



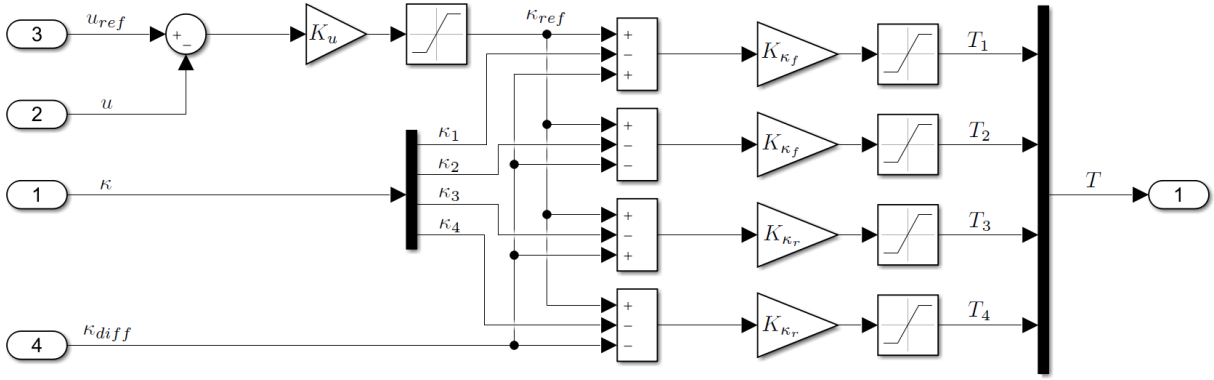


Figure 3.6: Block diagram of the longitudinal controller.

### 3.3.2 Lateral controller

The goals for the lateral controller, shown in figure 3.7, are to keep the slip ratio of the four tires within an acceptable range in a turn, while assisting the rotation of the vehicle about its vertical axis.

The simplified single-track vehicle model from section 2.2.3 cannot physically explain the creation of an additional yawing moment  $T_{TV}$ , since it is influenced by the four existing motors and only one motor is considered in the model. For the realistic vehicle model, the lateral controller output is no longer directly  $T_{TV}$ , but rather a slip ratio difference  $\kappa_{diff}$  given by (3.15), or asymmetry from left to the right car sides, that will improve the yaw response.

$$\kappa_{diff}(t) = K_r(r_{ref}(t) - r(t)) \quad [-], \quad (3.15)$$

which must respect the condition

$$\kappa_{diff}(t) \in [\kappa_{diff_{min}}, \kappa_{diff_{max}}] \quad [-]. \quad (3.16)$$

The procedure to determine gain  $K_r$  is explained in the next chapter.

If a yaw rate reference  $r_{ref}$  is not provided by the mid-level control layer, it is generated by the traction controllers according to (3.17), which is simultaneously influenced by the longitudinal velocity reference  $u_{ref}$  and the steering angle command  $\delta_{cmd}$ :

$$r_{ref}(t) = \frac{u_{ref}(t) \delta_{cmd}(t)}{(L_f + L_r) SR} \quad [\text{rad/s}], \quad (3.17)$$

where  $L_f + L_r$  represents the vehicle wheelbase and  $SR$  the steering ratio.

To correctly track the yaw rate reference  $r_{ref}$ , the slip ratio difference  $\kappa_{diff}$  is fed to the longitudinal controller, which computes the motor torques  $T$  that simultaneously ensure the tracking of  $u_{ref}$  and  $r_{ref}$ . Since  $\kappa_{ref}$  (3.7) and  $\kappa_{diff}$  (3.15) are both non-dimensional and contribute to the generation of the motor torque references, the relative magnitude of gains  $K_u$  and  $K_r$  effectively determines which reference is preferentially followed:

- If  $K_u \gg K_r$ ,  $u_{ref}$  will be preferentially followed;

- If  $K_r \gg K_u$ ,  $r_{ref}$  will be preferentially followed.

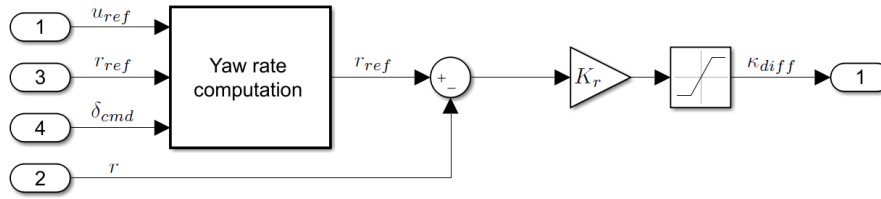


Figure 3.7: Block diagram of the lateral controller.

### 3.3.3 Power distribution

As mentioned in section 2.1.3, the electrical power that the vehicle uses is limited by the Formula Student competition regulations, which means that it must be monitored online and kept within an acceptable range if the vehicle has a 4WD configuration - for a RWD configuration, power control is not strictly necessary since the vehicle naturally complies with the regulations. In practice, this is enforced by measuring the voltage and current flowing from the battery and respecting the condition (2.35). Since the electrical component of the powertrain is not accurately modelled in this thesis, the condition cannot be directly enforced, so an alternative for power measurement is required.

If no electrical or mechanical losses between the battery and the driven wheel  $i$  are considered, all the electrical power is converted into mechanical power,

$$P_{total}(t) = \sum_i T_{cmd_i}(t) \omega_{m_i}(t) \text{ [W]}. \quad (3.18)$$

Knowing the motor angular speeds  $\omega_{m_i}$  and controlling the motor torques  $T_{ref_i}$ , it is possible to ensure that

$$P_{min} \leq P_{total}(t) \leq P_{max} \text{ [W]}, \quad (3.19)$$

where  $P_{min}$  corresponds to the electrical power limit when the PMSM is working in generator mode - limited mostly by the battery cells charging speed - and  $P_{max}$  the electrical power limit in motor mode - limited by the competition regulations.

The power distribution module receives as inputs:

- The motor angular velocities  $\omega_m$
- The output from the longitudinal controller  $T$ ;
- The longitudinal velocity reference  $u_{ref}$  and the current value  $u$ ;
- The motor torque saturations  $T_{f_{min}}$ ,  $T_{f_{max}}$ ,  $T_{r_{min}}$  and  $T_{r_{max}}$ ;
- The maximum and minimum motor speeds  $\omega_{m_{max}}$  and  $\omega_{m_{min}}$ ;
- The maximum and minimum electrical power limits  $P_{max}$  and  $P_{min}$ ;

and outputs two vectors that define the upper and lower PMSM torque limits,  $T_{up}$  and  $T_{low}$ , which are fed to a dynamic saturation block. The saturation block dynamically limits  $T$ , creating the final motor torque

command  $T_{cmd}$ , that fulfils the electrical power constraints, as depicted in figure 3.5. The electrical power distribution methodology is presented in algorithm 1.

---

**Algorithm 1: Power distribution**

---

**Input:**  $\omega_m, T, u, u_{ref}, T_{fmin}, T_{fmax}, T_{rmin}, T_{rmax}, \omega_{mmax}, \omega_{mmin}, P_{max}, P_{min}$   
**Output:**  $T_{up}, T_{low}$

```

1 while  $u_{ref} > 0$  do
2    $\omega_{mmean} = \text{mean}(\omega_m)$  // Compute the average motor speed
3   if  $\omega_{mmean} \geq \omega_{mmax}$  then
4      $T_{up} = (0 \ 0 \ 0 \ 0)^T$  // Only coasting or decelerating are possible
5      $T_{low} = (T_{fmin} \ T_{fmin} \ T_{rmin} \ T_{rmin})^T$ 
6   else if  $\omega_{mmean} \leq \omega_{mmin}$  then
7      $T_{up} = (T_{fmax} \ T_{fmax} \ T_{rmax} \ T_{rmax})^T$  // Only accelerating or coasting are possible
8      $T_{low} = (0 \ 0 \ 0 \ 0)^T$ 
9   else
10     $\omega_{limacc} = \frac{P_{max}}{2T_{fmax} + 2T_{rmax}}$  // Compute the motor speeds from/below which power limi-
11     $\omega_{limdec} = \frac{-P_{min}}{2|T_{fmin}| + 2|T_{rmin}|}$  // tation is necessary, in acceleration and deceleration
12    if  $u_{ref} \geq u$  then // In acceleration
13      if  $\omega_{mmean} \geq \omega_{limacc}$  then
14         $T_{up} = \frac{P_{max}}{\omega_{mmean}} \left( \frac{1}{4} \ \frac{1}{4} \ \frac{1}{4} \ \frac{1}{4} \right)^T$ 
15         $T_{low} = (T_{fmin} \ T_{fmin} \ T_{rmin} \ T_{rmin})^T$ 
16      else
17         $T_{up} = (T_{fmax} \ T_{fmax} \ T_{rmax} \ T_{rmax})^T$ 
18         $T_{low} = (T_{fmin} \ T_{fmin} \ T_{rmin} \ T_{rmin})^T$ 
19      else // In deceleration
20        if  $\omega_{mmean} \geq \omega_{limdec}$  then
21           $T_{up} = (T_{fmax} \ T_{fmax} \ T_{rmax} \ T_{rmax})^T$ 
22           $T_{low} = \frac{P_{min}}{\omega_{mmean}} \left( \frac{3}{10} \ \frac{3}{10} \ \frac{2}{10} \ \frac{2}{10} \right)^T$ 
23        else
24           $T_{up} = (T_{fmax} \ T_{fmax} \ T_{rmax} \ T_{rmax})^T$ 
25           $T_{low} = (T_{fmin} \ T_{fmin} \ T_{rmin} \ T_{rmin})^T$ 

```

---

The choice of weights for  $T_{up}$  if  $\omega_{mmean} \geq \omega_{limacc}$  corresponds to requesting the same power from all four motors, or  $\frac{P_{max}}{4}$  for each one. The choice is based on the fact that generally, when the power limit in acceleration is reached, traction is no longer a limiting factor, since the vehicle is close to a steady-state in terms of vertical load and tire slip. Additionally, since it is expected that  $P_{max}$  is reached at the end of a long straight line, unloading the rear motors is crucial, since they should be closer to the thermal limit than the front ones, which makes the built-in controller derate the motor torque. By shifting a fraction of the available power to the front motors in these instances, the derates can be postponed or even avoided. This assumption is valid considering that most power comes from the rear motors before  $P_{max}$  is reached, due to traction constraints.

The choice of weights for  $T_{low}$  if  $\omega_{mmean} \geq \omega_{limdec}$  has a different reasoning, mainly because vertical

load is transferred to the front axle while decelerating, increasing its potential of transmitting longitudinal force via the more loaded tires. The bias towards the front axle aims to avoid rear wheel lock, which can originate an unforeseen and unstable vehicle behaviour. Front wheel lock should also be avoided but is more tolerable from a stability perspective, since it induces a predictable behaviour, with the tires simply skidding.

Additionally,  $u_{ref}$  should be consistent with the motor speed operating range. By default,  $\omega_{m_{min}} = 0$  [rad/s] and  $\omega_{m_{max}} = 2094.4$  [rad/s] (20000 [rpm]), which correspond to the physical hardware limits. Converting motor angular speeds into vehicle linear speed, one concludes:

$$0 < u_{ref}(t) < \frac{2094.4 R}{GR} = 29.4 \text{ [m/s]}, \quad (3.20)$$

considering  $GR = 16.25$  [-] and  $R = 0.228$  [m]. If  $u_{ref} \geq 29.4$  [m/s], the null torque zone is reached, as shown in figure 2.7, and that causes torque chattering between  $T_{up} = (0 \ 0 \ 0 \ 0)^T$  [N.m] and  $T_{low} = (T_{f_{min}} \ T_{f_{min}} \ T_{r_{min}} \ T_{r_{min}})^T$  [N.m], which should be avoided to preserve the hardware. Analogously, if  $u_{ref} \approx 0$  [m/s], a highly inefficient motor operating region is entered, making the motors unsuitable to fully stop the vehicle.

## Chapter 4

# Controllers tuning and validation

In this chapter, a review of the Formula Student Driverless regulations is made, which motivate the controllers tuning process. The performance requirements for representative driving instances are defined and, finally, some insights about the realistic simulator are given.

### 4.1 Formula Student Driverless regulations

There are several dynamic events in a Formula Student competition, with slightly different rules for the person-driven and driverless categories but essentially with common goals. Considering the driverless category regulations, the dynamic events are:

- Acceleration - assesses the vehicle's longitudinal acceleration over a seventy five metres straight, followed by a braking zone, as shown in figure 4.1;
- Skid Pad - assesses the vehicle's lateral acceleration, driving over a figure-of-eight track at constant speed, depicted in figure 4.2;
- Autocross - consisting of a five hundred metres lap over a track with straights, turns and chicanes, assesses peak driving performance;
- Trackdrive - assesses durability and reliability of the vehicle over ten laps of the Autocross track, as in figure 4.3;
- Efficiency - the energy consumption relative to vehicle speed is assessed for the entire Trackdrive event.

To cover a wide range of driving conditions, the traction controllers are assessed in three categories: purely longitudinal, purely lateral and combined. For each category, a performance index  $J_P$  is suggested, to evaluate the aspects that are assumed to be more relevant in that category.

A heuristic tuning procedure for the traction controllers is suggested in the following sections. Due to the high number of design parameters and the heuristic nature of the procedure, it does not guarantee the determination of an optimal solution, but should steer the trial-and-error process in the correct

direction. Further parameter tuning can be performed on-track, starting from the proposed solution this thesis suggests.

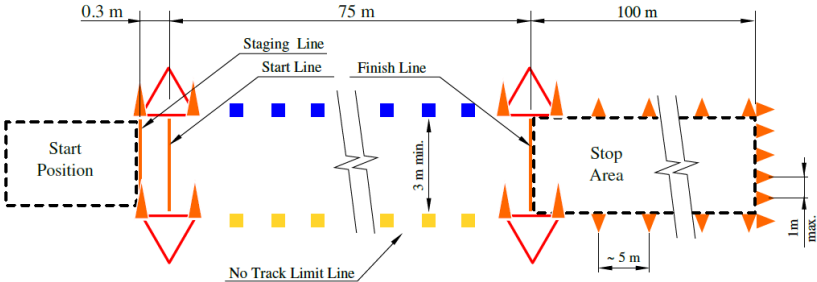


Figure 4.1: Layout of the Acceleration event [5].

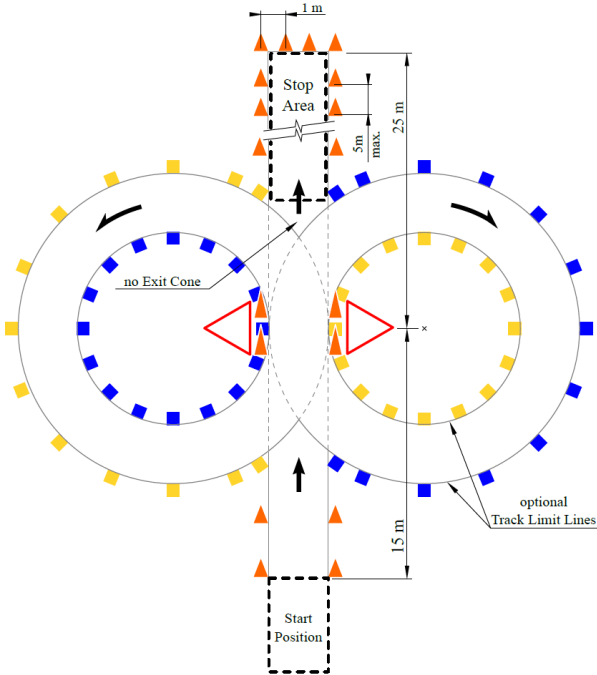


Figure 4.2: Layout of the Skid Pad event [5].

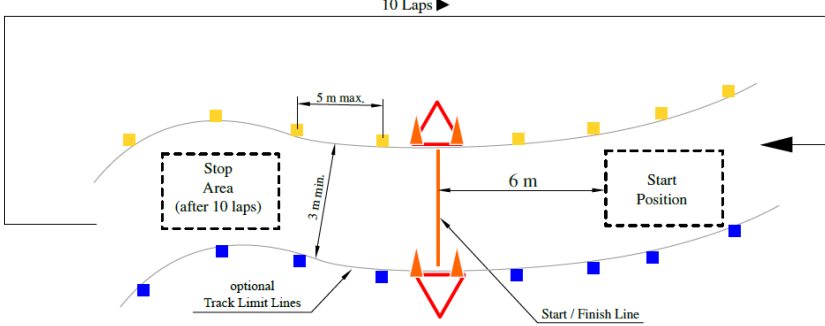


Figure 4.3: Layout of the Trackdrive event [5].

The race track limits are defined by plastic cones of four types, as shown in figure 4.4. The driverless vehicles must be able to perceive them and navigate the vehicle along the race track.



Figure 4.4: Types of cones used to define the race tracks [5].

## 4.2 Longitudinal performance

Pure longitudinal performance is heavily influenced by the longitudinal controller and power distribution modules, introduced in sections 3.3.1 and 3.3.3, which have the following design parameters:

- Gains  $K_u$ ,  $K_{\kappa_f}$  and  $K_{\kappa_r}$ ;
- Slip ratio saturations  $\kappa_{max}$  and  $\kappa_{min}$ ;
- Motor torque saturations  $T_{f_{min}}$ ,  $T_{f_{max}}$ ,  $T_{r_{min}}$  and  $T_{r_{max}}$ ;
- Electrical power limits  $P_{max}$  and  $P_{min}$ ;

essentially corresponding to eleven degrees of freedom, which prevent a straightforward approach to tuning. To achieve a design parameter combination that improves longitudinal performance, the following steps are followed:

1. Determine the desired range of tire slip by defining  $\kappa_{max}$  (tire slip in acceleration) and  $\kappa_{min}$  (tire slip in deceleration).
2. Determine the desired range of electrical power  $P_{max}$  (PMSM in motor mode) and  $P_{min}$  (PMSM in generator mode).
3. Tune gains  $K_u$ ,  $K_{\kappa_f}$  and  $K_{\kappa_r}$  for a scenario in which motor torque saturations do not play an important role, since the upper and lower bounds of  $P_{max}$  and  $P_{min}$  are not reached, and traction is the limiting factor for performance. The selected instance is a step in longitudinal speed from 0 to 10 [m/s]. For this input, the controlled system requirements (outer loop of the cascade) are presented in table 4.1.

Table 4.1: Performance requirements for  $u_{ref} = 10$  m/s.

Metric	Value, [units]
Settling time	< 2.5 [s]
Overshoot	< 5 [%]
Steady-state error	< 5 [%]

These requirements cover the typical dynamic goals for a Formula Student prototype - responding fast, accurately, with a non-oscillatory behaviour to a command (of longitudinal speed, in this case).

To try and isolate the effects of a cascade architecture, a known and constant slip ratio reference  $\kappa_{ref}$  is considered to determine  $K_{\kappa_f}$  and  $K_{\kappa_r}$ . The requirements for the inner loop are less strict than for the outer one: the only conditions are that the resulting motor torque reference is continuous and smooth, being consistent with the sign of  $\kappa_{ref}$ .

After defining  $K_{\kappa_f}$  and  $K_{\kappa_r}$ , gain  $K_u$  is tuned to achieve the requirements for the controlled system, stated in table 4.1.

4. Tune the motor torque saturations  $T_{f_{min}}$ ,  $T_{f_{max}}$ ,  $T_{r_{min}}$  and  $T_{r_{max}}$  for a scenario in which motor torque saturations strongly influence performance. The most relevant instance is necessarily the Acceleration event, depicted in figure 4.1.

For the Acceleration event, the longitudinal speed reference  $u_{ref}$  is defined as a step with the size of the vehicle's maximum speed, followed by a command to stop after the 75 [m] of the timed run have elapsed, as shown in figure 4.5.

Recovering equation (3.20), the reference for the Acceleration event is given by:

$$u_{ref}(t) = \begin{cases} 29 \text{ [m/s]}, & x_G < 75 \text{ [m]} \\ 0.5 \text{ [m/s]}, & x_G \geq 75 \text{ [m]} \end{cases}$$

to asymptotically come close to  $\omega_{m_{max}}$  but not reach it and, likewise, come close to  $\omega_{m_{min}}$  but not reach it.

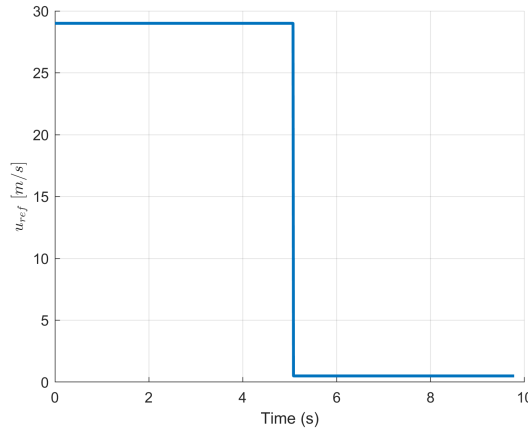


Figure 4.5: Longitudinal speed reference for the Acceleration event.

The way the speed reference is generated implies:

- The first branch of the speed reference is very close to the vehicle's maximum one, which means that the actuation effort should be maximum - necessary to achieve the best possible lap time;
- The second branch of the speed reference is very close to a stopped vehicle, by which point the motors should switch off or the hydraulic braking system should be engaged - since the motors are extremely inefficient at low speeds and are not suited to fully stop the vehicle up to  $u = 0$  [m/s];
- Irrespective on how fast the vehicle completes the Acceleration event, it will be commanded to stop, or  $u_{ref} = 0.5$  [m/s], after it reaches the end of the 75 [m] timed run;
- The performance of the traction controllers can be ranked according to the time it takes for the speed reference to switch to zero, termed  $t_{run}$ .



Then, for the Acceleration event, the suggested performance index is simply given by

$$J_P = t_{run} \text{ [s]}. \quad (4.1)$$

5. Assess the proposed solution in terms of robustness to changing or uncertain driving parameters.

The considered parameters are:

- Friction coefficient  $\mu$ , tested for  $\pm 50$  [%] of the design value, with 10 [%] increments;
- Vehicle mass  $m$ , tested for  $\pm 30$  [%] of the design value, with 5 [%] increments;
- Tire radius  $R$ , tested for  $\pm 10$  [%] of the design value, with 2.5 [%] increments.

### 4.3 Lateral performance

Pure lateral performance can be assessed in a steady-state cornering manoeuvre such as the Skid Pad event, or as a transient manoeuvre such as a chicane/slalom. To isolate the component of lateral dynamics as much as possible, the tests are performed at constant longitudinal speed  $u$ .

Tuning the lateral controller is a simpler task than tuning the longitudinal one, since there are fewer parameters:  $K_r$ ,  $\kappa_{diff_{max}}$  and  $\kappa_{diff_{min}}$ . Due to the coupling between longitudinal and lateral dynamics (a car cannot turn if it is not moving forward), the lateral controller tuning should be performed after the longitudinal controller is set, with a solution that fulfils longitudinal performance requirements.

The procedure to tune the lateral controller is the following:

1. Define gain  $K_u$  so that the subsequent tests are performed at a prescribed, constant  $u$  - even while turning and consequently dissipating energy - and gains  $K_{\kappa_f}$  and  $K_{\kappa_r}$  so that the resulting motor torque reference stays within an admissible range. Determine the appropriate motor torque saturations to investigate lateral dynamics.
2. Determine the desired slip ratio differences  $\kappa_{diff_{max}}$  and  $\kappa_{diff_{min}}$ , which should be equal in absolute value provided there is no preferential turning side.
3. Tune gain  $K_r$  based on two representative instances of lateral dynamics: a step input in yaw rate  $r_{ref} = 1$  [rad/s] and a chicane - a typical manoeuvre in racing - both performed at constant  $u$ . The lateral performance requirements are the following:

- Regarding the unitary yaw rate step input, the quantitative requirements for the controlled system are defined in table 4.2. The rise time requirement captures the speed of the transient response, while the steady-state error one ensures adequate tracking of a constant yaw rate reference.

The significance of this step input corresponds to performing half of a Skid Pad event, sketched in figure 4.2.

- To take into consideration more complex instances of lateral dynamics, such as handling at the limit of tire adhesion, a chicane is considered. A chicane is characterised as having con-

Table 4.2: Performance requirements for  $r_{ref} = 1$  rad/s.

Metric	Value, [units]
Rise time	< 0.4 [s]
Steady-state error	< 1 [%]

secutive turns to opposite sides, similarly to avoid an unforeseen road obstacle, which occurs frequently in a Formula Student track. A yaw rate reference that represents this situation is shown in figure 4.6. The suggested command corresponds to the worst-case scenario in terms of yaw rate reference, since it is very abrupt and discontinuous, testing the controller's robustness. In a practical application, one expects a smoother reference and, consequently, an overall smoother vehicle behaviour.

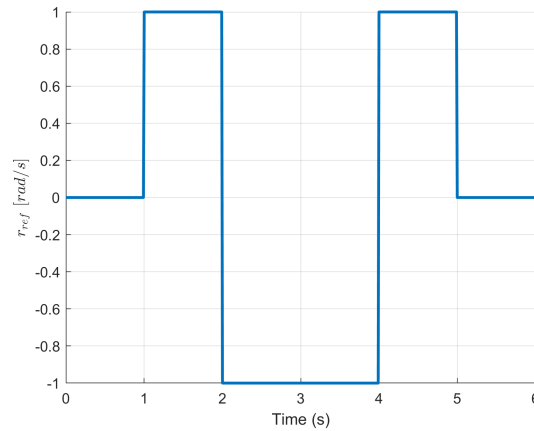


Figure 4.6: Yaw rate reference for a chicane.

In a chicane, considering that it will impact subsequent manoeuvres when navigating the race track, performance can be ranked based on how well the controllers can follow the reference. The proposed performance index is given by the root-mean-square (RMS) yaw rate reference tracking error:

$$J_P = \text{RMS}(r_{ref} - r) \text{ [rad/s]}. \quad (4.2)$$

- In typical low-radius Formula Student turns, it is often observed that inner tires (right tires in a right-hand turn and vice-versa for a left-hand one) break traction and start spinning, creating a spike in the slip ratios of those tires. This happens because that vehicle side is vertically unloaded and the same torque command is given from left to right motors. So, an additional, qualitative lateral controller requirement is that the slip ratios of the inner tires are inferior to that of the outer ones, particularly during the transient part of the response. This corresponds to implementing a torque vectoring capability.

It is expected that all performance metrics improve with an increase in  $K_r$ . However, as explained in section 3.3.2, the relative magnitude of gains  $K_u$  and  $K_r$  is important to adequately follow simultaneously  $u_{ref}$  and  $r_{ref}$ . Additionally, high values of  $K_r$  will saturate the actuators and reduce

stability for lower-traction conditions. For these reasons, the lowest value of  $K_r$  that fulfills all performance requirements must be chosen.

4. Assess the proposed solution in terms of robustness to changing friction coefficient  $\mu$ , tested for  $\pm 50$  [%] of the design value, with 10 [%] increments.

## 4.4 Combined performance

Representing a traditional approach to racing, the high-level goal is to minimize the lap time around a generic race track. From a lower-level, traction control perspective, the goal in driving around a generic race track is still to follow the speed references  $u_{ref}$  and  $r_{ref}$ , while respecting powertrain and tire state constraints.

In the Formula Student Driverless competition, the most complex dynamic event is the Trackdrive, as sketched in figure 4.3. FST Lisboa provided two race tracks for simulation, which were the Trackdrive courses from previous competitions held in Germany and Italy, shown in figures 4.7(a) and 4.7(b), respectively. Instead of simulating ten consecutive laps around the race track, only the first lap is considered, since it is more demanding in terms of traction control due to the stand-still start. It is expected that, if the first lap is completed without driving off-track, the remaining nine should be quite similar, since the trajectory is not updated online, provided there is no drastic change in traction conditions. If the design parameters of the traction controllers were well defined by the procedures for longitudinal and lateral performance (independent tuning for both instances), little or no additional tuning effort should be necessary when both instances are combined, in a way, for a generic race track.

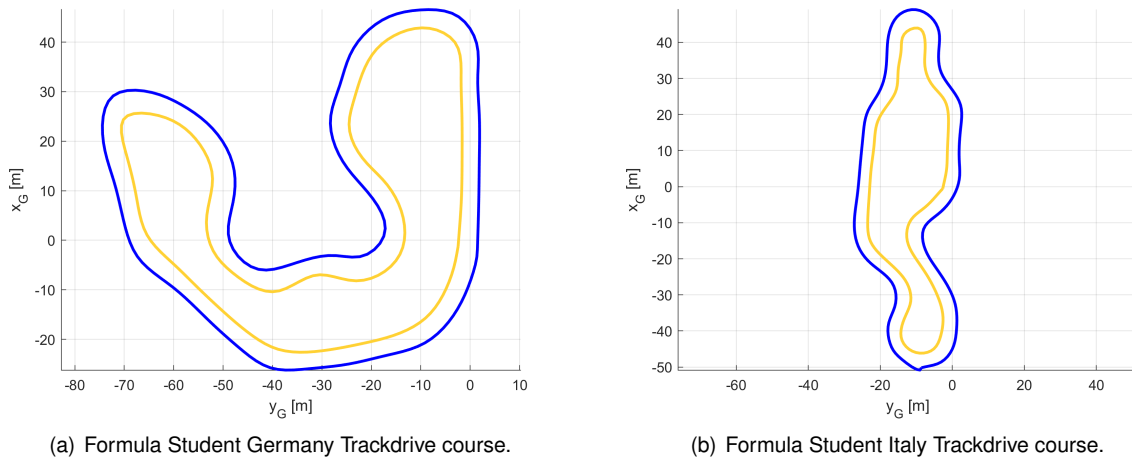


Figure 4.7: Race tracks used for simulation.

The suggested procedure to validate the traction controllers on the generic race tracks is the following:

1. Create sets of trajectories that correspond to increasing levels of traction, based on [18]. Three trajectory categories are considered: poor traction (adequate for low  $\mu$  values), intermediated traction (adequate for intermediate  $\mu$  values) and excellent traction (adequate for high  $\mu$  values).

2. Validate the resulting trajectories for varying  $\mu$ ,  $\pm 50$  [%] of the design value, with 10 [%] increments.
3. Compute the performance indexes associated to the traction controllers,  $J_{P_u}$  and  $J_{P_r}$ , defined as

$$J_{P_u} = \text{RMS}(u_{ref} - u) \text{ [m/s];} \quad (4.3)$$

$$J_{P_r} = \text{RMS}(r_{ref} - r) \text{ [rad/s];} \quad (4.4)$$

and  $t_{lap}$  [s], the time it takes to finish the lap. It is expected that  $t_{lap}$  is strongly influenced by the trajectory definition and not so much by the performance of the traction controllers.

The metrics only make physical sense if the vehicle does not drive off-track, keeping within the blue and yellow cones. If the vehicle drives off-track irreversibly, the run is classified as DNF (did not finish), scoring zero points in that particular run.

4. Investigate whether all tire state and powertrain constraints are fulfilled for the entire range of  $\mu$ .

## 4.5 Simulation specifics

This thesis focuses on the "Low-level controllers" block, which is downstream from the "High-level planning" and "Mid-level controllers" blocks, as shown in the diagram from figure 3.1. The planning tasks are performed offline, so no variables are fed back. On the other hand, the mid-level controllers receive the vehicle planar pose, position  $(x_G, y_G)$  [m] and orientation  $\psi$  [rad], as feedback. Finally, to the low-level controllers are fed back the longitudinal speed  $u$ , yaw rate  $r$  and the slip ratios of the four tires  $\kappa$ . In a practical application, none of these variables would be readily available for feedback, so an online estimator must be implemented, fusing information from the existing sensors - motor encoders, GPS, accelerometer, camera and LIDAR - and computing the most likely estimates. This thesis does not cover state estimation nor sensor modelling, so one assumes that all variables of interest are available for feedback.

The initial conditions considered in the simulator for the vehicle stand still configuration are shown in table 4.3. The initial value for the longitudinal speed  $u = 0.1$  [m/s] was chosen so that the singular configuration (in terms of software) for  $u = 0$  [m/s] is avoided, which means that the stand still configuration is actually defined with a marginal longitudinal speed. In practice, this compromise is acceptable, since the foremost part of the vehicle is staged 0.3 [m] behind the starting line [5]. Defining an initial slip ratio of  $\kappa_i = 0.001$  [-], the values for  $\omega_i$  may be computed according to equation (2.15). Similarly, the end of a simulation is defined when  $u < 0.5$  [m/s]. This condition is necessary since braking is only performed by the electric motors, which are not capable of fully stopping the vehicle due to the low efficiency at very low speeds. In practice, as long as the road is levelled, the car will come to a halt due to the internal drivetrain friction. The hydraulic braking system is usually a ON-OFF system, prohibiting any brake modulation, used to brake the car in emergency situations or after the run is completed.

Table 4.3: Stand still initial conditions in the simulation environment.

State/input variable	Value, [units]
$(u, v, w)$	$(0.1, 0, 0)$ [m/s]
$(p, q, r)$	$(0, 0, 0)$ [rad]
$(x_G, y_G, z_G)$	$(0, 0, -0.265)$ [m]
$(\varphi, \theta, \psi)$	$(0, 0, 0)$ [rad]
$(\omega_1, \omega_2, \omega_3, \omega_4)$	$(0.44, 0.44, 0.44, 0.44)$ [rad/s]
$(T_1, T_2, T_3, T_4)$	$(0, 0, 0, 0)$ [N.m]
$\delta$	0 [rad]

The constants and coefficients used to simulate the FST 10d race car were kindly provided by FST Lisboa and can be found in table 4.4.

Table 4.4: Constants and coefficients that model the FST 10d.

Category	Parameter	Symbol	Value, [units]
Aerodynamics	Air density	$\rho$	1.20 [kg/m <sup>3</sup> ]
Aerodynamics	CG downforce coefficient	$C_a$	1.96 [kg/m]
Aerodynamics	Drag coefficient	$C_D$	1.27 [-]
Aerodynamics	Lift coefficient	$C_L$	3.11 [-]
Aerodynamics	Projected area	$A_p$	1.05 [m <sup>2</sup> ]
Dissipation	CG translation coefficient	$C_t$	0.80 [kg/m]
Dissipation	CG rotation coefficient	$C_r$	0.001 [kg/s <sup>2</sup> ]
Dissipation	Wheels rotation coefficient	$C_{r_w}$	0.003 [kg/s <sup>2</sup> ]
Geometry	Distance from CG to front axle	$L_f$	0.816 [m]
Geometry	Distance from CG to rear axle	$L_r$	0.724 [m]
Geometry	Track width	$L_t$	1.200 [m]
Geometry	CG height	$L_h$	0.265 [m]
Powertrain	Powertrain efficiency	$\eta_{PT}$	0.90 [-]
Powertrain	Torque time constant	$t_{PT}$	0.02 [s]
Powertrain	Maximum motor torque	$T_{max}$	21 [N.m]
Powertrain	Maximum motor speed	$N_{max}$	20000 [rpm]
Powertrain	Gear ratio	$GR$	16.25 [-]
Steering	Maximum steering wheel angle	$\delta_{max}$	$\pm 28$ [deg]
Steering	Steering ratio	$SR$	6 [-]
Steering	Steering time constant	$t_{STA}$	0.1 [s]
Suspension	Mass (without driver)	$m$	256 [kg]
Suspension	Motion ratio of quarter $i$	$MR_i$	[1.11 1.11 1.14 1.14] [-]
Suspension	Elastic constant of spring $i$	$k_i$	[52.5 52.5 52.5 52.5] [kN/m]
Suspension	Damping constant of damper $i$	$c_i$	[2 2 2 2] [kN.s/m]
Suspension	Wheel inertia	$J_w$	0.24 [kg.m <sup>2</sup> ]
Suspension	Inertia tensor (CG)	$J$	$diag([39 142 160])$ [kg.m <sup>2</sup> ]
Tires	Loaded radius	$R$	0.228 [m]
Tires	Pressure	$p$	0.8 [bar]

# Chapter 5

## Results and discussion

In this chapter, the simulation results are presented and discussed. The performance of a baseline control solution that does not include traction considerations is presented and the inherent drawbacks are identified. To improve longitudinal and lateral performance, the procedure suggested in chapter 4 is followed, considering relevant instances of longitudinal and lateral performance, separately. Subsequently, the resulting solution is validated against more generic and complex instances, namely two FSD race tracks.

### 5.1 Solution without traction control

In this section, the relevance of a traction control scheme for a Formula Student prototype is studied, establishing a baseline solution that the traction controllers must improve on. Longitudinal dynamics is investigated with respect to an Acceleration event, while lateral dynamics considers a chicane. In both cases, no traction control is employed.

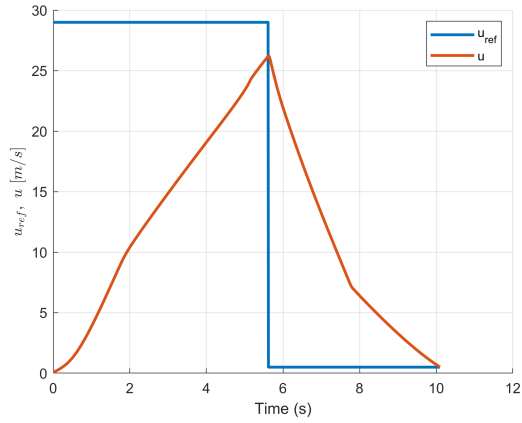
#### 5.1.1 Longitudinal dynamics

A simulation of the Acceleration event without traction control is performed. Since no traction considerations are implemented, the only goal is  $u_{ref}$  tracking, with a  $T_{cmd}$  proportional to the tracking error. Since the electrical power limits are typically reached in an Acceleration event, the power distribution module is not employed as well, since it might influence (improve) vehicle traction. To make the simulation numerically possible, the maximum allowable motor torque is not the hardware limit, but rather the much more feasible nominal value - approximately half of the hardware limit.

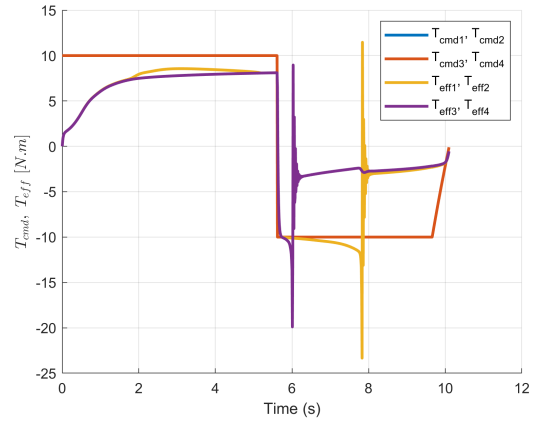
Moving on to the results for the Acceleration event, it is successfully completed, with  $J_P = 5.63$  [s], the time in which the switch to  $u_{ref} = 0.5$  [m/s] occurs, as shown in figure 5.1(a). However, not considering tire state introduces serious limitations to this approach, even if the maximum allowable motor torque is approximately half of the maximum possible value, as seen on figure 5.1(b). It is possible to observe, from figure 5.1(c), that the front tires are effectively spinning throughout the majority of the accelerating phase and skidding during part of the decelerating one, corresponding to  $|\kappa_i| \gg \kappa_{critical}$ ,  $i = 1, 2$ .

Regarding the rear tires, the problematic part is the full decelerating phase, in which tire skid ensues, or  $\kappa_i \ll -\kappa_{critical}$ ,  $i = 3, 4$ . In practice, these phenomena would induce an unstable car state, rendering control a very difficult task, especially for a driverless vehicle. Any small steering wheel correction could induce a spin around the vehicle's vertical axis, particularly during the decelerating phase. As it can be seen on figure 5.1(d), the longitudinal tire force  $F_x$  evolution has an unpredictable evolution, associated with the loss of traction and stability from a tire point of view. Even with conservative maximum motor torque values, the electric power requirements are not observed, as shown in figure 5.1(e). The G-G diagram from figure 5.1(f) shows relatively high maximum values, approximately  $a_{x_{max}} = 0.7$  [g] in acceleration and  $a_{x_{min}} = -1$  [g] in deceleration, however there is a high amount of points close to the origin - showing relatively low accelerations in a large portion of the Acceleration event - which must be improved.

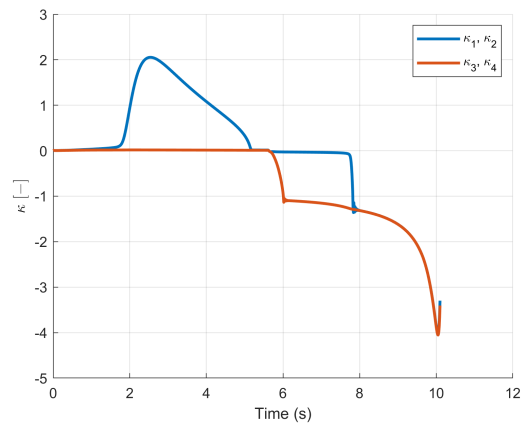
The results for an Acceleration event without traction control suggest that this approach is essentially flawed for a Formula Student prototype. Without TC, only very conservative motor torque saturations will avoid excessive tire spin and eventually tire lock. There is clearly an excess of power that cannot be adequately delivered to drive the vehicle, thus resulting in a deterioration in  $J_P$ , vehicle safety and the longevity of its components.



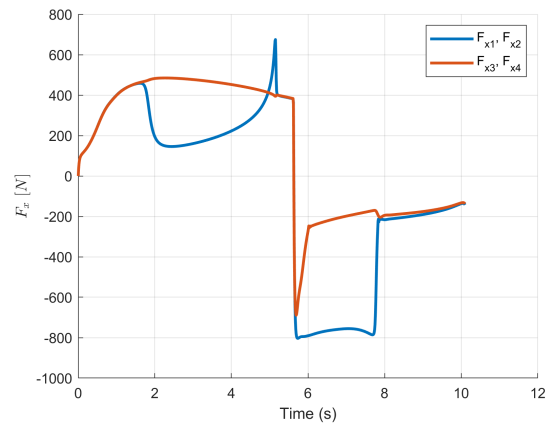
(a) Longitudinal velocity ( $u$ ).



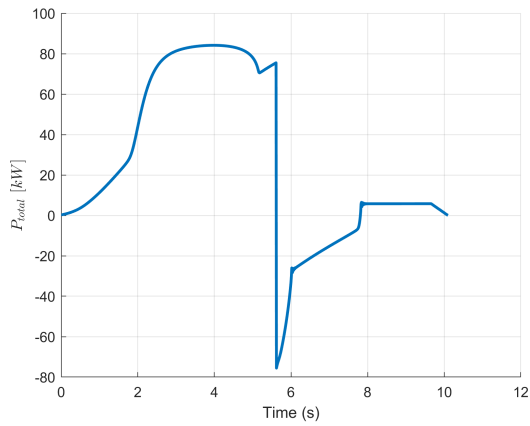
(b) Motor torque commands ( $T_{cmd}$ ) and effective values ( $T_{eff}$ ).



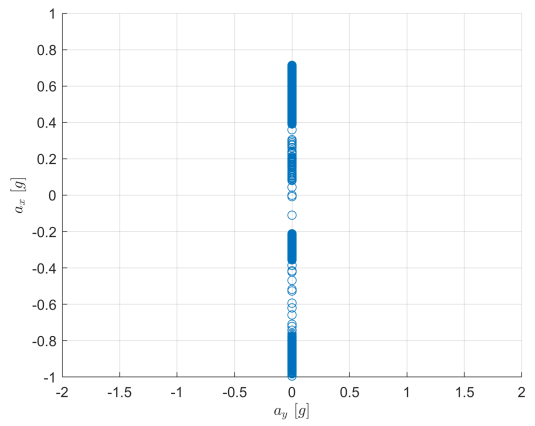
(c) Tire slip ratios ( $\kappa$ ).



(d) Longitudinal tire force  $F_x$ .



(e) Electric power ( $P_{total}$ ).



(f) G-G diagram.

Figure 5.1: Results for the Acceleration event, without traction control.

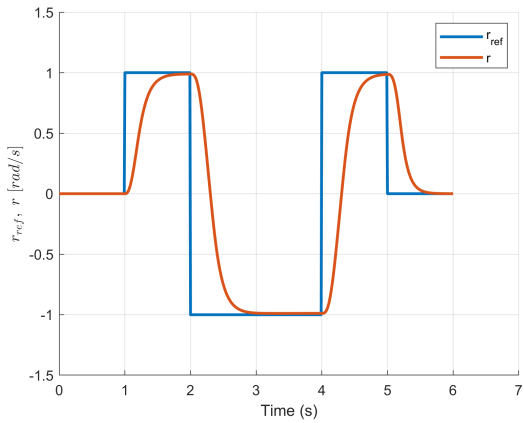


### 5.1.2 Lateral dynamics

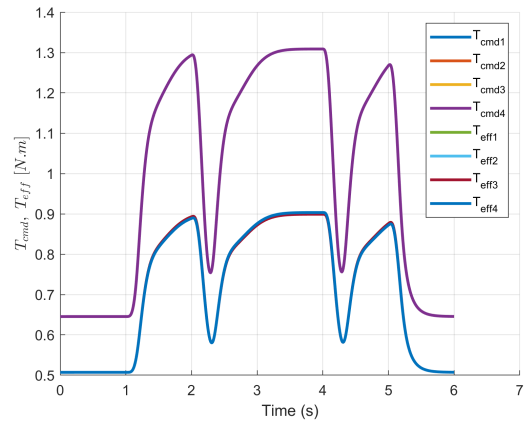
In the scope of this thesis, lateral control corresponds to the feedforward component to the longitudinal controller, caused by gain  $K_r$ , that induces a slip ratio asymmetry and, consequently, a motor torque asymmetry or torque vectoring. To establish the sensitivity to lateral control, the results for a chicane at constant  $u$  are shown in figure 5.2, in which the motor torque commands are all equal, irrespective of tire state.

In this instance, the goal is to track  $r_{ref}$ , while ensuring a constant  $u_{ref}$ . Qualitatively, the reference is adequately followed, with  $J_P = 0.68$  [rad/s], shown in figure 5.2(a). From figure 5.2(b), it is evident that all motor torque commands and effective values are equal, effectively collapsing the eight torque curves into just two. The equal motor torque commands  $T_{ref}$  for all four wheels results, however, in the distinct evolution of  $\kappa$  from figure 5.2(c). The inner wheels always have a higher slip ratio, consistent with what is physically expectable, due to mass transfers. The inner wheels are, therefore, closer to  $\kappa_{critical}$  and, consequently, to the tire stability limit. Regarding the evolution of the slip angles  $\alpha$  from figure 5.2(d), an adequate behaviour, with  $\alpha < \alpha_{critical}$ , is verified. Lastly, concerning the vehicle yawing moment  $T_z$  evolution from figure 5.2(e), it presents an oscillatory behaviour, briefly showing negative values for a turn of positive sign (according to the right-hand rule) and vice-versa. This behaviour should be avoided, since the vehicle's tendency is effectively to rotate in the wrong direction for a short period of time. For lateral performance, the qualitative behaviour of  $T_z$  should be identical to  $r_{ref}$ , a "predictable", piecewise-constant square wave. From figure 5.2(f), one concludes that the chicane is made at approximately constant longitudinal velocity, due to the low  $a_x$  values. Lateral control will aim to increase the  $a_y$  range, the peak and mean values, creating a more responsive behaviour in turns.

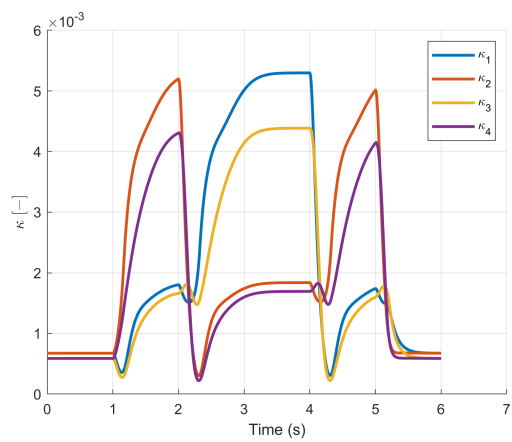
From this analysis, it is possible to conclude that the existence of lateral control is indeed optional, from a safety point of view. The vehicle does not reach the tire stability limits  $\kappa = \kappa_{critical}$  and  $\alpha = \alpha_{critical}$  in the chicane. However, it will be seen that lateral control helps with vehicle rotation while turning, which will inevitably improve lateral performance, especially considering a 4WD vehicle with independent wheel torque actuation.



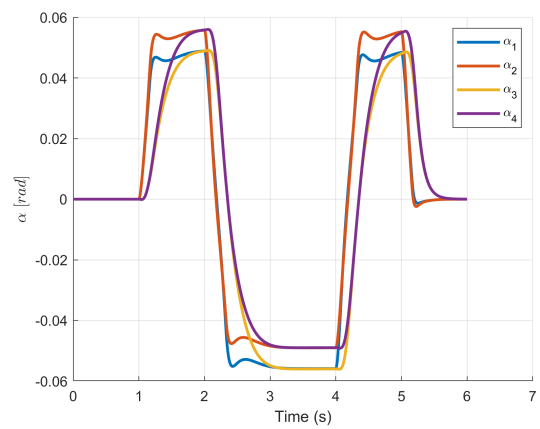
(a) Yaw rate ( $r$ ).



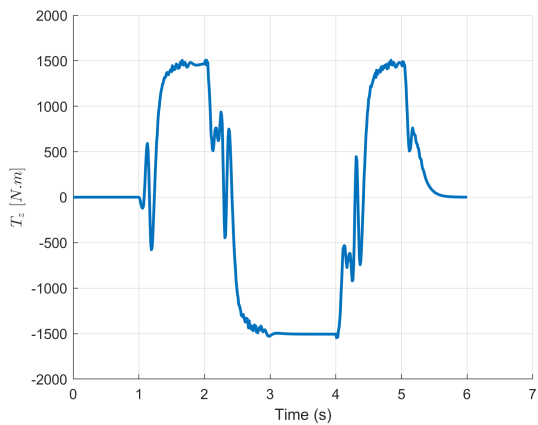
(b) Motor torque commands ( $T_{cmd}$ ) and effective values ( $T_{eff}$ ).



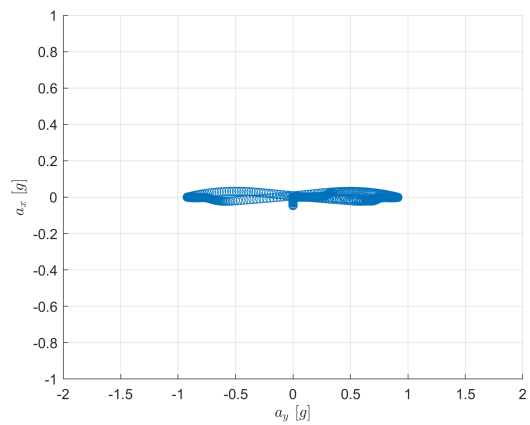
(c) Tire slip ratios ( $\kappa$ ).



(d) Tire slip angles ( $\alpha$ ).



(e) Yawing moment ( $T_z$ ).



(f) G-G diagram.

Figure 5.2: Results for the chicane, without traction control.

## 5.2 Longitudinal performance

To try and improve the baseline longitudinal dynamics presented in section 5.1.1, the procedure from section 4.2 is followed.

1. The admissible tire slip ratio range should be chosen based on the tire curves presented in section 2.1.2. As shown in figure 2.3, the slip ratio  $\kappa_{critical} = \pm 0.07$  [-] corresponds to the optimal operating conditions for maximum force generation in acceleration and deceleration. However, it also corresponds to the tire stability limit, so the controllers must aim to operate within  $|\kappa| < 0.07$  [-].

It is desirable to be more conservative in terms of deceleration to avoid the possibility of wheel-lock. Additionally, the motor regenerative braking ability is inferior to the acceleration ability. For these reasons, the admissible slip ratio range has boundaries  $\kappa_{max} = 0.07$  [-] and  $\kappa_{min} = -0.03$  [-].

2. Since no hydraulic braking system is employed to decelerate the vehicle, the PMSM have both accelerating and decelerating tasks. In motor-operating mode, the maximum combined electrical power should not exceed 80 [kW], as per the competition regulations. However, in generator-operating mode, the bottlenecks are the battery charging characteristics, which is able to charge at up to 30 [kW]. To make use of the full operating range, the electrical power limits are chosen as:  $P_{max} = 80$  [kW] and  $P_{min} = -30$  [kW]. Naturally, the chosen limits lead to peak vehicle performance but may reduce the design life of the powertrain system. Intermediate power limits can be chosen to mitigate these consequences.
3. Starting with the tuning of  $K_{\kappa_f}$  and  $K_{\kappa_r}$  for a constant slip ratio reference and then varying  $K_u$ , the requirements defined in table 4.1 are achieved. The time response created by gains  $K_u = 0.1$ ,  $K_{\kappa_f} = 250$  and  $K_{\kappa_r} = 400$  is shown in figure 5.3. As expected, gain  $K_u$  has a greater influence in velocity tracking, while gains  $K_{\kappa_f}$  and  $K_{\kappa_r}$  have more impact on the slip ratio evolution. The motor torque saturations are set as the hardware limits:  $T_{fmin} = T_{rmin} = -21$  [N.m];  $T_{fmax} = T_{rmax} = 21$  [N.m], without an actual limitation from the power distribution module. Even though the suggested gain combination quickly saturates the rear motor torque values, this is not an adequate way to launch the vehicle from a stand-still, since the motors are inefficient at low speeds, particularly when high torques are requested. The large gap between torque command and the effective value shown in figure 5.3(b) must be mitigated downstream, by adequately setting the motor torque saturations that the power distribution module enforces. Despite this, the controller is able to maintain the slip ratio in the desired range of  $|\kappa| < 0.07$  [-] in all tires, as plotted in figure 5.3(c).

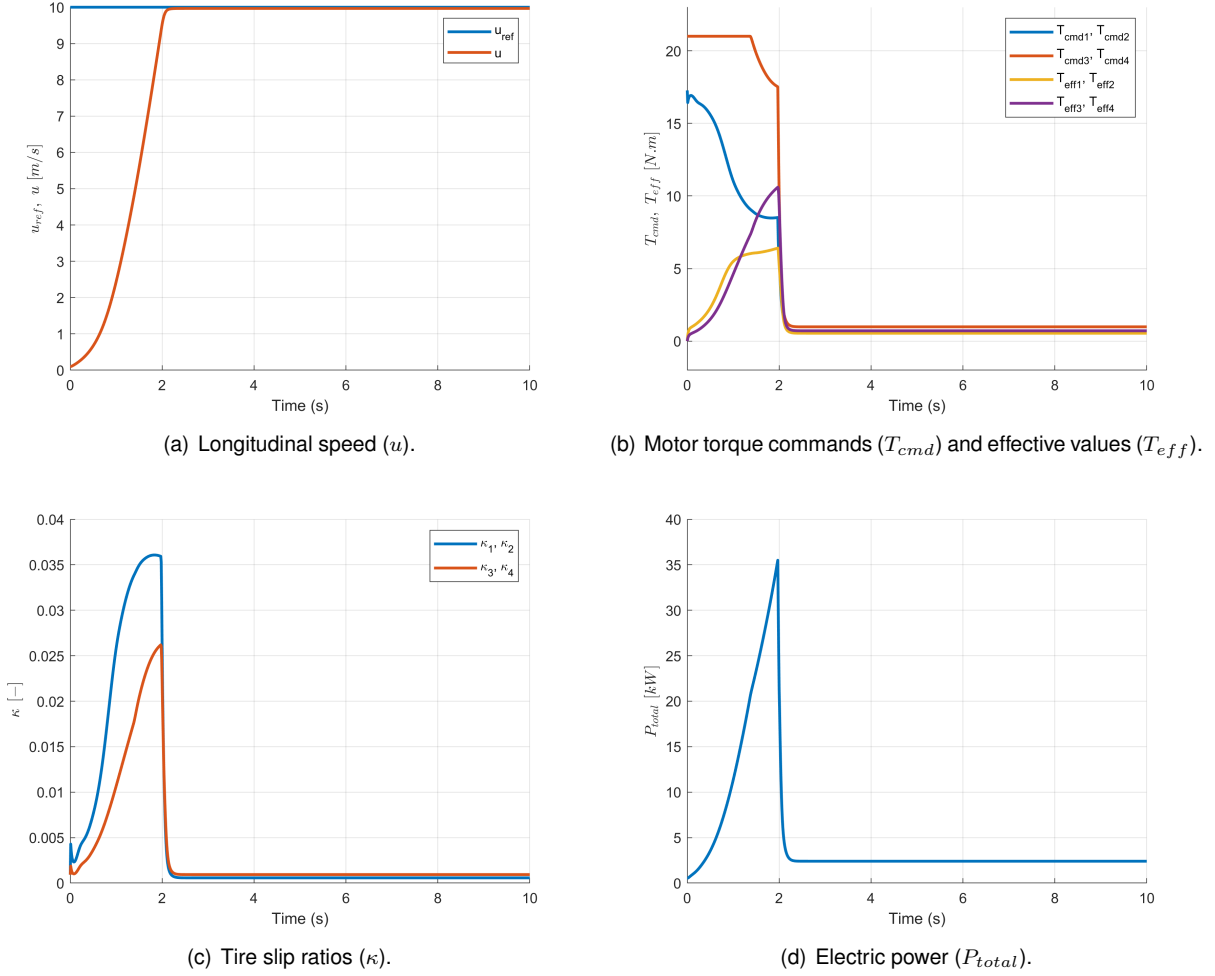


Figure 5.3: Results for a step in longitudinal speed.

4. In order to have a progressively more representative instance of the full longitudinal dynamics, the correct motor torque saturations are studied for an Acceleration event.

The starting point for the search of the torque saturations that yield the best performance in an Acceleration event is chosen as the rated torque, since it represents a condition of stability and longevity for the motors:  $T_{f_{min}} = T_{r_{min}} = -10$  [N.m] and  $T_{f_{max}} = T_{r_{max}} = 10$  [N.m], providing a benchmark for comparison.

Initially, only the accelerating phase of the Acceleration event is considered, corresponding to the timed run. In this instance, the parameter that is expected to have the highest correlation with performance is  $T_{r_{max}}$  since, due to longitudinal mass transfers, the rear axle is more vertically loaded and therefore has the potential to deliver more power than the front one. Starting from 0 [N.m] (FWD only), a  $T_{r_{max}}$  sweep is made with 1 [N.m] increments, as shown in table 5.1.

Increasing  $T_{r_{max}}$  is generally associated with improved performance, or a decrease in  $J_P$ . There is, however, an inflection point for  $T_{r_{max}} = 17$  [N.m], beyond which  $J_P$  slightly increases. The reason for the deterioration in  $J_P$  despite the increase in  $T_{r_{max}}$  is attributed to the motor inefficiency for higher torque values and the fact the electrical power limit is reached sooner for the same

motor speed. The optimum value purely in terms of  $J_P$  is clearly  $T_{r_{max}} = 17$  [N.m], however this configuration leads to a gain of only 0.01 [s] comparing with if  $T_{r_{max}} = 15$  [N.m]. The trade-off between a fraction of a second and a more conservative motor torque value (closer to the nominal torque) allows a higher "torque budget" to be allocated to the front axle before the electrical power limit is reached and operating in a more efficient motor torque range.

Table 5.1:  $T_{r_{max}}$  sweep for an Acceleration event.

$(T_{f_{max}}, T_{r_{max}})$	$J_P$ [s]	Observations
(10,0)	7.75	-
(10,1)	7.21	-
(10,2)	6.86	-
(10,3)	6.47	-
(10,4)	6.18	-
(10,5)	5.85	-
(10,6)	5.83	-
(10,7)	5.67	-
(10,8)	5.52	-
(10,9)	5.40	-
<b>(10,10)</b>	<b>5.29</b>	<b>Benchmark</b>
(10,11)	5.21	-
(10,12)	5.14	-
(10,13)	5.08	-
(10,14)	5.04	-
<b>(10,15)</b>	<b>5.01</b>	<b>Preferable <math>T_{r_{max}}</math></b>
(10,16)	5.01	-
<b>(10,17)</b>	<b>5.00</b>	<b>Lowest <math>J_P</math></b>
(10,18)	5.03	-
(10,19)	5.06	-
(10,20)	5.10	-
(10,21)	5.15	-

In a similar fashion, the optimal front motor torque saturation  $T_{f_{max}}$  is studied, as shown in table 5.2.

The results clearly justify the adoption of a 4WD configuration since, like in the previous analysis, an increase in  $T_{f_{max}}$  is generally associated with a decrease in  $J_P$ . Likewise, an inflection occurs for intermediate values of  $T_{f_{max}}$ , the lowest of which is considered the preferable one. This choice allows the electrical power limit to be reached fractionally later than a higher value of  $T_{f_{max}}$  that would result in the same  $J_P$  value.

Table 5.2:  $T_{f_{max}}$  sweep for an Acceleration event.

$(T_{f_{max}}, T_{r_{max}})$	$J_P$ [s]	Observations
(0,15)	6.99	-
(1,15)	6.49	-
(2,15)	6.20	-
(3,15)	5.88	-
(4,15)	5.64	-
(5,15)	5.49	-
(6,15)	5.36	-
(7,15)	5.23	-
(8,15)	5.12	-
(9,15)	5.04	-
<b>(10,15)</b>	<b>5.01</b>	<b>Lowest <math>J_P</math>; preferable <math>T_{f_{max}}</math></b>
<b>(11,15)</b>	<b>5.01</b>	<b>Lowest <math>J_P</math></b>
<b>(12,15)</b>	<b>5.01</b>	<b>Lowest <math>J_P</math></b>
(13,15)	5.02	-
(14,15)	5.03	-
(15,15)	5.04	-
(16,15)	5.05	-
(17,15)	5.06	-
(18,15)	5.06	-
(19,15)	5.05	-
(20,15)	5.05	-
(21,15)	5.05	-

For the decelerating phase of the Acceleration event, the same approach can be made regarding motor torque saturations  $T_{f_{min}}$  and  $T_{r_{min}}$ . As previously mentioned, the decelerating phase of the Acceleration event is not timed but should happen within a decelerating distance  $d_{dec} < 100$  [m], which is a conservative value. It is expected that, in an emergency situation, a Formula Student car is able to stop from maximum speed in less than half that distance, for dry tarmac conditions. As such, the most relevant performance criterion is the smooth evolution of the tire slip ratio (within the admissible range), to prevent wheel-lock. The motor torque saturations  $T_{f_{min}}$  and  $T_{r_{min}}$  are simultaneously decremented by 1 [N.m], as shown in table 5.3. If the slip ratio evolution is smooth and within the admissible range and simultaneously  $d_{dec} < 100$  [m], the combination of  $(T_{f_{min}}, T_{r_{min}})$  is considered adequate.

Having performed the  $T_{f_{min}}$  and  $T_{r_{min}}$  sweep, one concludes that all motor torque saturations produce an adequate response, except for  $T_{f_{min}} = T_{r_{min}} = -1$  [N.m], which fails to fully stop the vehicle within 100 [m]. Decreasing the  $T_{f_{min}}$  and  $T_{r_{min}}$  any further than  $-7$  [N.m] results in a plateau in  $d_{dec}$ , directly influenced by the admissible slip ratio range, namely  $\kappa_{min}$ . Since gains  $K_{\kappa_f}$  and  $K_{\kappa_r}$  are biased towards the rear axle (useful during the accelerating phase), it is not advisable that  $|T_{r_{min}}| > |T_{f_{min}}|$ , since the rear axle becomes less vertically loaded than the front one during braking, and it may lead to vehicle instability.

Table 5.3:  $T_{f_{min}}$  and  $T_{r_{min}}$  sweep for an Acceleration event.

$(T_{f_{max}}, T_{f_{min}}, T_{r_{max}}, T_{r_{min}})$	$d_{dec}$ [m]	Observations
(10,-1,15,-1)	131	Inadequate response
(10,-2,15,-2)	91	Adequate response
(10,-3,15,-3)	76	Adequate response
(10,-4,15,-4)	64	Adequate response
(10,-5,15,-5)	59	Adequate response
(10,-6,15,-6)	60	Adequate response

Finally, in figure 5.4 are shown the results for the complete Acceleration event, produced by:

- $K_u = 0.1$ ,  $K_{\kappa_f} = 250$ ,  $K_{\kappa_r} = 400$ ;
- $\kappa_{max} = 0.07$ ,  $\kappa_{min} = -0.03$  [-];
- $T_{f_{max}} = 10$ ,  $T_{f_{min}} = -5$ ,  $T_{r_{max}} = 15$ ,  $T_{r_{min}} = -5$  [N.m];
- $P_{max} = 80$ ,  $P_{min} = -30$  [kW].

The vehicle is able to successfully complete the Acceleration event in a stable fashion, almost reaching the desired top speed  $u_{ref} = 29$  [m/s] within 1 [%] error, and gradually coming to a stop (corresponding to  $u_{ref} = 0.5$  [m/s]), as shown in figure 5.4(a). Inspecting figure 5.4(c), one concludes that tire slip is kept within the strictly ascending part of the tire curve during acceleration and the strictly descending part during deceleration or, more formally,  $|\kappa| < \kappa_{critical}$ . The most important consequence of this fact is that the longitudinal force evolution, plotted in figure 5.4(d), is smooth and relatively close to the limits defined by the  $F_x(\kappa)$  curve from figure 2.3(a), in contrast with the case where traction control is not employed, shown in figure 5.1(d). The power requirements are observed, since both the motor power limit in acceleration and deceleration are reached, and the controller gradually decreases (in absolute value) the torque reference to ensure the limits are maintained, as proved in figure 5.4(e). An obvious conclusion, and perhaps the biggest performance limiting factor, is that the PMSM are very inefficient in low motor speeds and relatively high torques, essentially making the traction control task at the beginning of the Acceleration event easier, but creating a substantial gap between torque command and effective value, as shown in figure 5.4(b). Comparing with figure 5.1(f), the G-G diagram from figure 5.4(f) shows clear improvements. Even though  $a_{x_{max}}$  and  $a_{x_{min}}$  have comparable magnitudes, now the points are biased towards the extremities, showing higher mean  $a_x$  in both phases of the Acceleration event and an improvement of 11 [%] in  $J_P$ .

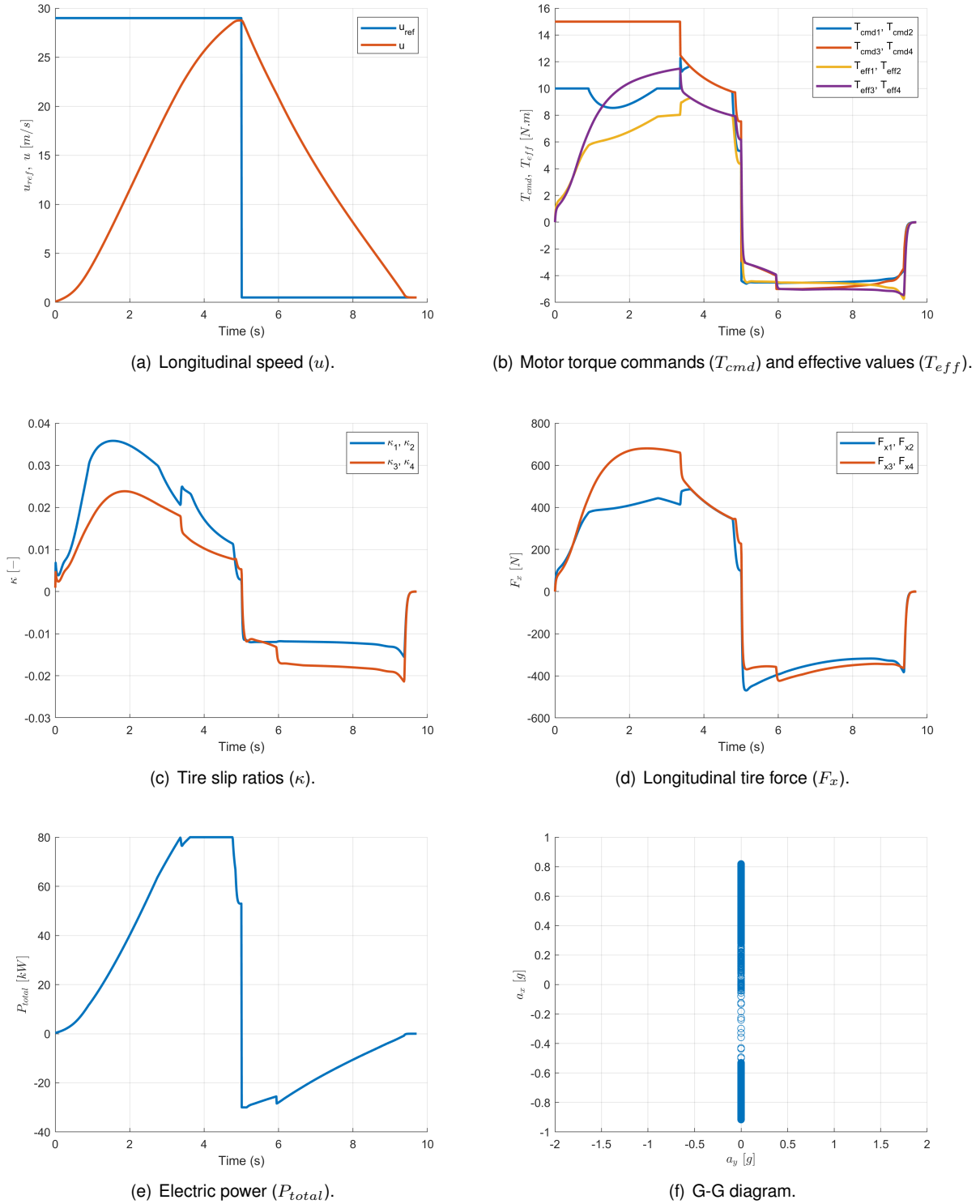


Figure 5.4: Results for the Acceleration event, with traction control.

5. Traction controllers must be robust to changes in parameters, namely due to uncertainties or dynamic changes during the vehicle's life cycle.

The friction coefficient  $\mu$  conveniently encompasses variations in traction, either due to changes on the road surface or tire operating conditions, such as pressure and temperature. The traction controllers are designed around a nominal/intermediate friction coefficient  $\mu = 1$  [-] but, ideally,



should present satisfactory responses - in terms of safety but also pure performance - for worse traction conditions (for instance in a rainy race track) but also if the traction level is superior to the design conditions (for very good quality tarmac). Using the previously-mentioned parameter combination, the friction coefficient is varied for an Acceleration event, as documented in table 5.4. As logic would suggest, a decrease in  $\mu$  leads to a deterioration in  $J_P$ . Since, for lower  $\mu$ , the longitudinal slip stiffness decreases, tires slip more easily, requiring a lower torque command to achieve the desired  $\kappa_{ref}$  - translating in a lower amount of torque available to drive the vehicle. Conversely, the performance gain for  $\mu > 1$  [-] is negligible since the longitudinal slip stiffness increase is largely offset by the lower tire slip, effectively resulting in a similar driving force  $F_x$ , comparing to the design condition of  $\mu = 1$  [-]. To produce significant improvements in  $J_P$ , higher effective torque values would be needed, to bring the tire slip ratio closer to the optimal value of  $\kappa_{critical} = 0.07$  [-]. The decelerating distance requirement is observed irrespective of variations in  $\mu$ .

Table 5.4:  $\mu$  sensitivity for an Acceleration event.

$\mu$ [-]	$J_P$ [s]	$d_{dec}$ [m]	Observations
0.5	5.87	71	-
0.6	5.50	69	-
0.7	5.26	67	-
0.8	5.11	64	-
0.9	5.05	61	-
<b>1.0</b>	<b>5.01</b>	<b>59</b>	<b>Benchmark</b>
1.1	4.98	58	-
1.2	4.97	57	-
1.3	4.96	57	-
1.4	4.96	57	-
1.5	4.96	56	-

Regarding the sensitivity to changes in vehicle mass  $m$ , there is a significant correlation between increases in mass and in  $J_P$ , as shown in table 5.5. From this analysis, it is possible to determine the impact of a driver's mass in performance, corresponding to approximately  $\Delta m = +30$  [%], or 77 [kg]. Conversely, it is useful to determine the impact that mass reduction would have, especially for future prototypes. Exhibiting a quasi-linear relationship, one can conclude that the performance loss in an Acceleration event is approximately 0.07 [s] per 10 [kg] mass increase.

Table 5.5:  $m$  sensitivity for an Acceleration event.

$\Delta m$ [%]	$J_P$ [s]	$d_{dec}$ [m]	Observations
-30	4.50	47	-
-25	4.57	49	-
-20	4.65	51	-
-15	4.74	53	-
-10	4.83	53	-
-5	4.92	57	-
<b>0</b>	<b>5.01</b>	<b>59</b>	<b>Benchmark</b>
+5	5.10	61	-
+10	5.20	63	-
+15	5.29	65	-
+20	5.36	66	-
+25	5.49	67	-
+30	5.59	68	-

The last parameter that has a significant impact on traction is the tire radius  $R$ , which may vary dynamically due to vertical load transfer, changes in tire pressure/temperature and wear level. Additionally, variations in tire radius can occur if future prototypes are fitted with a different tire model - assuming no changes in tire characteristics other than radius. As a rule of thumb, the changes should be within  $\pm 10$  [%] of the current tire radius value. The effect that these variations would have with respect to an Acceleration event is shown in table 5.6. For a given motor torque command, a tire with a higher  $R$  will transmit a lower driving force  $F_x$ . This simple principle justifies the improvements in  $J_P$  for smaller tires. However, a higher driving force sacrifices the vehicle's top speed: for all cases of  $\Delta R < 0$  [%], the maximum motor speed  $\omega_{m_{max}}$  is achieved, entering the zero-torque/zero-power zone, which should be avoided to preserve the powertrain. This can be overcome by adjusting  $u_{ref}$ , as suggested in section 4.2. Still, since  $\omega_{m_{max}}$  is very rarely achieved (other than in Acceleration events), it may be a good design principle to choose smaller tires for future prototypes, purely from a performance perspective. To create the same driving force, lower motor torques are required, possibly allowing to operate within a more efficient range of the motor map shown in table 2.4. Additionally, lower-radius tires are often associated with a lower overall vehicle mass, contributing to an extra performance gain, as discussed in the previous table.

Table 5.6:  $R$  sensitivity for an Acceleration event.

$\Delta R$ [%]	$J_P$ [s]	$d_{dec}$ [m]	Observations
-10	4.88	49	$\omega_{m_{max}}$ reached
-7.5	4.90	52	$\omega_{m_{max}}$ reached
-5	4.93	55	$\omega_{m_{max}}$ reached
-2.5	4.97	58	$\omega_{m_{max}}$ reached
<b>0</b>	<b>5.01</b>	<b>59</b>	<b>Benchmark</b>
+2.5	5.06	60	-
+5	5.11	61	-
+7.5	5.17	62	-
+10	5.23	63	-

## 5.3 Lateral performance

To try and improve the baseline lateral dynamics described in section 5.1.2, the procedure from section 4.3 is followed.

1. The yaw rate reference  $r_{ref}$ , defined in equation (3.17), combines two inputs:  $u_{ref}$  and  $\delta_{ref}$ . Conceptually, the desired  $r_{ref} = 1$  [rad/s] can be obtained using low values for  $u_{ref}$  and high values for  $\delta_{ref}$ , vice-versa, or intermediate values for both. In this analysis,  $u_{ref}$  is set as the maximum value up to which the Skid Pad event is made with a safety margin of 0.5 [m] (distance to the closest cones), without lateral control, or  $K_r = 0$ . This value is  $u_{ref} = 9$  [m/s] and, to achieve the desired  $r_{ref} = 1$  [rad/s], the required steering wheel angle is  $\delta_{ref} = 1.027$  [rad].

Gain  $K_u$  is determined as the minimum value that allows the tracking error of  $u_{ref} = 9$  [m/s] to be within 1 [%], the range within which  $u$  is considered constant. The minimum value is chosen, since the relative weights of  $K_u$  and  $K_r$  dictate which command ( $u_{ref}$  or  $r_{ref}$ ) is preferentially followed:  $K_u = 0.1$ . Regarding the inner loop gains of the cascade,  $K_{\kappa_f}$  and  $K_{\kappa_r}$ , they were set as equal to express no preferential axle;  $K_{\kappa_f} = K_{\kappa_r} = 300$ . Additionally, since all tests are performed at  $u \approx 9$  [m/s], with approximately null longitudinal acceleration, the motor torque saturations are set as conservative values, the nominal torque:  $T_{fmax} = T_{rmax} = 10$ ,  $T_{fmin} = T_{rmin} = -10$  [N.m]. Additionally, this choice prevents the existence of motor torque spikes, since the yaw rate references are abrupt and discontinuous, to test the traction controllers for the worst-case scenario.

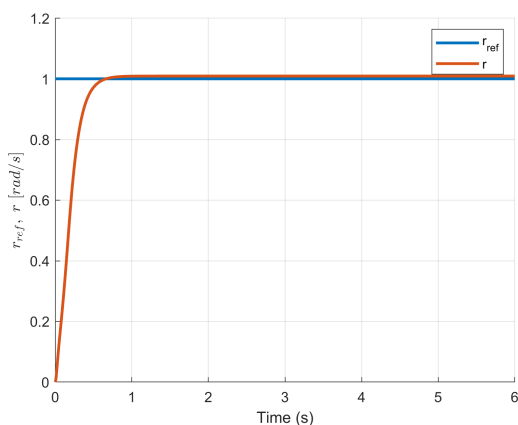
2. One of the main goals of the traction controllers is to keep  $\kappa_{min} < \kappa < \kappa_{max}$  [-]. Since the lateral controller tests are designed at a constant  $u$ , it is expected that the baseline tire slip ratios are low in absolute value, close to zero. For these reasons, the maximum slip ratio asymmetries that enter the feedforward component of the longitudinal controller are set as  $\kappa_{diffmax} = 0.03$ ,  $\kappa_{diffmin} = -0.03$  [-], as there is no preferential turning side in the following tests. The slip ratio saturations of the longitudinal controller are kept as  $\kappa_{max} = 0.07$ ,  $\kappa_{min} = -0.03$  [-].
3. In order to investigate the relationship between the magnitudes of  $K_u$  and  $K_r$ , a sweep of  $K_r$  is performed, as documented in table 5.7.  $K_r = 0$  corresponds to the case of no lateral control. It is possible to observe that all metrics improve if  $K_r > 0$ : for the step input, chicane and the qualitative slip ratio requirements.

As  $K_r$  is progressively increased, one observes improvements in terms of rise time and steady-state error for the constant yaw rate reference. However, regarding the chicane, for  $K_r > 0.03$ , a plateau in  $J_P$  is reached. The qualitative slip ratio requirements are fulfilled, for any  $K_r \geq 0.1$ . Considering that the minimum  $K_r$  that fulfills all performance requirements must be chosen, gain  $K_r = 0.03$  is considered optimal for this analysis.

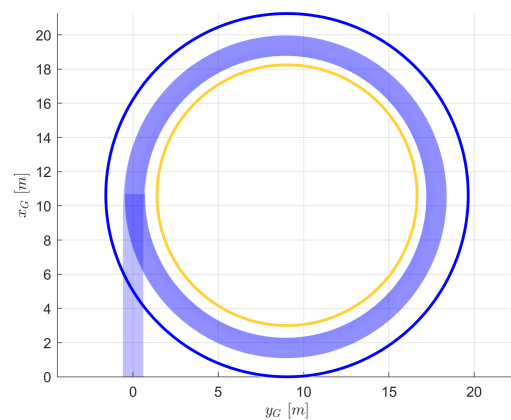
Table 5.7:  $K_r$  sweep.

$K_r$	Step input of $r_{ref} = 1$ [rad/s]		Chicane	Slip ratio requirements
	Rise time	Steady-state error	$J_P$	
0	0.33	1.3	0.68	Not fulfilled
0.01	0.33	1.2	0.64	Fulfilled
0.02	0.34	1.0	0.61	Fulfilled
<b>0.03</b>	<b>0.33</b>	<b>0.9</b>	<b>0.60</b>	<b>Fulfilled</b>
0.04	0.32	0.9	0.60	Fulfilled
0.05	0.30	0.8	0.60	Fulfilled
0.06	0.29	0.8	0.60	Fulfilled
0.07	0.28	0.7	0.60	Fulfilled
0.08	0.27	0.6	0.60	Fulfilled
0.09	0.26	0.6	0.60	Fulfilled
0.1	0.26	0.6	0.60	Fulfilled

To better understand how both instances of lateral dynamics translate into vehicle motion, figures 5.5 and 5.6 show the yaw rate references and responses, as well as the resulting vehicle paths, shown in light blue. The paths width corresponds to the vehicle track width  $L_t$ . If the unitary yaw rate reference from figure 5.5(a) is extended up to approximately  $t = 14$  [s], the resulting path is half of a Skid Pad, as shown in figure 5.5(b). The darker blue regions refer to a path overlap. To complete the full Skid Pad event, the yaw rate reference would need to be inverted,  $r_{ref} = -1$  [rad/s], at approximately  $t = 14$  [s]. It is worth mentioning that, in practice, a race car is not able to perform a full Skid Pad event without a proper guidance logic, because online input corrections are necessary when the control algorithms depend on perception hardware and there is a certain mismatch between the ideal Skid Pad configuration and the physical one, as well as external disturbances such as wind effects or road imperfections.



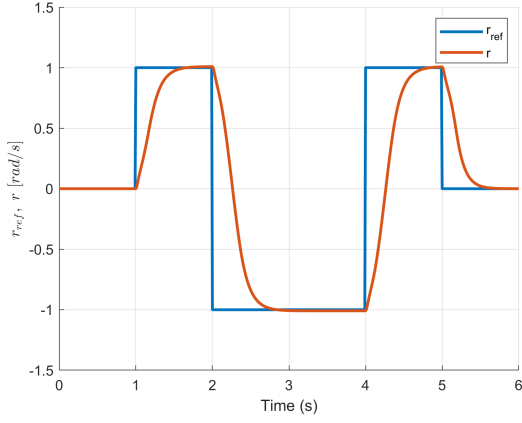
(a) Unitary yaw rate reference and response.



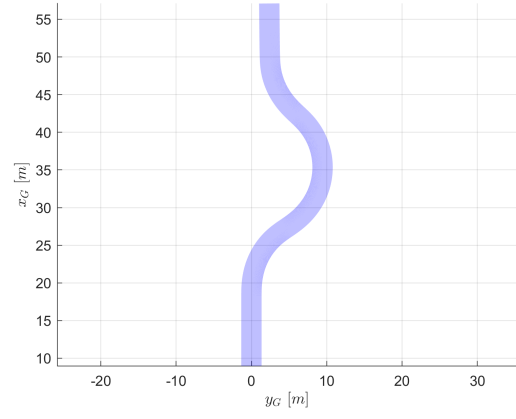
(b) Extended vehicle path for  $r_{ref} = 1$  rad/s.

Figure 5.5: Yaw rate response for a step input and resulting vehicle path.

The yaw rate response from figure 5.6(a) results in the vehicle path depicted in figure 5.6(b), performed at constant  $u$ , which is a common manoeuvre in racing.



(a) Chicane yaw rate reference and response.



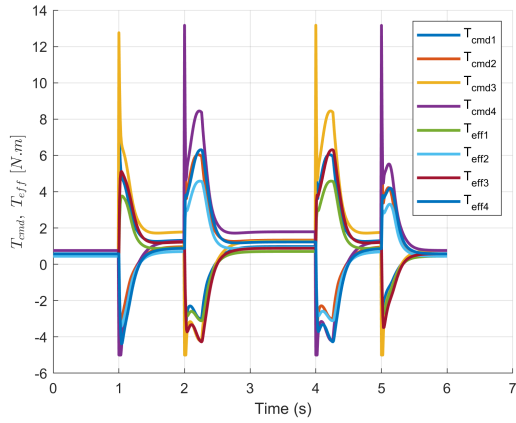
(b) Vehicle path for a chicane.

Figure 5.6: Yaw rate response for a chicane and resulting vehicle path.

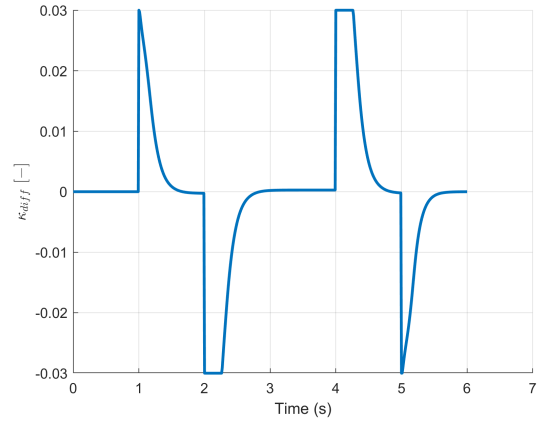
Shown in figure 5.7 are the results for a chicane, produced by:

- $K_u = 0.1, K_{\kappa_f} = 300, K_{\kappa_r} = 300$ ;
- $\kappa_{max} = 0.07, \kappa_{min} = -0.03$  [-];
- $K_r = 0.03$ ;
- $\kappa_{diff_{max}} = 0.03, \kappa_{diff_{min}} = -0.03$  [-];
- $T_{f_{max}} = 10, T_{f_{min}} = -10, T_{r_{max}} = 10, T_{r_{min}} = -10$  [N.m].

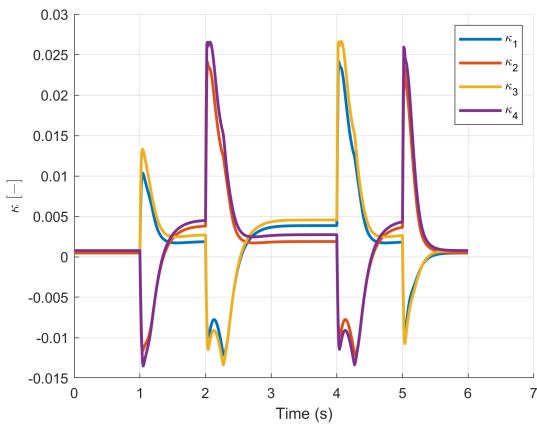
As shown in figure 5.7(b), a slip ratio difference  $\kappa_{diff}$  from inner to outer wheels is introduced, creating motor torque asymmetries, particularly during the transient phases of the chicane, as depicted in figure 5.7(a). The motor torque asymmetry also induces the desirable slip ratio evolution from figure 5.7(c). Since  $\kappa_{min} < 0$ , negative motor torque values are allowed, effectively braking the inner wheels to assist in the yaw motion. If, for any reason, one wishes to obtain only positive torque values, this saturation can be changed, which directly influences the torque command of the inner wheels. Considering the  $F_x(\kappa)$  tire curve from figure 2.3(a), one concludes that  $|\kappa| < \kappa_{critical}$  during the entire chicane. Regarding the tire slip angles, even though they are not directly controlled, they are also kept within the critical values of the  $F_y(\alpha)$  tire curve from figure 2.3(b),  $|\alpha| < \alpha_{critical}$ . As suggested in section 5.1.1, the temporal evolution of  $T_z$  should be less oscillatory and qualitatively resemble  $r_{ref}$ . The addition of a lateral control component,  $K_r > 0$ , modifies the transient evolution of  $T_z$  so that it is less oscillatory. For  $K_r \geq 0.4$ ,  $T_z$  is strictly consistent with the sign of  $r_{ref}$ . Even with  $K_r = 0.3$ , the response shows significant improvements over a situation where there is not lateral control, as figure 5.7(e) demonstrates. Comparing the G-G diagram obtained with lateral control, shown in figure 5.7(f), with the one from figure 5.2(f), similar values of  $a_y$  are achieved, however since negative motor torques are allowed while turning, the  $a_x$  evolution is more evident, effectively working to keep a constant speed  $u$  despite the introduction of negative motor torques in turns.



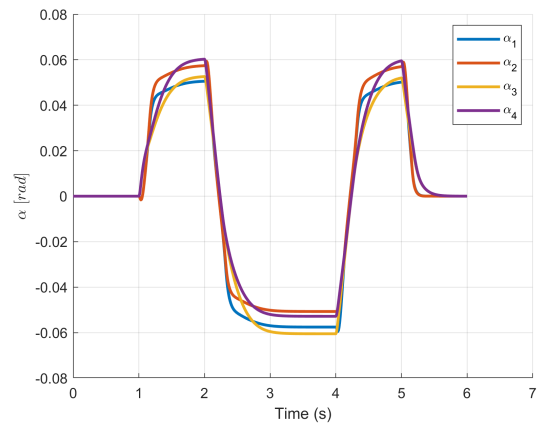
(a) Motor torque commands ( $T_{cmd}$ ) and effective values ( $T_{eff}$ ).



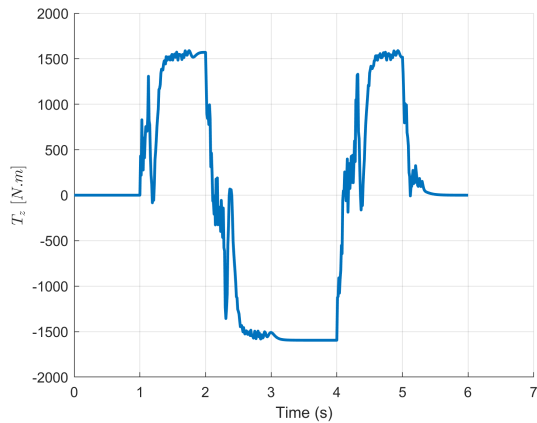
(b) Slip ratio difference ( $\kappa_{diff}$ ).



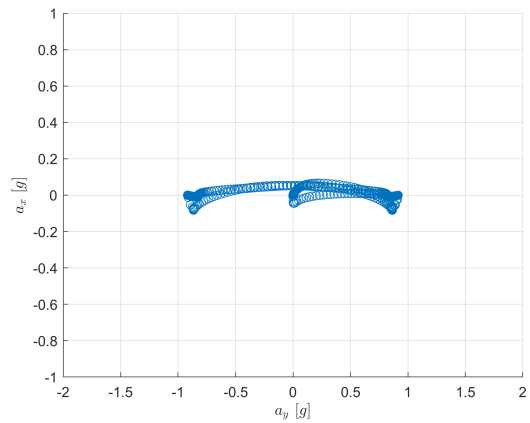
(c) Tire slip ratios ( $\kappa$ ).



(d) Tire slip angles ( $\alpha$ ).



(e) Yawing moment ( $T_z$ ).



(f) G-G diagram.

Figure 5.7: Results for the chicane, with lateral control.

4. It is important to assess whether the proposed solution would still work for traction conditions that are different to the design ones. In table 5.8 the vehicle's sensitivity to changes in friction coefficient  $\mu$  is presented, for a chicane.

As expected, for  $\mu < 1$  [-],  $J_P$  increases, which means that the reference tracking error increases. However, for  $\mu \leq 0.7$ , the maximum absolute yaw rate value drops below  $r = 1$  [rad/s], because

the car starts to slide laterally or, more formally,  $|\alpha| > \alpha_{critical}$ . When this behaviour ensues, additional steering wheel lock or motor torque asymmetry will not help in achieving the desired yaw rate. The vehicle is under-steering, not being able to perform the manoeuvre. Even when the vehicle under-steers, the values of the slip ratio are kept within  $|\kappa| < \kappa_{critical}$ , since the variable is actively controlled.

For better traction conditions than the design ones, or  $\mu > 1$  [-],  $J_P$  slightly improves. To obtain significant improvements in  $J_P$ , higher values of  $\kappa$  and  $\alpha$  are necessary, created by an increase in gains  $K_{\kappa_f}$ ,  $K_{\kappa_r}$  and  $K_r$ .

Table 5.8:  $\mu$  sensitivity for a chicane.

$\mu$ [-]	$J_P$ [rad/s]	Observations
0.5	No physical meaning	$ r _{max} = 0.84$ [rad/s]
0.6	No physical meaning	$ r _{max} = 0.88$ [rad/s]
0.7	No physical meaning	$ r _{max} = 0.94$ [rad/s]
0.8	0.62	-
0.9	0.61	-
<b>1.0</b>	<b>0.60</b>	<b>Benchmark</b>
1.1	0.60	-
1.2	0.60	-
1.3	0.59	-
1.4	0.59	-
1.5	0.59	-

## 5.4 Combined performance

The significance of this section is to assess whether the suggested approach of tuning the traction controllers for independent, simple instances of "pure" longitudinal and lateral dynamics, will translate into a combined solution that works in two generic race tracks, from previous Formula Student Germany (FSG) and Formula Student Italy (FSI) competitions. To validate the traction controllers, the procedure from section 4.4 is followed.

1. Unlike the relatively straightforward Acceleration and Skid Pad events and a chicane, the generic race tracks require a guidance logic, that updates and corrects the vehicle behaviour online. The guidance logic implemented in this thesis corresponds to the "High-level planning" and "Mid-level controllers" blocks from figure 3.1. To create instances in which the traction controllers are validated according to several traction levels, three sets of trajectories are defined for each race track. The desired path is common in all trajectories, but the velocity profile is variable, which heavily influences  $t_{lap}$ . It is expected that the more conservative velocity profiles can be adequately tracked even in lower-traction conditions, or lower  $\mu$ . Conversely, the more demanding velocity profiles should only produce valid runs for higher  $\mu$  values.

To define the velocity profiles, two additional parameters are introduced, torque fraction  $TF$  and maximum longitudinal speed  $u_{max}$ , such that:

$$TF = \frac{\text{Available motor torque}}{\text{Maximum motor torque}} \quad [-]; \quad (5.1)$$

$$0 < u(t) < u_{max}(t) \quad [\text{m/s}]; \quad (5.2)$$

aiming to limit the vehicle's longitudinal acceleration and speed by adjusting the velocity profile.

The creation of trajectories according to the expected race track traction conditions allows one to decide how conservatively the car should drive on the Trackdrive event. If the traction conditions are expected to be good (from on-site testing or feedback from other teams), one may chose to adopt the intermediate traction trajectory, and then assess whether to upgrade to the excellent traction or downgrade to the poor traction one, based on the results. If, however, a more conservative approach is desirable, or the team expects unfavourable traction conditions (for instance, in a wet race track), choosing the poor traction trajectory may be appropriate, to perform a benchmark run. After that, to tentatively improve the lap times, the intermediate traction trajectory may be employed if the team decides there is margin for improvement. The three trajectory sets are created according to the parameters found in table 5.9.

Table 5.9: Parameters considered for trajectory generation.

Traction levels	$TF$ [-]	$u_{max}$ [m/s]
Poor	0.25	10
Intermediate	0.50	12.5
Excellent	0.75	15



2. The simulation results for the FSG and FSI race tracks are shown in tables 5.10 and 5.11, respectively. The performances indexes  $J_{P_u}$ ,  $J_{P_r}$  and  $t_{lap}$  are computed for a range of friction coefficients  $0.5 \leq \mu \leq 1.5$  [-].

Table 5.10:  $\mu$  sensitivity for the FSG race track.

$\mu$ [-]	Poor traction			Intermediate traction			Excellent traction		
	$J_{P_u}$ [m/s]	$J_{P_r}$ [rad/s]	$t_{lap}$ [s]	$J_{P_u}$ [m/s]	$J_{P_r}$ [rad/s]	$t_{lap}$ [s]	$J_{P_u}$ [m/s]	$J_{P_r}$ [rad/s]	$t_{lap}$ [s]
0.5		DNF			DNF			DNF	
0.6		DNF			DNF			DNF	
0.7	0.38	0.19	35.3		DNF			DNF	
0.8	0.38	0.18	35.2		DNF			DNF	
0.9	0.38	0.18	35.1		DNF			DNF	
1.0	0.37	0.18	35.1	0.72	0.29	28.7		DNF	
1.1	0.37	0.18	35.1	0.72	0.29	28.6		DNF	
1.2	0.37	0.18	35.0	0.71	0.29	28.6	1.16	0.39	25.1
1.3	0.37	0.18	35.0	0.71	0.29	28.6	1.15	0.39	25.0
1.4	0.37	0.18	35.0	0.71	0.28	28.6	1.15	0.38	24.9
1.5	0.37	0.18	35.0	0.71	0.28	28.5	1.14	0.38	24.9

Table 5.11:  $\mu$  sensitivity for the FSI race track.

$\mu$ [-]	Poor traction			Intermediate traction			Excellent traction		
	$J_{P_u}$ [m/s]	$J_{P_r}$ [rad/s]	$t_{lap}$ [s]	$J_{P_u}$ [m/s]	$J_{P_r}$ [rad/s]	$t_{lap}$ [s]	$J_{P_u}$ [m/s]	$J_{P_r}$ [rad/s]	$t_{lap}$ [s]
0.5		DNF			DNF			DNF	
0.6		DNF			DNF			DNF	
0.7	0.49	0.28	27.1		DNF			DNF	
0.8	0.49	0.27	27.0		DNF			DNF	
0.9	0.49	0.27	26.9		DNF			DNF	
1.0	0.49	0.27	26.9	0.77	0.40	22.1		DNF	
1.1	0.49	0.27	26.9	0.77	0.39	22.0		DNF	
1.2	0.49	0.27	26.9	0.77	0.39	22.0	0.93	0.54	19.6
1.3	0.49	0.26	26.8	0.77	0.39	22.0	0.93	0.46	19.4
1.4	0.49	0.26	26.8	0.77	0.39	22.0	0.92	0.46	19.4
1.5	0.48	0.26	26.8	0.77	0.39	21.9	0.92	0.45	19.3

3. The learnings from the simulations documented in tables 5.10 and 5.11 are quite identical for both race tracks, despite the FSI race track having a higher degree of complexity. Since it is more elongated, with lower-radius turns at both extremities, higher yaw accelerations and velocities occur.

It can be observed that, for  $\mu < 0.7$  [-], the traction controllers are not able to keep the vehicle within the track limits, irrespective of the trajectory category, resulting in a DNF. If such poor traction conditions are expected, the trajectory must be updated, further decreasing  $TF$  and/or  $u_{max}$ . The critical  $\mu$  value for which the run is successfully completed (non-DNF) increases as the trajectory becomes more demanding from a velocity profile point of view.

Provided that the vehicle does not run off-track, the performance indexes  $J_{P_u}$  and  $J_{P_r}$  remain approximately constant for the entire  $\mu$  range, showing a very slight improvement as  $\mu$  increases. Performance indexes  $J_{P_u}$  and  $J_{P_r}$  consistently increase for more demanding trajectory categories, which can be explained due to the vehicle's constant translational and rotational inertia. The more demanding the velocity profile is, the longer it takes for  $u_{ref}$  and  $r_{ref}$  to be tracked, contributing to increases in  $J_{P_u}$  and  $J_{P_r}$ .

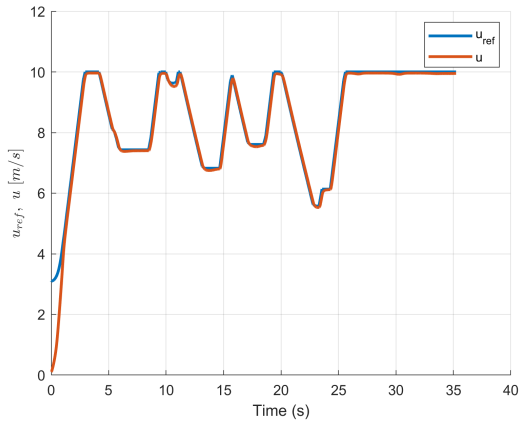
The lap time  $t_{lap}$  is approximately constant for each trajectory category, showing slight improvements as  $\mu$  increases, but drastic changes for the three trajectory categories, showing a much stronger correlation with the guidance logic than with the traction controllers performance, as expected.

4. Due to the high number of simulation results, only the extreme cases that resulted in non-DNF runs are discussed, corresponding to the poor traction trajectory with  $\mu = 0.7$  [-] and the excellent traction one with  $\mu = 1.5$  [-]. The extreme cases illustrate the boundaries of the expected traction control operating conditions, encompassing a wide spectrum of vehicle performance.

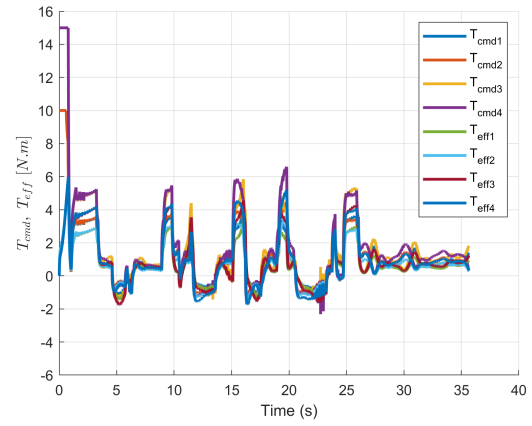
From the results documented in figures 5.8-5.11 it is clear that the independent tuning process for longitudinal and lateral dynamics results in a combined solution that presents satisfactory results for two increasingly complex race tracks - for a wide range of friction coefficient values and for three levels of performance in terms of trajectory generation, as documented in tables 5.10 and 5.11.

Even though the desired path is common for the three trajectory categories, the variation of parameters  $TF$  and  $u_{max}$ , as suggested in table 5.9, allowed the significant differences in  $u_{ref}$ , as documented in figures 5.8-5.11(a). Consequently, to track the varying longitudinal velocity profiles, the motor torque responses, shown in figures 5.8-5.11(b), also vary significantly. It is clear that, in the first seconds after the stand still start, tire traction is the limiting factor in terms of slip ratio evolution for the poor traction conditions, as observed in figures 5.8(c) and 5.10(c). For the excellent traction conditions shown in figures 5.9(c) and 5.11(c) the limiting factor is actually motor torque availability, since it is saturated during the first branch of  $u_{ref}$ . Throughout the rest of the run, the motor torque values are very low for the poor traction conditions and saturate in the maximum values (in straights) often for the excellent traction conditions, showing the desir-

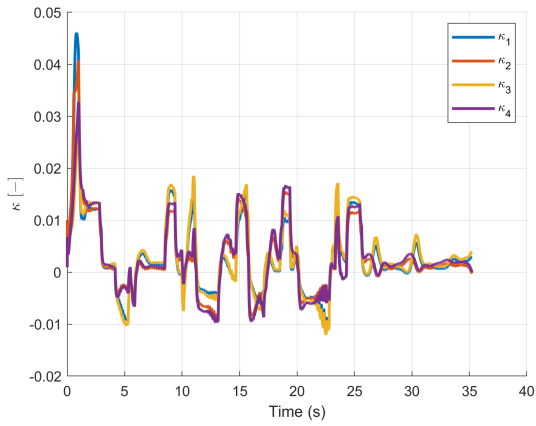
able robustness to traction levels. Tire state constraints are always observed,  $|\kappa| < \kappa_{critical}$ , a paramount requirement of this TCS. Even though it is not shown,  $|\alpha| < \alpha_{critical}$ , since when that condition is not met, the run usually results in a DNF due to lateral sliding - which can happen even if  $|\kappa| < \kappa_{critical}$ . Regarding lateral dynamics, since the yaw rate definition (3.17) includes  $u_{ref}$ , it is expected that the yaw rate profile is more demanding for better traction conditions, as seen in figures 5.8-5.11(d). One observes, however, that  $r_{ref}$  is adequate to the existing traction conditions, since the profile is always well tracked. To test the control system's robustness, the vehicle is placed intentionally shifted from the desired path at the beginning of the simulation, the reason why the initial  $r_{ref}$  has a much higher magnitude than during the rest of the run. Regarding the electrical power requirements, one concludes that they are observed irrespective of traction conditions and adopted trajectory, as documented in figures 5.8-5.11(e), although with a stark difference in energy consumption between both extreme cases. The much lower  $P_{min}$  - due to the battery charging characteristics - compared with  $P_{max}$  proves not be a problem in decelerating the vehicle. The lower limit is never reached, however significant longitudinal decelerations are achieved, if one inspects the G-G diagrams for excellent traction conditions 5.9 and 5.11(f). As expected, for poor traction conditions, the G-G diagrams from figures 5.8 and 5.10(f) show a high point density around the origin, which means the longitudinal and lateral accelerations are much lower than the excellent traction trajectory counterparts.



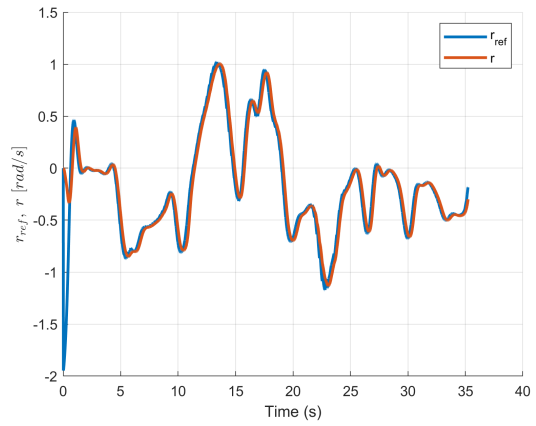
(a) Longitudinal speed ( $u$ ).



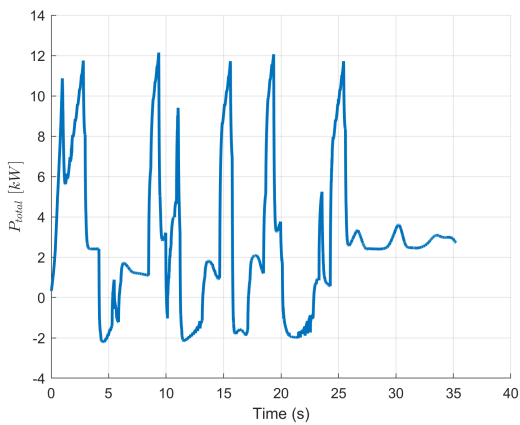
(b) Motor torque commands ( $T_{cmd}$ ) and effective values ( $T_{eff}$ ).



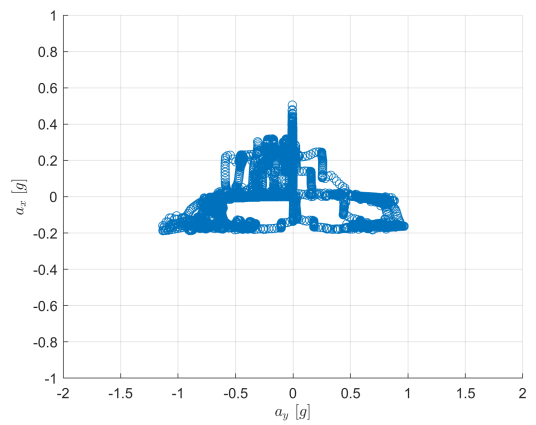
(c) Tire slip ratios ( $\kappa$ ).



(d) Yaw rate ( $r$ ).

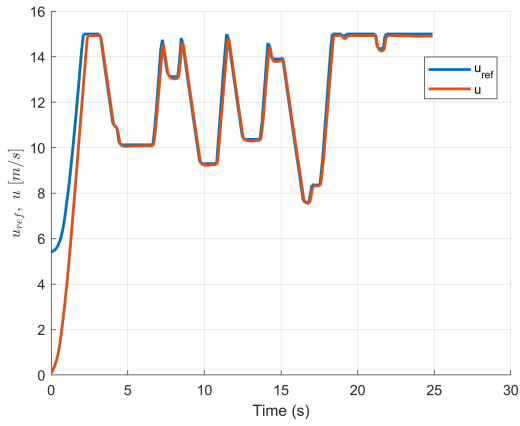


(e) Electric power ( $P_{total}$ ).

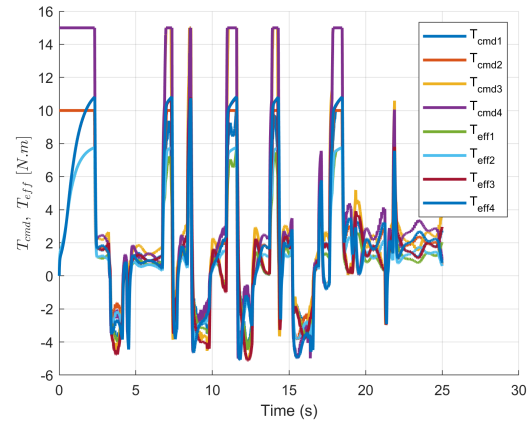


(f) G-G diagram.

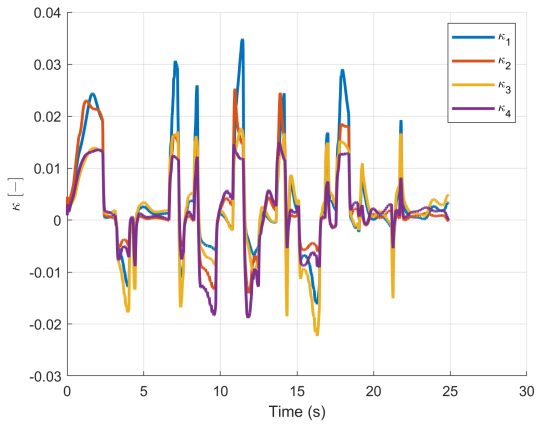
Figure 5.8: Results associated to the poor traction trajectory for the FSG race track.



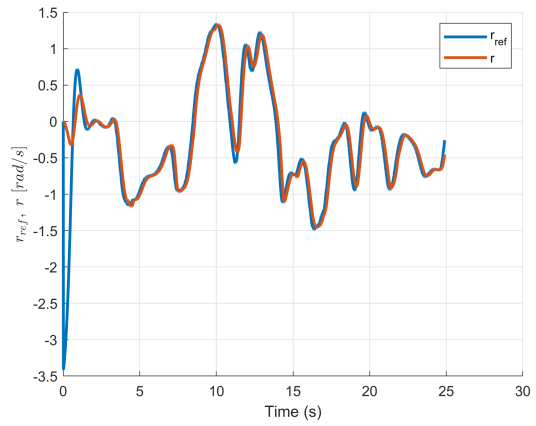
(a) Longitudinal speed ( $u$ ).



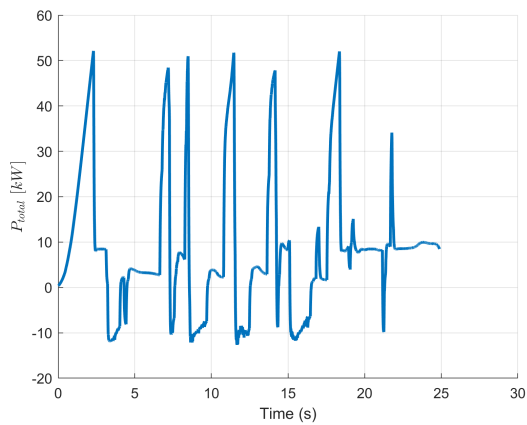
(b) Motor torque commands ( $T_{cmd}$ ) and effective values ( $T_{eff}$ ).



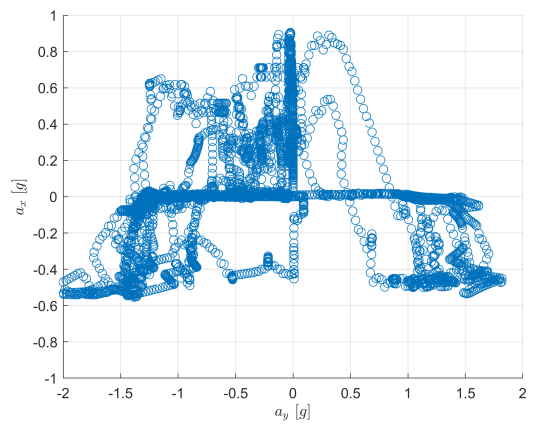
(c) Tire slip ratios ( $\kappa$ ).



(d) Yaw rate ( $r$ ).

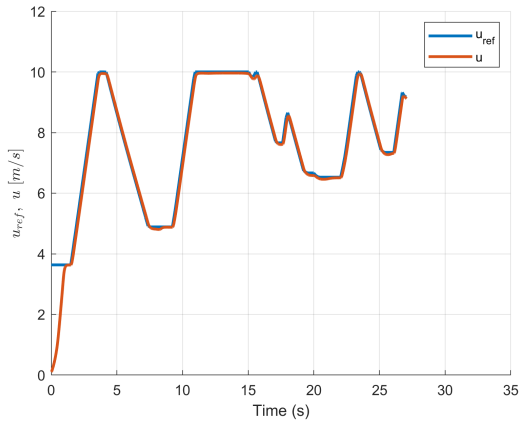


(e) Electric power ( $P_{total}$ ).

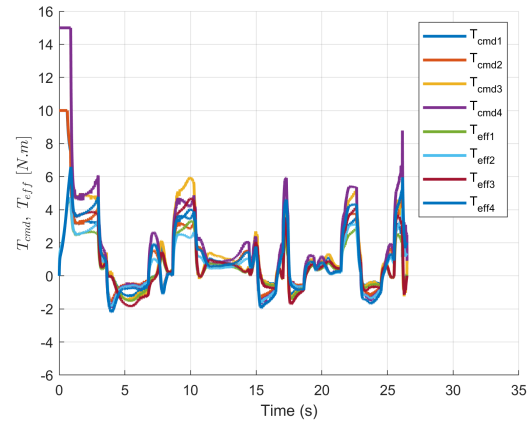


(f) G-G diagram.

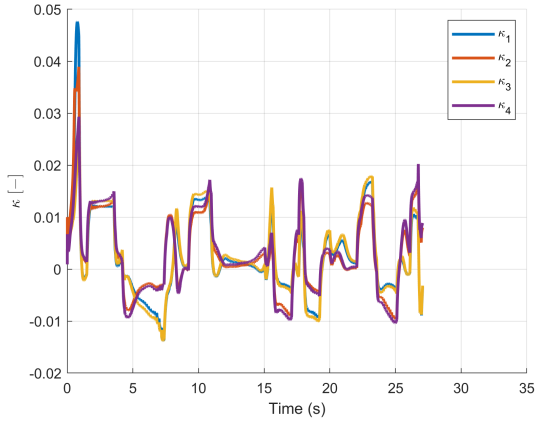
Figure 5.9: Results associated to the excellent traction trajectory for the FSG race track.



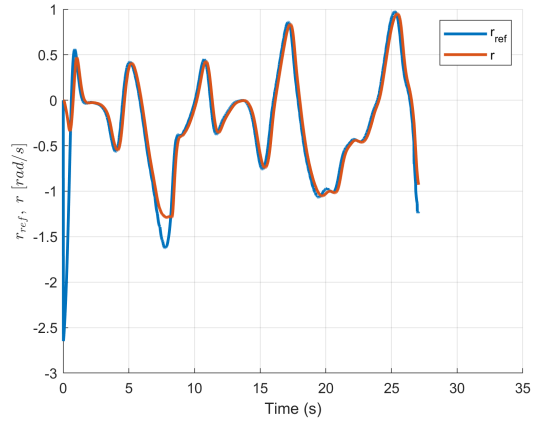
(a) Longitudinal speed ( $u$ ).



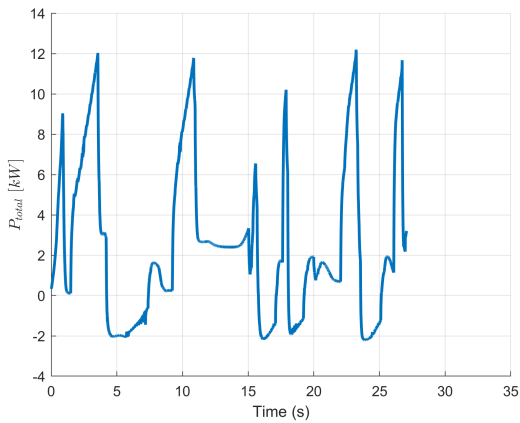
(b) Motor torque commands ( $T_{cmd}$ ) and effective values ( $T_{eff}$ ).



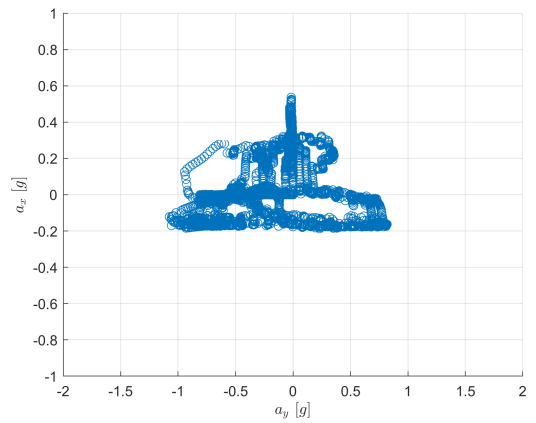
(c) Tire slip ratios ( $\kappa$ ).



(d) Yaw rate ( $r$ ).

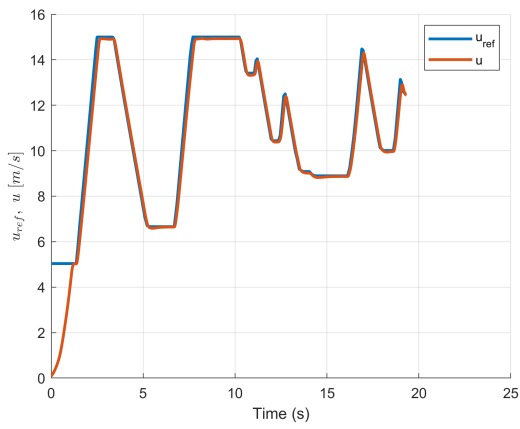


(e) Electric power ( $P_{total}$ ).

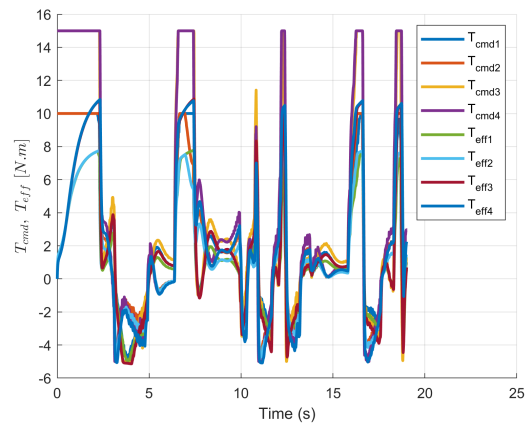


(f) G-G diagram.

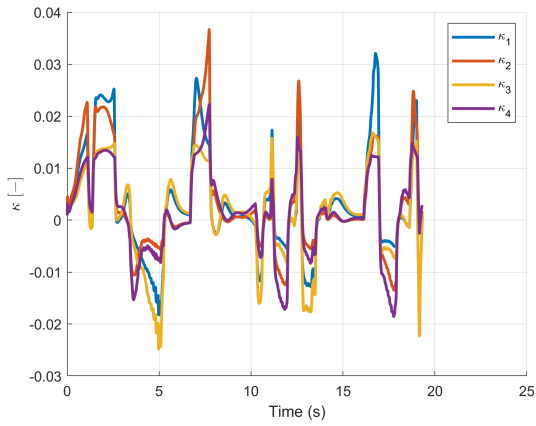
Figure 5.10: Results associated to the poor traction trajectory for the FSI race track.



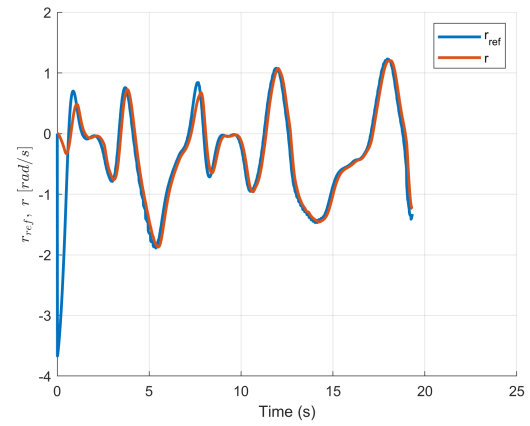
(a) Longitudinal speed ( $u$ ).



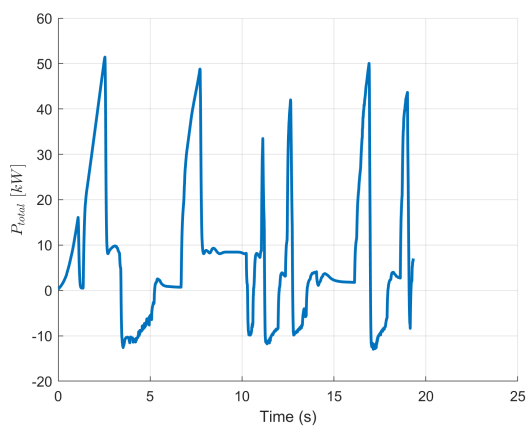
(b) Motor torque commands ( $T_{cmd}$ ) and effective values ( $T_{eff}$ ).



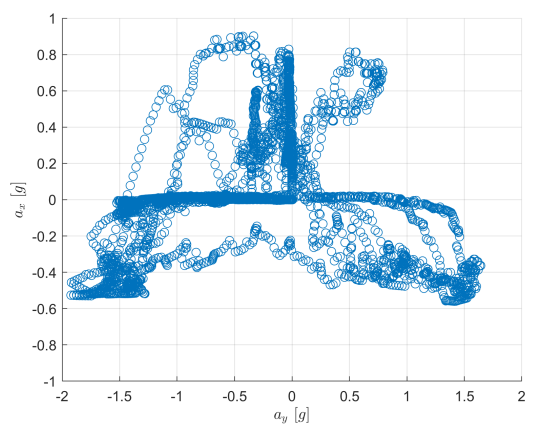
(c) Tire slip ratios ( $\kappa$ ).



(d) Yaw rate ( $r$ ).



(e) Electric power ( $P_{total}$ ).



(f) G-G diagram.

Figure 5.11: Results associated to the excellent traction trajectory for the FSI race track.

# Chapter 6

## Conclusions

### 6.1 Achievements

Analysing the results documented in the previous chapter, one concludes that the objectives for this thesis, defined in section 1.3, were accomplished. Initially, the main goal was understanding the physical mechanisms that govern traction of a ground vehicle, as well as the variables of interest that directly affect it. From the literature review made in section 1.2, it was made abundantly clear that a traction control system should be robust to nonlinearities and changes in operating conditions, a philosophy that was implemented throughout this work. Rather than adopting an approach that guarantees optimality in certain design conditions, a more heuristic-based approach was employed to suggest what proved to be a robust traction control solution in a wide range of racing scenarios.

Developing controllers in a simulation environment significantly decreases the duration and complexity of the design process. The sensitivity to parametric changes is easily studied, provided that sufficiently complex vehicle models are employed to adequately capture the desired dynamics. After experimenting with a number of unidimensional and single-track vehicle models, one concludes that a high-fidelity tridimensional vehicle model is necessary to capture the key variables that govern traction of a Formula Student vehicle: longitudinal and lateral tire slip, vertical load and dynamic mass transfers, tire-road friction coefficient and motor torque response - and, eventually, braking system dynamics, which were not considered in this thesis.

The developed control architecture is conceptually simple, however it is capable of simultaneously influencing both longitudinal and lateral vehicle dynamics, combining traction control in a holistic manner, from a planar point of view. The heuristic method suggested to separately tune the longitudinal and lateral controllers results in a robust solution to autonomously drive around a complex race track. It is clear that the driving performance in a generic race track is also influenced by the planning module and mid-level controllers, since the traction controllers are downstream from the planning and control pipeline. Understanding how the connected system works and how each module influences the vehicle is crucial.

A stark performance gain is achieved with the introduction of traction controllers on a Formula Student



prototype, as well as a less quantifiable - but still very important - safety benefit. The traction controllers essentially increase the average speed at which the vehicle is able to drive but also avoid unstable driving situations, making the vehicle's behaviour more predictable.

The traction controllers are developed with the autonomous prototype from FST Lisboa in mind, however they can be extended to the person-driven vehicle. To that end, instead of receiving longitudinal speed commands, the longitudinal controller would receive the accelerator and brake pedal positions to calculate the adequate motor torque - obviously with a re-tuning of the gains. The lateral controller and power distribution modules would remain identical.

## 6.2 Future work

Some aspects should be considered before implementing the proposed control solution in the Formula Student vehicle. Several variables should be fed back to the mid-level control and to the traction control modules. This thesis does not propose an estimator, which should be implemented to fuse the readings from redundant sensors and obtain the most likely estimate of each variable. One can argue, however, that the prediction model should be tridimensional and include suspension dynamics and a nonlinear tire model. The vehicle model can be either derived from first principles or determined via system identification from the simulator used in this thesis. If the vehicle runs as RWD, however, the longitudinal velocity and slip ratios estimation is vastly simplified if one has access to the angular speeds of the front wheels. For the 4WD configuration, a more complex estimator would be needed, such as an Extended Kalman Filter.

An accurate modelling of the electrical powertrain components would improve the simulation results and controller tuning process, including regenerative braking constraints rather than just a fixed boundary, inverters and battery efficiency maps, as well as a drivetrain characterization, which is expected to be far less efficient than the electrical components. With a more accurate powertrain modelling, the field-oriented motor controllers can be co-designed with the proposed traction controllers, allowing the study of the powertrain's thermal aspects and integration with the in-house motor/inverter solution being developed by FST Lisboa.

Several trajectory categories are employed to cover the expected range of traction conditions. However, with an online friction coefficient estimator, the trajectory can be automatically adapted to the existing track conditions, instead of changing it manually before or after a run. Additionally, the desired path can be redefined as function of traction conditions, since it is not likely that the optimal path is the same for very conservative and for excellent traction conditions. This idea implies communication not only from the mid-level to the traction controllers, but also vice-versa, since the trajectory definition benefits from information about the existing traction conditions.

# Bibliography

- [1] A. Aly, E.-S. Zeidan, A. Hamed, and F. A. Salem. An antilock-braking systems (abs) control: A technical review. *Intelligent Control and Automation*, 2011. doi: 10.4236/ica.2011.23023.
- [2] Fault-tolerant traction control of electric vehicles. *Control Engineering Practice*, 19(2):204–213, 2011. ISSN 0967-0661. doi: <https://doi.org/10.1016/j.conengprac.2010.11.012>.
- [3] Formula Student Técnico Lisboa; accessed on 02.02.2021, . URL <https://fstlisboa.com/en/home-en/>.
- [4] Formula Student Germany; accessed on 02.02.2021, . URL <https://www.formulastudent.de/fsg/>.
- [5] Formula Student Rules 2020 V1.0; Formula Student Germany 2020 Competition Handbook V1.0, . URL <https://www.formulastudent.de/fsg/rules/>.
- [6] Y. Hori, Y. Toyoda, and Y. Tsuruoka. Traction control of electric vehicle: basic experimental results using the test ev "uot electric march". *IEEE Transactions on Industry Applications*, 34(5):1131–1138, 1998. doi: 10.1109/28.720454.
- [7] W. Milliken and D. Milliken. *Race Car Vehicle Dynamics*. SAE International, 1995. ISBN 9781560915263.
- [8] H. Tan and Y. kwok Chin. Vehicle traction control: Variable-structure control approach. *Journal of Dynamic Systems Measurement and Control-transactions of The Asme*, 113:223–230, 1991.
- [9] T. Furuya, Y. Toyoda, and Y. Hori. Implementation of advanced adhesion control for electric vehicle. In *Proceedings of 4th IEEE International Workshop on Advanced Motion Control - AMC '96 - MIE*, volume 2, pages 430–435 vol.2, 1996. doi: 10.1109/AMC.1996.509287.
- [10] K. Fujii and H. Fujimoto. Traction control based on slip ratio estimation without detecting vehicle speed for electric vehicle. In *2007 Power Conversion Conference - Nagoya*, pages 688–693, 2007. doi: 10.1109/PCCON.2007.373040.
- [11] P. Khatun, C. M. Bingham, N. Schofield, and P. H. Mellor. Application of fuzzy control algorithms for electric vehicle antilock braking/traction control systems. *IEEE Transactions on Vehicular Technology*, 52(5):1356–1364, 2003. doi: 10.1109/TVT.2003.815922.

- [12] D. Yin, S. Oh, and Y. Hori. A novel traction control for ev based on maximum transmissible torque estimation. *IEEE Transactions on Industrial Electronics*, 56(6):2086–2094, 2009. doi: 10.1109/TIE.2009.2016507.
- [13] H. Pacejka. *Tire and Vehicle Dynamics*. 2012. doi: 10.1016/C2010-0-68548-8.
- [14] B. Subudhi and S. S. Ge. Sliding-mode-observer-based adaptive slip ratio control for electric and hybrid vehicles. *IEEE Transactions on Intelligent Transportation Systems*, 13(4):1617–1626, 2012. doi: 10.1109/TITS.2012.2196796.
- [15] S. Ko, J. Ko, S. Lee, J. Cheon, and H. Kim. A study on the road friction coefficient estimation and motor torque control for an in-wheel electric vehicle. *Proceedings of the Institution of Mechanical Engineers, Part D: Journal of Automobile Engineering*, 229(5):611–623, 2015. doi: 10.1177/0954407014547750.
- [16] F. Borrelli, A. Bemporad, M. Fodor, and D. Hrovat. An mpc/hybrid system approach to traction control. *IEEE Transactions on Control Systems Technology*, 14(3):541–552, 2006. doi: 10.1109/TCST.2005.860527.
- [17] D. Bohl, N. Kariotoglou, A. B. Hempel, P. J. Goulart, and J. Lygeros. Model-based current limiting for traction control of an electric four-wheel drive race car. pages 1981–1986, 2014. doi: 10.1109/ECC.2014.6862532.
- [18] A. Athayde. Path following and control for autonomous driving of a formula student car. Master's thesis, Instituto Superior Técnico, Universidade de Lisboa, 2021.
- [19] J. Ferro. Design and simulation of an abs control scheme for a formula student prototype. Master's thesis, Instituto Superior Técnico, Universidade de Lisboa, 2014.
- [20] H. Furtado. Model predictive control with a neural network model of a formula student prototype. Master's thesis, Instituto Superior Técnico, Universidade de Lisboa, 2020.
- [21] J. Antunes. Torque vectoring for a formula student prototype. Master's thesis, Instituto Superior Técnico, Universidade de Lisboa, 2017.
- [22] J. Loof, I. Besselink, and H. Nijmeijer. Traction control of an electric formula student racing car. In *Proceedings of the FISITA 2014 World Automotive Congress*, 2014.
- [23] R. Cordeiro. Modelagem e controle de trajetória de um veículo robótico terrestre de exterior. Master's thesis, Universidade Estadual de Campinas, 2013.
- [24] K. Ogata. *Modern Control Engineering*. 2010. ISBN 9780136156734.
- [25] C. C. de Wit, P. Tsotras, E. Velenis, M. Basset, and G. Gissinger. Dynamic friction models for road/tire longitudinal interaction. *Vehicle System Dynamics*, 39(3):189–226, 2003. doi: 10.1076/vesd.39.3.189.14152.

- [26] H. B. Pacejka and E. Bakker. The magic formula tyre model. *Vehicle System Dynamics*, 21(sup001): 1–18, 1992. doi: 10.1080/00423119208969994.
- [27] B. Beckman. The physics of racing. *Burbank, CA*, 91503, 1991.
- [28] *AMK Racing Kit*. AMK GmbH, 2015/26 edition, 2015.
- [29] B. Paden, M. Čáp, S. Z. Yong, D. Yershov, and E. Frazzoli. A survey of motion planning and control techniques for self-driving urban vehicles. *IEEE Transactions on Intelligent Vehicles*, 1(1):33–55, 2016. doi: 10.1109/TIV.2016.2578706.
- [30] R. N. Jazar. *Vehicle Dynamics*. Springer International Publishing, 2017. doi: 10.1007/978-3-319-53441-1.
- [31] A. Antunes. Sideslip estimation of formula student prototype. Master's thesis, Instituto Superior Técnico, Universidade de Lisboa, 2017.
- [32] S. Srinivasan, S. N. Giles, and A. Liniger. A holistic motion planning and control solution to challenge a professional racecar driver. *CoRR*, abs/2103.00358, 2021. URL <https://arxiv.org/abs/2103.00358>.